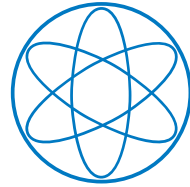


PHYSIK - DEPARTMENT



**Feasibility Study for a First
Observation of Coherent
Neutrino Nucleus Scattering
Using Low-Temperature
Detectors.**

DISSERTATION

VON

ACHIM GÜTLEIN



TECHNISCHE UNIVERSITÄT
MÜNCHEN

TECHNISCHE UNIVERSITÄT MÜNCHEN
Physik-Department
Lehrstuhl für Experimentalphysik und Astroteilchenphysik
Univ.-Prof. Dr. Stefan Schönert

Feasibility Study for a First Observation of Coherent Neutrino Nucleus Scattering Using Low-Temperature Detectors.

Achim Gütlein

Vollständiger Abdruck der von der Fakultät für Physik der Technischen Universität München zur Erlangung des akademischen Grades eines

Doktors der Naturwissenschaften (Dr. rer. nat.)

genehmigten Dissertation.

Vorsitzender: Univ.-Prof. Dr. B. Garbrecht

Prüfer der Dissertation:

1. Univ.-Prof. Dr. L. Oberauer
2. Univ.-Prof. S. Bishop, Ph.D. (schriftliche Beurteilung)

Priv.-Doz. Dr. A. Ulrich (mündliche Prüfung)

Die Dissertation wurde am 12.02.2013 bei der Technischen Universität München eingereicht und durch die Fakultät für Physik am 17.04.2013 angenommen.

Abstract

Coherent Neutrino Nucleus Scattering (CNNS) is a neutral current process of the weak interaction. For low transferred momenta the neutrino scatters coherently off all nucleons leading to an enhanced cross section. However, because of the small resulting recoil energies ($\mathcal{O}(\text{keV})$) CNNS has not been observed experimentally so far.

For the first observation of CNNS a strong neutrino source is needed. Thus, the expected count rates for solar neutrinos, supernova neutrinos, neutrinos generated by the decay of stopped π^+ particles at accelerators, and reactor neutrinos were calculated. Although an observation of CNNS could also be possible with other sources, the most promising neutrino sources are nuclear reactors with thermal powers between 2 and 4 GW. For an assumed energy threshold of 0.5 keV the target material with the largest count rate ($\sim 10 \text{ kg}^{-1} \text{ day}^{-1}$) is sapphire. Thus, a low-temperature detector based on a 32 g sapphire crystal was designed and built to measure the background spectrum for energies below $\sim 10 \text{ keV}$. Although the energy threshold ($\sim 1 \text{ keV}$) of this detector is too large for an observation of CNNS, the measured background spectrum can still be used for an investigation of the main background sources and the suppression of their events. For this investigation the simulated spectra of cosmic muons, ambient neutrons, and external gamma-rays are compared to the measured background spectrum. As a result, cosmic muons are the main contribution to the measured background spectrum.

For a future experiment aiming at the observation of CNNS an array of 125 low-temperature detectors based on 32 g sapphire crystals is assumed. Background simulations of cosmic muons, ambient neutrons, and intrinsic radioactivity show that especially an efficient muon-veto system is crucial for a sufficient background suppression. To study the observation potential of this future experiment a distance of $\sim 40 \text{ m}$ to a reactor core with a thermal power of $\sim 4 \text{ GW}$ (neutrino flux of $\sim 3.6 \cdot 10^{12} \text{ cm}^{-2} \text{ s}^{-1}$) and a rejection of $\sim 99.9\%$ of the background events are assumed. The probability to reject a background-only hypothesis at a confidence level of 99.99% is $\sim 50\%$ for an exposure of 4 kg-years. For larger exposures and a location closer to the reactor also physics beyond the standard model could be investigated. The reachable upper limit on the magnetic moment of the neutrino is worse than the current best limit by a factor of ~ 3 . For an oscillation of flavor neutrinos ($\nu_e, \nu_\mu, \nu_\tau, \bar{\nu}_e, \bar{\nu}_\mu, \text{ and } \bar{\nu}_\tau$) into sterile neutrinos a $3\text{-}\sigma$ -effect could be observed with a probability of $\sim 1\%$.

Furthermore, due to CNNS atmospheric and also solar neutrinos can constitute an ultimate background source for direct dark matter searches limiting the achievable sensitivity for the WIMP-nucleon cross section to a material-dependent value between 3 and $9 \cdot 10^{-48} \text{cm}^2$. These achievable limits were calculated for neon, argon, germanium, xenon, and calcium tungstate.

Zusammenfassung

Die kohärente Neutrinostreuung an Atomkernen (Coherent Neutrino Nucleus Scattering, CNNS) ist ein neutraler Stromprozess der schwachen Wechselwirkung. Bei niedrigen Impulsüberträgen wird das Neutrino kohärent an allen Nukleonen gestreut, was zu einem erhöhten Wirkungsquerschnitt führt. Wegen der niedrigen Rückstoßenergien ($\mathcal{O}(\text{keV})$) wurde die CNNS allerdings bisher noch nicht experimentell beobachtet.

Um eine starke Neutrinoquelle für den Nachweis der CNNS zu finden, wurden die erwarteten Zählraten für solare Neutrinos, Supernovaneutrinos, Neutrinos aus dem Zerfall gestoppter Pionen und Reaktor-neutrinos berechnet. Obwohl ein Nachweis mit allen Quellen möglich wäre, sind Kernreaktoren mit einer thermischen Leistung von 2 bis 4 GW am vielversprechendsten. Für eine angenommene Energieschwelle von 0,5 keV ist Saphir das Detektormaterial mit der höchsten Zählrate ($\sim 10 \text{ kg}^{-1} \text{ day}^{-1}$). Deshalb wurde für die Messung des Untergrundspektrums für Energien unterhalb von $\sim 10 \text{ keV}$ ein Tieftemperaturdetektor hergestellt, der auf einem 32 g schweren Saphirkristall basiert. Obwohl die Energieschwelle dieses Detektors mit $\sim 1 \text{ keV}$ zu hoch für den Nachweis der CNNS ist, kann das gemessene Spektrum trotzdem dazu verwendet werden, den Hauptanteil des Untergrunds und seine Unterdrückung zu untersuchen. Dazu wurden die simulierten Spektren für kosmische Myonen, Neutronen aus der Detektorumgebung und externe Gammastrahlung mit dem gemessenen Spektrum verglichen. Durch diesen Vergleich lassen sich kosmische Myonen als Hauptquelle für den Untergrund feststellen.

Für ein zukünftiges Experiment zum Nachweis der CNNS wurde ein Aufbau mit 125 Tieftemperaturdetektoren angenommen, die auf 32 g schweren Saphirkristallen basieren. Die Untergrundsimulationen mit kosmischen Myonen, Neutronen aus der Detektorumgebung und intrinsischer Radioaktivität zeigen, dass ein effizientes Myonvetosystem entscheidend für eine ausreichende Untergrundunterdrückung ist. Um das Nachweispotential dieses zukünftigen Experiments zu untersuchen, wurde ein Abstand von $\sim 40 \text{ m}$ zu einem Reaktorkern mit einer thermischen Leistung von $\sim 4 \text{ GW}$ (Neutrinofluß: $\sim 3,6 \cdot 10^{12} \text{ cm}^{-2} \text{ s}^{-1}$) und eine Unterdrückung von $\sim 99,9\%$ des Untergrunds angenommen. Die Wahrscheinlichkeit, eine Hypothese, die nur Untergrund annimmt, auf einem Konfidenzniveau von 99,99% auszuschließen, ist $\sim 50\%$ für eine Messzeit von 4 kg-Jahren. Für längere Messzeiten und eine Detektorposition näher am Reaktorkern könnte die Entdeckung von Physik jenseits des Standardmodels möglich sein. Während die erreichbare

obere Grenze für ein magnetisches Moment des Neutrinos um einen Faktor von ~ 3 schlechter ist als die aktuelle experimentelle Obergrenze, könnte mit einer Wahrscheinlichkeit von $\sim 1\%$ ein $3\text{-}\sigma$ Effekt für eine Oszillation von Flavorneutrinos ($\nu_e, \nu_\mu, \nu_\tau, \bar{\nu}_e, \bar{\nu}_\mu$ und $\bar{\nu}_\tau$) in sterile Neutrinos beobachtet werden.

Darüberhinaus kann die kohärente Neutrinostreuung atmosphärischer und solarer Neutrinos eine Untergrundquelle für Experimente zur direkten Suche nach dunkler Materie werden. Die erreichbare Sensitivität dieser Experimente hinsichtlich des WIMP-Nukleon-Wirkungsquerschnitts wird auf einen materialabhängigen Wert zwischen 3 und $9 \cdot 10^{-48} \text{ cm}^2$ begrenzt. Die erreichbaren Sensitivitäten wurden für Neon, Argon, Germanium, Xenon und Calciumwolframat berechnet.

Contents

1	Coherent Neutrino Nucleus Scattering (CNNS)	1
1.1	Cross section	2
1.2	Count-rate calculation	3
1.2.1	Solar neutrinos	4
1.2.2	Reactor neutrinos	7
1.2.3	Stopped pion source	13
1.2.4	Supernova neutrinos	17
2	Low-temperature detectors for the observation of CNNS	21
2.1	Thermal model for low-temperature detectors	22
2.2	Transition Edge Sensor (TES)	28
2.3	Read-out system	29
2.4	Calibration methods	31
2.4.1	LED calibration	31
2.4.2	Direct TES calibration	33
2.5	Setup of a future experiment for the observation of CNNS	33
3	Measurements with a low-temperature detector	37
3.1	Calibration measurement	38
3.2	Background spectrum for low energies	43
4	Data analysis: template fit and applied cuts	47
4.1	Determination of pulse parameters	47
4.2	Template fit	50
4.2.1	Generation of a template	51
4.2.2	Goodness of fit and χ^2 Minimization	52
4.3	Rejection of poor events	57
4.3.1	Cut on the base-line width σ_{BL}	58
4.3.2	Cut on the base-line slope m_{BL}	59
4.3.3	Cut on the goodness of the template fit	60
4.3.4	Cut on peak position and onset channel	61

4.4	Determination of the cut efficiency	63
5	Background investigations for a future CNNS experiment	69
5.1	Simulation of the background measurement	69
5.1.1	Muon background	70
5.1.2	Neutron background	73
5.1.3	Gamma background	74
5.2	Simulation of a future experiment	77
5.2.1	The use of coincident events to reject background . . .	79
5.2.2	Cosmic muon background	81
5.2.3	Ambient neutron background	83
5.2.4	External and internal gamma background	85
6	Observation potential for a future CNNS experiment	91
6.1	Hypothesis testing and Bayes' theorem	91
6.2	Parameter estimation and observation potential	93
7	Investigation of physics beyond the standard model	101
7.1	Magnetic moment of the neutrino	101
7.2	Search for sterile neutrinos	106
8	Neutrinos as background for direct dark-matter searches	109
8.1	Direct dark-matter searches	109
8.2	Neutrinos as background source	110
8.2.1	Solar neutrinos	111
8.2.2	Atmospheric neutrinos	117
8.3	Limitations for future experiments	120
9	Conclusions and outlook	127
	References	133

Chapter 1

Coherent Neutrino Nucleus Scattering (CNNS)

The Coherent Neutrino Nucleus Scattering (CNNS) is a neutral-current process of the weak interaction and thus independent of the neutrino flavor. A neutrino ν_x of any flavor ($\nu_x \in \{\nu_e, \nu_\mu, \nu_\tau, \bar{\nu}_e, \bar{\nu}_\mu, \bar{\nu}_\tau\}$) scatters off a nucleus via the exchange of a virtual Z^0 boson. For low transferred momenta the wavelength of the Z^0 boson is of the order of the diameter of the nucleus. Thus, the neutrino scatters coherently off all nucleons. Figure 1.1 depicts the Feynman diagram for this process.

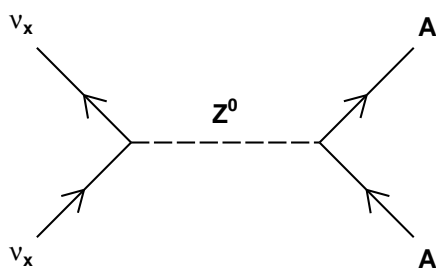


Figure 1.1: Feynman diagram for the Coherent Neutrino Nucleus Scattering (CNNS). A neutrino ν_x of any flavor scatters off a nucleus with mass number A via the exchange of a virtual Z^0 boson. For low transferred momenta the neutrino scatters coherently off all nucleons leading to a N^2 dependence of the total scattering cross section (see also equation (1.6)).

1.1 Cross section

Due to the coherence of the scattering the cross section for CNNS is enhanced compared to other neutrino interactions. The cross section in the laboratory frame is given by [1, 2]

$$\frac{d\sigma}{d\cos\theta} = \frac{G_F^2}{8\pi} [Z(4\sin^2\theta_W - 1) + N]^2 E_\nu^2 (1 + \cos\theta) |f(q)|^2 \quad (1.1)$$

$$\frac{d\sigma}{dE_{rec}} = \frac{G_F^2}{8\pi} [Z(4\sin^2\theta_W - 1) + N]^2 M \left(2 - \frac{E_{rec}M}{E_\nu^2}\right) |f(q)|^2 \quad (1.2)$$

$$\sigma_{tot} = \int_0^{\frac{2E_\nu^2}{M}} dE_{rec} \frac{d\sigma}{dE_{rec}}, \quad (1.3)$$

where G_F is the Fermi constant, Z the proton number of the target nucleus, N the neutron number of the target nucleus, θ_W the Weinberg angle, E_ν the neutrino energy, θ the scattering angle in the laboratory frame, $f(q)$ is the form factor as described below, M the mass of the target nucleus, and $E_{rec} = \frac{E_\nu^2}{M}(1 - \cos\theta)$ its recoil energy. For a given neutrino energy E_ν the maximal recoil energy is $\frac{2E_\nu^2}{M}$.

For large transferred momenta $q = \sqrt{2ME_{rec}}$ the Z^0 wavelength is smaller than the target nucleus. Thus, the cross section is modified by a form factor $|f(q)|^2$. The form factor is the Fourier-transformation of the weak charge distribution of the target nucleus[3]. In this work the weak charge distribution is assumed to be identical to the electric charge distribution[4]. Helm[5] assumed that the charge distribution is the convolution of a step function describing the inner part of the nucleus and a Gaussian describing the shell of the nucleus. The advantage of this assumption for the charge distribution is that its Fourier-transformation can be calculated analytically. Thus, the form factor used in this work is[5]

$$|f(q)|^2 = \left(3 \frac{j_1(qR_0)}{qR_0}\right)^2 e^{-q^2s^2} = \left(3 \frac{\sin(qR_0) - qR_0 \cos(qR_0)}{q^3 R_0^3}\right)^2 e^{-q^2s^2}, \quad (1.4)$$

where j_1 is the spherical Bessel function of the first kind and order 1, $R_0 = 1.14A^{\frac{1}{3}} \text{ fm}$ [4] the effective radius of the target nucleus, and $s = 0.9 \text{ fm}$ [4] the skin thickness of the nucleus. With these values for s and R_0 the Helm form factor (1.4) is in agreement with other approaches to the form factor[4]. In figure 1.2 the Helm form factor is shown for different materials as a function of the recoil energy.

Taking the Helm form factor into account the function for the cross section (see equation (1.2)) can only be integrated numerically. However, since low-energetic neutrinos, e.g. reactor neutrinos (see section 1.2.2) are generating

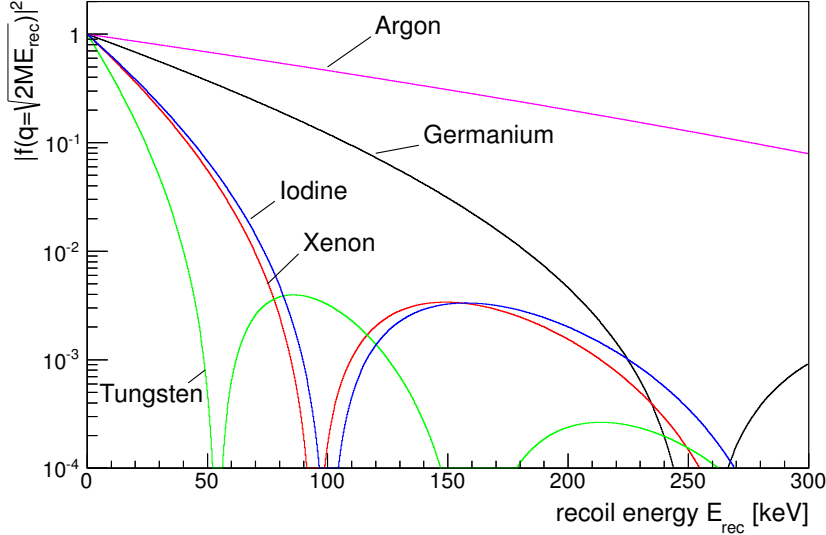


Figure 1.2: Helm form factor for different materials. The charge density is assumed to be the convolution of a step function describing the inner part and a Gaussian describing the shell of the nucleus.

low transferred momenta, the form factor can be neglected. Hence, for low-energetic neutrinos the total cross section can be calculated:

$$\sigma_{tot} \stackrel{f(q)=1}{=} \frac{G_F^2}{4\pi} [Z (4 \sin^2 \theta_W - 1) + N]^2 E_\nu^2. \quad (1.5)$$

Since $\sin^2 \theta_W = 0.23$ [6], the total cross section σ_{tot} is approximately given by

$$\sigma_{tot} \approx \frac{G_F^2}{4\pi} N^2 E_\nu^2 = 4.2 \cdot 10^{-45} N^2 \left(\frac{E_\nu}{1 \text{ MeV}} \right)^2 \text{ cm}^2. \quad (1.6)$$

1.2 Count-rate calculation

The CNNS count rate R is given by

$$R = N_t \int_0^\infty dE_\nu \Phi(E_\nu) \sigma_{tot}(E_\nu), \quad (1.7)$$

where N_t is the number of target nuclei, E_ν the neutrino energy, $\Phi(E_\nu)$ is the flux of neutrinos with energy E_ν , and $\sigma_{tot}(E_\nu)$ is the CNNS cross section for neutrino energy E_ν . Using equation (1.5) for $\sigma_{tot}(E_\nu)$, the count rate is given by

$$R = N_t \int_0^\infty dE_\nu \Phi(E_\nu) \int_0^{\frac{2E_\nu^2}{M}} dE_{rec} \frac{d\sigma(E_\nu, E_{rec})}{dE_{rec}}. \quad (1.8)$$

In order to calculate the recoil spectrum the two integrals in (1.8) have to be swapped. The integration limits have to be changed, too. The lower limit of the second integration in (1.9) is determined by the minimum neutrino energy leading to a given recoil energy. The rate R is then determined by:

$$R = N_t \int_0^\infty dE_{rec} \int_{\sqrt{\frac{E_{rec}M}{2}}}^\infty dE_\nu \Phi(E_\nu) \frac{d\sigma(E_\nu, E_{rec})}{dE_{rec}}. \quad (1.9)$$

The recoil spectrum $\frac{dR}{dE_{rec}}$ is now given by the integrand of equation (1.9):

$$\frac{dR}{dE_{rec}} = N_t \int_{\sqrt{\frac{E_{rec}M}{2}}}^\infty dE_\nu \Phi(E_\nu) \frac{d\sigma(E_\nu, E_{rec})}{dE_{rec}}. \quad (1.10)$$

This integral can in general not be solved analytically. Therefore, a numerical algorithm is used to calculate the recoil spectra for different neutrino sources. For this work the Romberg integration algorithm (see section 4.3 in [7]) was used.

The count rate R_{th} above an energy threshold E_{th} is given by:

$$R_{th} = N_t \int_{E_{th}}^\infty dE_{rec} \int_{\sqrt{\frac{E_{rec}M}{2}}}^\infty dE_\nu \Phi(E_\nu) \frac{d\sigma(E_\nu, E_{rec})}{dE_{rec}}. \quad (1.11)$$

1.2.1 Solar neutrinos

The last missing term in equations (1.10) and (1.11) is the neutrino flux $\Phi(E_\nu)$. A strong neutrino source is needed for the observation of CNNS with detector masses of $\mathcal{O}(\text{kg})$. The strongest natural neutrino source is the sun. The integrated solar neutrino flux is $\sim 6.5 \cdot 10^{10} \text{ cm}^{-2}\text{s}^{-1}$ (model BP04(Garching))[8]. The production mechanisms of the different solar neutrinos are listed in table 1.1. The fluxes given in the third column are taken from [8] (model BP04 (Garching)).

The energy spectra of the different solar neutrinos[9] are shown in figure 1.3. The neutrinos produced in the CNO cycle (^{13}N , ^{15}O , ^{17}F) are represented by the dotted lines. The solid lines depict the neutrinos produced in the proton-proton chain (pp, pep, hep, ^7Be , ^8B).

The values for the continuous energy spectra (pp, hep, ^8B , ^{13}N , ^{15}O , ^{17}F) given in [9] were fitted by a polynomial of ninth order:

$$\Phi(E_\nu) = \begin{cases} \frac{1}{N} \sum_{i=0}^8 a_i E_\nu^{i+1} & \text{for } E_\nu < E_{\nu,max} \\ 0 & \text{for } E_\nu \geq E_{\nu,max} \end{cases} \quad (1.12)$$

$$N = \sum_{i=0}^8 \frac{1}{i+2} a_i E_{\nu,max}^{i+2}, \quad (1.13)$$

Solar neutrinos	Production mechanism	flux [$\text{cm}^{-2}\text{s}^{-1}$]
pp	$p + p \rightarrow {}^2\text{H} + e^+ + \nu_e$	$5.54 \cdot 10^{10}$
pep	$p + e^- + p \rightarrow {}^2\text{H} + \nu_e$	$1.41 \cdot 10^8$
hep	${}^3\text{He} + p \rightarrow {}^4\text{He} + e^+ + \nu_e$	$7.88 \cdot 10^3$
${}^7\text{Be}$	${}^7\text{Be} + e^- \rightarrow {}^7\text{Li} + \nu_e$	$4.84 \cdot 10^9$
${}^8\text{B}$	${}^8\text{B} \rightarrow {}^8\text{Be}^* + e^+ + \nu_e$	$5.74 \cdot 10^6$
${}^{13}\text{N}$	${}^{13}\text{N} \rightarrow {}^{13}\text{C} + e^+ + \nu_e$	$5.70 \cdot 10^8$
${}^{15}\text{O}$	${}^{15}\text{O} \rightarrow {}^{15}\text{N} + e^+ + \nu_e$	$4.98 \cdot 10^8$
${}^{17}\text{F}$	${}^{17}\text{F} \rightarrow {}^{17}\text{O} + e^+ + \nu_e$	$5.87 \cdot 10^6$

Table 1.1: Production mechanisms and fluxes of the different solar neutrinos (model BP04(Garching))[8]. In the so-called proton-proton chain pp, pep, hep, ${}^7\text{Be}$ and ${}^8\text{B}$ neutrinos are produced. In the CNO-cycle, ${}^{13}\text{N}$, ${}^{15}\text{O}$ and ${}^{17}\text{F}$ neutrinos are generated.

where N is a normalisation constant and $E_{\nu,max}$ the maximum neutrino energy. The values for $E_{\nu,max}$ used for the calculation of the recoil spectra are

Solar neutrinos	$E_{\nu,max}$ [MeV]
pp	0.428
hep	18.79
${}^8\text{B}$	14.88
${}^{13}\text{N}$	1.201
${}^{15}\text{O}$	1.733
${}^{17}\text{F}$	1.74

Table 1.2: Maximum neutrino energy $E_{\nu,max}$ for the continuous solar neutrino spectra[9].

given in table 1.2. The values for the fit parameters a_i are given in table 1.3.

With the energy spectra of equation (1.12), the fluxes given in table 1.1, and equation (1.10) the recoil spectra for the different solar neutrinos can be calculated. As an example, figure 1.4 shows the recoil spectra for the different neutrinos with sapphire (Al_2O_3) as target material in the left diagram. In the right diagram the integrated count rate R_{th} versus recoil-energy threshold for the different neutrinos is shown.

For an energy threshold of 0.1 keV the total count rate for solar neutrinos is ~ 174 per ton-year corresponding to ~ 0.48 counts per ton-day. Thus, a ton-scale detector would be needed for the observation of CNNS. For recoil energies $\gtrsim 0.4$ keV the spectrum is dominated by ${}^8\text{B}$ and hep neutrinos, for lower recoil energies also pep neutrinos and the neutrinos from the CNO-cycle

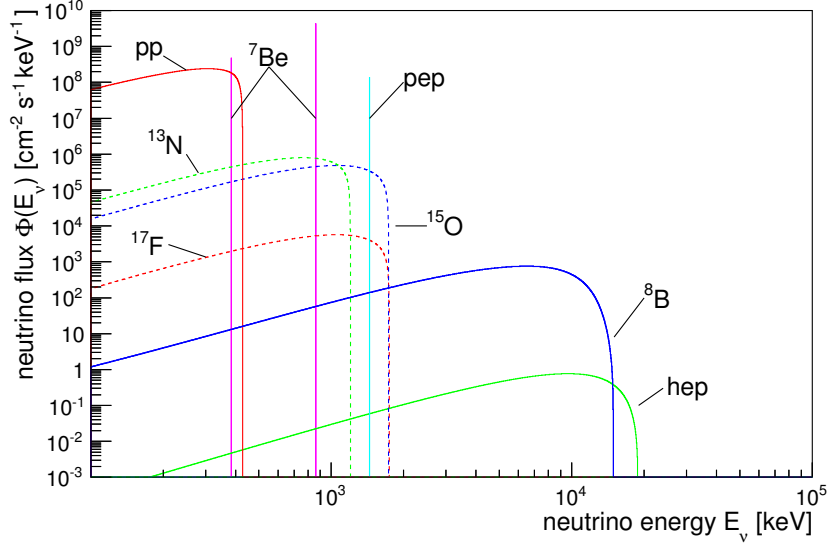


Figure 1.3: Energy spectra of solar neutrinos. The dotted spectra are produced in the CNO-cycle, the others are produced in the proton-proton chain. The overall flux of solar neutrinos is $\sim 6.5 \cdot 10^{10} \text{ cm}^{-2} \text{ s}^{-1}$ and by far dominated by the low-energetic pp-neutrinos.

are visible.

Due to the production processes the neutrinos from the CNO-cycle are strongly coupled to the metallicity of the sun[10, 11]. Currently solar models with low metallicity and high metallicity are discussed leading to a difference of 30% to 40% in the CNO flux[10, 11]. Thus, a precise measurement of the CNO flux could distinguish between solar models with low and high metallicity.

Unfortunately, the recoil spectra of CNO and pep neutrinos are strongly overlapping (see figure 1.4). So only the combined flux of pep and CNO neutrinos can be measured using sapphire detectors. However, the pep neutrino flux has a very small uncertainty of $\sim 1\%$ due to constraints by the solar luminosity[11]. Thus, a combined measurement of CNO and pep neutrinos could help to distinguish between low and high metallicity.

For the observation of CNO and pep neutrinos very large detector masses (10 to 100 tons) would be needed. Since it is very difficult to produce detectors with energy thresholds of $\sim 0.1 \text{ keV}$ and ton-scale or even higher masses for precise measurements, the fluxes of solar neutrinos are probably too small for an observation of CNNS and the measurement of the CNO flux.

It has to be emphasized that solar and also atmospheric neutrinos can be a dangerous background source for direct dark matter searches[2, 12, 13, 14,

	pp	hep	⁸B
a_0	$-2.87034 \cdot 10^{-1}$	$-2.04975 \cdot 10^{-6}$	$6.01473 \cdot 10^{-4}$
a_1	$1.63559 \cdot 10^2$	$4.22577 \cdot 10^{-3}$	$1.49699 \cdot 10^{-2}$
a_2	$-1.22253 \cdot 10^3$	$-4.70817 \cdot 10^{-4}$	$-2.6481 \cdot 10^{-3}$
a_3	$1.55085 \cdot 10^4$	$2.55332 \cdot 10^{-5}$	$-2.4141 \cdot 10^{-5}$
a_4	$-1.465140 \cdot 10^5$	$-2.81714 \cdot 10^{-6}$	$6.22325 \cdot 10^{-5}$
a_5	$7.843750 \cdot 10^5$	$3.06961 \cdot 10^{-7}$	$-9.84329 \cdot 10^{-6}$
a_6	$-2.35724 \cdot 10^6$	$-1.87479 \cdot 10^{-8}$	$7.51311 \cdot 10^{-7}$
a_7	$3.71082 \cdot 10^6$	$6.01396 \cdot 10^{-10}$	$-2.8606 \cdot 10^{-8}$
a_8	$-2.38308 \cdot 10^6$	$-7.88874 \cdot 10^{-12}$	$4.31573 \cdot 10^{-10}$
	¹³N	¹⁵O	¹⁷F
a_0	$-2.59522 \cdot 10^{-2}$	$-1.36811 \cdot 10^{-2}$	$-6.74473 \cdot 10^{-2}$
a_1	$1.05228 \cdot 10^1$	3.94221	4.63141
a_2	$-3.2344 \cdot 10^1$	-8.55431	$-1.1535 \cdot 10^1$
a_3	$1.33211 \cdot 10^2$	$2.36712 \cdot 10^1$	$2.85067 \cdot 10^1$
a_4	$-4.11848 \cdot 10^2$	$-5.00477 \cdot 10^1$	$-5.11664 \cdot 10^1$
a_5	$7.28405 \cdot 10^2$	$6.07542 \cdot 10^1$	$5.51102 \cdot 10^1$
a_6	$-7.26105 \cdot 10^2$	$-4.15278 \cdot 10^1$	$-3.45332 \cdot 10^1$
a_7	$3.8137 \cdot 10^2$	$1.49462 \cdot 10^1$	$1.1655 \cdot 10^1$
a_8	$-8.21149 \cdot 10^1$	-2.20367	-1.63814

Table 1.3: Fit parameters a_i used in equation (1.12) for all neutrino species with continuous energy spectra. The total uncertainty of the energy spectra is $\sim 1\%$.

15, 16] (see chapter 8).

1.2.2 Reactor neutrinos

Nuclear power plants are producing very high fluxes of neutrinos. The mean energy release per fission is $\sim 205.3 \text{ MeV}$ [17]. For a thermal power of 2 GW that leads to $\sim 6.08 \cdot 10^{19}$ fissions per second. On average there are 6 anti-electron neutrinos emitted in subsequent β -decays[17] for each fission. Thus, a 2 GW reactor produces $N_\nu \approx 3.65 \cdot 10^{20}$ anti-electron neutrinos per second. These neutrinos are emitted in each direction. The neutrino flux Φ_0 at the distance R of the reactor core is given by

$$\Phi_0 = \frac{N_\nu}{4\pi R^2} \left[\frac{1}{\text{cm}^2\text{s}} \right]. \quad (1.14)$$

The neutrino flux at a distance of $R = 17 \text{ m}$ is $\sim 1.0 \cdot 10^{13} \text{ cm}^{-2}\text{s}^{-1}$.

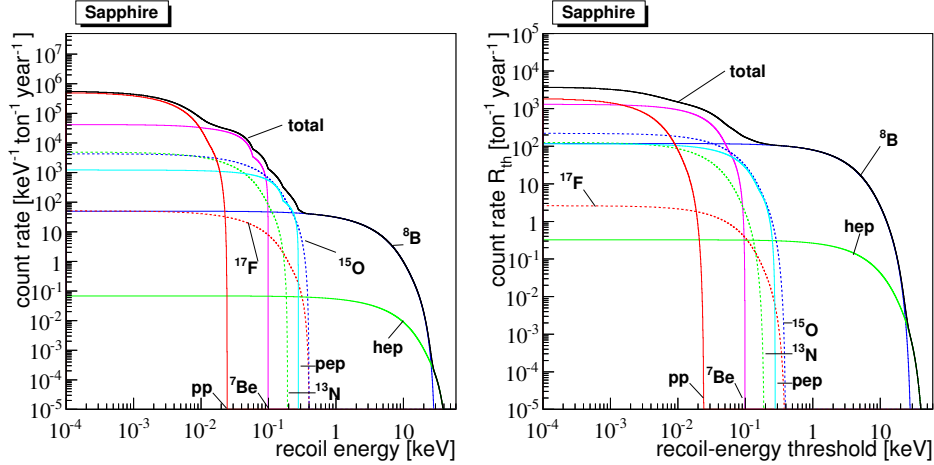


Figure 1.4: *Left diagram:* Recoil spectra of the different solar neutrinos with sapphire (Al_2O_3) as target material.

Right diagram: Integrated count rate R_{th} above a recoil-energy threshold. For a threshold of ~ 0.1 keV in addition to ${}^8\text{B}$, pep and hep neutrinos also neutrinos from the CNO-cycle would be visible. A measurement of the flux of CNO neutrinos could distinguish between solar models with high metallicity and models with low metallicity since the flux of CNO neutrinos is highly dependent on the metallicity[10, 11].

The energy dependence of the neutrino fluxes given in [18]¹ was for each fuel component² fitted by the following function:

$$\Phi_i(E_\nu) = \frac{1}{N_i} \cdot \left[A_0 \left(e^{-\frac{E_\nu}{a_0}} - e^{-\frac{E_\nu}{a_1}} \right) + A_1 \left(e^{-\frac{E_\nu}{a_2}} - e^{-\frac{E_\nu}{a_0}} \right) \right] \quad (1.15)$$

$$N_i = \frac{1}{a_0(A_0 - A_1) - a_1A_0 + a_2A_1}, \quad (1.16)$$

where $\Phi_i(E_\nu)$ is the normalized energy spectrum of the fuel component i and N_i is its normalisation constant. The fit parameters A_0 , A_1 and a_0 , a_1 and a_2 are given in table 1.4. The flux for reactor neutrinos is given by

$$\Phi(E_\nu) = \frac{N_\nu}{4\pi R^2} \sum_{\text{fuel components}} n_i \cdot \Phi_i(E_\nu). \quad (1.17)$$

The parameters n_i are describing the fuel composition and are thus characteristic for each reactor. For most pressurised water reactors a standard fuel composition consisting of 62% ${}^{235}\text{U}$, 30% ${}^{239}\text{Pu}$, and 8% ${}^{238}\text{U}$ [18] can be used. Figure 1.5 shows the standard reactor anti-neutrino spectrum for this kind

¹The fluxes given in the last column of table 3 in [18] were used.

²Only the most frequent isotopes, i.e., ${}^{235}\text{U}$, ${}^{238}\text{U}$, and ${}^{239}\text{Pu}$ are taken into account.

	^{235}U	^{238}U	^{239}Pu
A_0	$1.72254 \cdot 10^0$	$1.04669 \cdot 10^1$	$1.52535 \cdot 10^0$
A_1	$1.05200 \cdot 10^1$	$2.51948 \cdot 10^1$	$1.03982 \cdot 10^1$
a_0	$8.96017 \cdot 10^2$	$8.54174 \cdot 10^2$	$7.99199 \cdot 10^2$
a_1	$1.05450 \cdot 10^3$	$8.56805 \cdot 10^2$	$9.38927 \cdot 10^2$
a_2	$9.45390 \cdot 10^2$	$8.64198 \cdot 10^2$	$8.42464 \cdot 10^2$

Table 1.4: Fit parameters A_0 , A_1 , a_0 , a_1 , a_2 used in equation (1.15) for the different fuels used in this work.

of reactors. It is important to note that in pressurised water reactors one third of the fuel is exchanged once every year. Thus, the fuel composition changes only little with time[18].

The recoil-energy spectrum can be calculated according to equation (1.10). The recoil-energy spectra for different target materials are shown in the left panel of figure 1.6. For heavy target materials the recoil-energy spectra are shifted to low recoil energies ($E_{rec} \propto \frac{1}{M}$). However, the cross section is enhanced ($\sigma_{tot} \propto N^2$, see equation (1.5)) for heavy target materials. Thus, depending on the energy threshold different target materials are leading to the best count rate (see figure 1.6, right panel). For energy thresholds above ~ 400 eV sapphire (Al_2O_3) provides the highest count rate whereas calcium tungstate (CaWO_4) is the best target material for energy thresholds below ~ 100 eV. For energy thresholds between 100 eV and 400 eV germanium has the highest count rate.

Depending on energy threshold and target material the count rate for an experiment in ~ 17 m distance to a power reactor is between ~ 5 (Al_2O_3 , $E_{th} \sim 1$ keV) and ~ 120 counts per kg and per day (CaWO_4 , $E_{th} \sim 50$ eV). If both neutrino count rate and background rate are known well, deviations from the expected rates are given by Poisson statistics. Due the large numbers both the distribution of the measured events as well as the distribution of background events can be approximated by normal distributions. If all measured events were due to background, their number n would be normal-distributed around the expected number of background events as mean:

$$p_B(n) = \frac{1}{\sqrt{2\pi B}} e^{-\frac{(n-B)^2}{2B}} \quad (1.18)$$

$$B = R_B t_0, \quad (1.19)$$

where B is the number of expected background events for a background rate R_B and an exposure t_0 . For the observation of CNNS with a confidence level CL the measured number of events has to be n_0 or larger fulfilling the

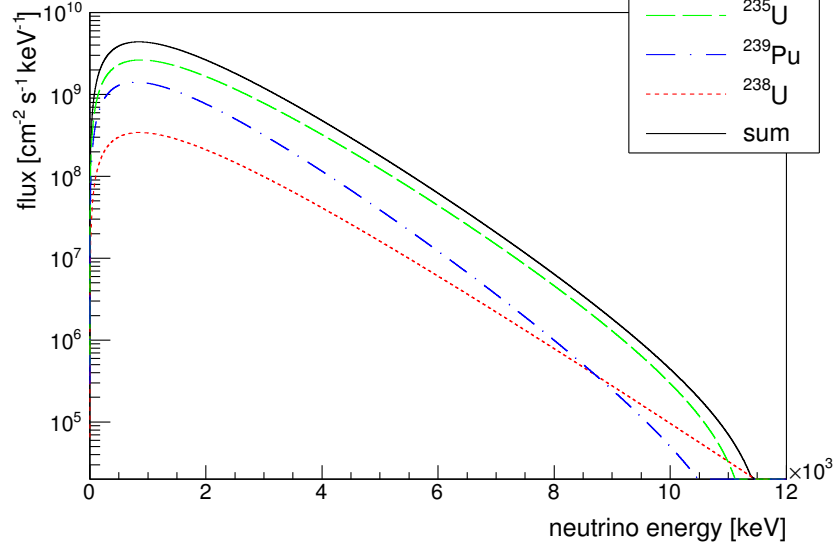


Figure 1.5: Standard energy spectrum for anti-neutrinos from pressurised water reactors. For this reactor type the fuel composition is 62% ^{235}U , 30% ^{239}Pu , and 8% ^{238}U . This fuel composition changes only little with time due to the exchange of one third of the fuel per year.

requirement:

$$P_B(n_0) = \int_{n_0}^{\infty} dn \frac{1}{\sqrt{2\pi B}} e^{-\frac{(n-B)^2}{2B}} \leq (1 - CL), \quad (1.20)$$

where $P_B(n_0)$ is the probability to observe n_0 or more background events, if all events are due to background.

The measured number of events n is normal-distributed around the sum of background and neutrino events as mean:

$$p_{SB}(n) = \frac{1}{\sqrt{2\pi(B+S)}} e^{-\frac{(n-B-S)^2}{2(B+S)}} \quad (1.21)$$

$$S = R_S t_0, \quad (1.22)$$

where S is the expected number of neutrino events for a neutrino count rate R_S and an exposure t_0 . The probability P_{SB} that the measured number of events is larger than n_0 is then given by

$$P_{SB} = \int_{n_0}^{\infty} p_{SB}(n) dn. \quad (1.23)$$

Using equations (1.20) and (1.23) the allowed background rate can be estimated. As an example, in the following the confidence level CL for an observation of CNNS is assumed to be 99.99%. Using a sapphire-based detector with

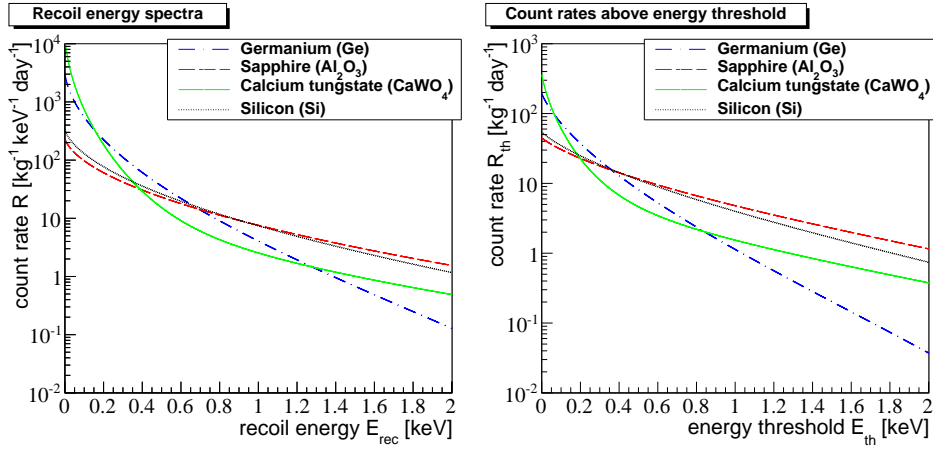


Figure 1.6: *Left*: Recoil-energy spectrum of reactor neutrinos for different target materials. For the calculation of the spectra a distance of ~ 17 m to a reactor with a thermal power of ~ 2 GW was assumed. The recoil-energy spectra for heavy targets are shifted to small recoil energies. However, the total count rate is increased ($\sigma_{tot} \propto N^2$, see equation (1.5)) for heavy target materials.

Right: Count rates R_{th} above an energy threshold E_{th} for different target materials. For energy thresholds $\lesssim 100$ eV calcium tungstate (CaWO_4) leads to the highest count rate whereas sapphire (Al_2O_3) leads to the highest count rate for energy thresholds $\gtrsim 400$ eV. For thresholds in the region between 100 and 400 eV germanium is the best target material.

an energy threshold of ~ 1.0 keV the neutrino rate is $R_S = 5.0 \text{ kg}^{-1} \text{ day}^{-1}$. Thus, for an exposure of ~ 30 kg-days the number of expected neutrino events $S = 150$. For a background rate of $\lesssim 26.1 \text{ kg}^{-1} \text{ day}^{-1}$ the n_0 obtained from equation (1.20) is sufficient, so that the probability P_{SB} to measure enough events to observe CNNS is $\gtrsim 90\%$. For an exposure of one kg-year the background rate R_B can even be $\lesssim 333.6$ background events per kg-day.

An energy threshold of ~ 1 keV is a very conservative approach. It has been shown that it is possible to reach energy thresholds between ~ 0.1 keV and ~ 0.5 keV with sapphire based cryogenic detectors[19][20]. In chapter 2 a setup for the observation of CNNS using an array of 125 sapphire based detectors with a mass of ~ 32 g each and an energy threshold of ~ 0.5 keV is described. The target mass of this setup is ~ 4 kg leading to ~ 40 neutrino events per day for the standard reactor³ scenario. The allowed background rate for this setup and the standard reactor scenario is $\sim 7.8 \cdot 10^3$. With a good background suppression it would also be possible to observe CNNS at a larger distance or with a smaller thermal power of the reactor.

Reactor	Thermal power	Distance	R_S	R_B	P_{SB}
Standard	2 GW	17 m	11.5	$7.8 \cdot 10^3$	90 %
CHOOZ[21]	4.270 GW	40 m	4.5	$1.2 \cdot 10^3$	90 %
ISAR-2[21]	3.950 GW	40 m	4.1	$1.0 \cdot 10^3$	90 %
FRM II[22]	20 MW	8 m	0.5	$1.6 \cdot 10^1$	90 %
Standard	2 GW	17 m	11.5	$1.1 \cdot 10^4$	66 %
CHOOZ[21]	4.270 GW	40 m	4.5	$1.7 \cdot 10^3$	66 %
ISAR-2[21]	3.950 GW	40 m	4.1	$1.5 \cdot 10^3$	66 %
FRM II[22]	20 MW	8 m	0.5	$2.3 \cdot 10^1$	66 %
Standard	2 GW	17 m	11.5	$1.4 \cdot 10^4$	50 %
CHOOZ[21]	4.270 GW	40 m	4.5	$2.1 \cdot 10^3$	50 %
ISAR-2[21]	3.950 GW	40 m	4.1	$1.8 \cdot 10^3$	50 %
FRM II[22]	20 MW	8 m	0.5	$2.9 \cdot 10^1$	50 %

Table 1.5: An array of 125 sapphire based detectors with an energy threshold of ~ 0.5 keV and a mass of ~ 32 g each was assumed for the estimation of the allowed background rate R_B . Both the neutrino rate R_S and the background rate R_B are given in [$\text{kg}^{-1} \text{ day}^{-1}$]. The allowed background rate R_B was estimated for different probabilities P_{SB} to observe enough events.

In table 1.5 the allowed background rates are listed for different reactor sites and also for different probabilities P_{SB} to observe enough events.

³17m distance to a 2 GW reactor.

The two power plants CHOOZ[21] in France and ISAR-2[21] in Germany have both a thermal power of ~ 4 GW. At larger distances from the reactor core both technical and security issues are easier to handle. Furthermore, the background rate correlated to the reactor is much smaller. Thus, for the estimation of the allowed background a distance of 40 m was assumed for both reactors.

Since the FRM II[22] is a research facility the setup of an experiment near the reactor core is less complicated as for commercial power plants. Another advantage of the FRM II is the short time between reactor-off periods (~ 60 days)⁴. So the background rate can be determined more precisely and at several times in a year. An experiment using the FRM-II would be a good opportunity to study the background spectrum close to a reactor core for a running reactor and also for reactor-off periods. However, due to the small neutrino flux the observation of CNNS using the FRM II requires a very good background suppression by a factor of ~ 100 (see table 1.5).

It is important to note that if the background rate is not correlated with the power reactor, i.e. the background rate is similar for a running reactor as for a not-running reactor, it is possible to determine the background rate precisely during the reactor-off periods. However, for experimental sites very close to the reactor core this assumption might not hold. It is still possible to determine the background rate if the shape of the background spectrum does not or only slightly change. This can be monitored at energies $\gtrsim 4$ keV where no significant number of neutrino events is expected (only $\sim 1.5\%$ of the neutrino events expected for sapphire as target material and an energy threshold of 0.5 keV have energies above 4 keV).

Thus, the site of the experiment has to be chosen in such a way that the background rate and the shape of the background spectrum is not or only slightly correlated with the state of the power reactor. A more detailed discussion of different background sources and their suppression is given in chapters 5 and 6.

1.2.3 Stopped pion source

Another promising neutrino source is the pion decay at rest [23, 24]. For this source an intense proton beam with proton energies between 650 and 1500 MeV [23] is guided to a beam dump. Here, the protons produce pions. The π^+ are stopped to rest before they decay⁵. The π^+ decays into a charged

⁴The FRM II has only one reactor core. Thus, systematic uncertainties due to the operation of other cores are vanishing.

⁵The π^0 are not decaying into neutrinos. The π^- are captured by atoms and interact with their nuclei without producing neutrinos.

lepton and its corresponding neutrino. The main decay channel is (see section 10.5 in [3])

$$\pi^+ \rightarrow \mu^+ + \nu_\mu \quad (1.24)$$

$$\mu^+ \rightarrow e^+ + \bar{\nu}_\mu + \nu_e. \quad (1.25)$$

Only a small fraction ($\sim 10^{-4}$ [6]) of the π^+ decay directly into positrons and electron neutrinos. The energy spectra of the three neutrinos produced in the π^+ decay at rest are shown in figure 1.7.

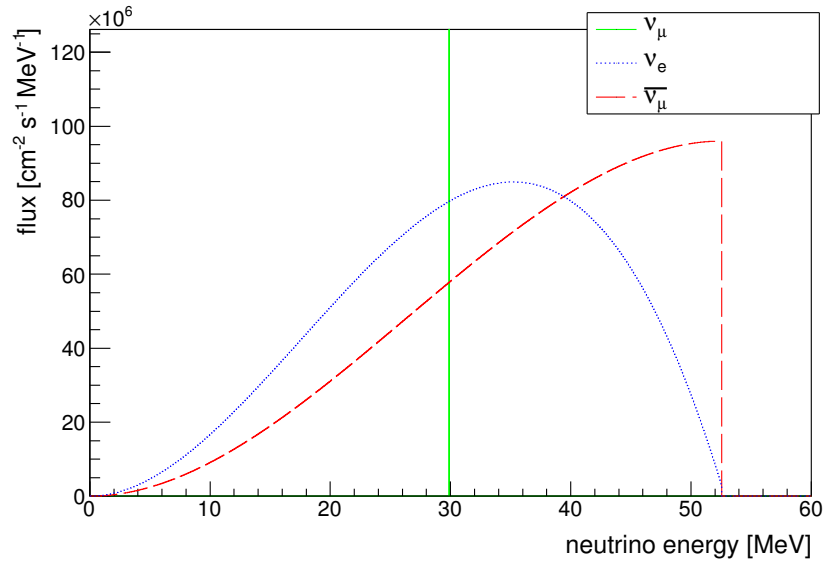


Figure 1.7: Energy spectra of neutrinos produced in the π^+ decay at rest. Only the neutrinos produced in the main decay channel (1.24) were taken into account for these spectra and the following calculations. The integrals of all three neutrino flavors are the same. For ν_e the flux is reduced for energies near the end point of the spectrum due to different helicities of the decay products and angular momentum conservation (see section 10.5 in [3] and footnote 7 for more details).

The π^+ -decay ($\pi^+ \rightarrow \mu^+ + \nu_\mu$) is a two-body decay. Thus, the ν_μ are monoenergetic with an energy E_{ν_μ} of

$$E_{\nu_\mu} = \frac{m_\pi^2 - m_\mu^2}{2m_\pi} = 29.89 \text{ MeV}, \quad (1.26)$$

where m_π is the π^+ rest mass and m_μ the μ^+ rest mass, respectively. The subsequent μ^+ -decay is a three-body decay. So the $\bar{\nu}_\mu$ and the ν_e have continuous energy spectra. Due to momentum conservation the end-point energy

of these spectra is $\frac{1}{2}(m_\mu - m_e)$ where m_e is the e^+ rest mass⁶.

The shape $\Phi_e(E_\nu)$ of the energy spectrum for the ν_e is - in the standard model - given by[25]

$$\Phi_e(E_\nu) = \frac{m_\mu^5 G_F^2}{16\pi^3} (F_1(y) + \eta x_0 F_3(y)) \frac{dE_\nu}{dy} \quad (1.27)$$

$$F_1(y) = \frac{(1 - x_0^2 - y)^2 y^2}{1 - y} \quad (1.28)$$

$$F_3(y) = \frac{(1 - x_0^2 - y)^2 y^2}{(1 - y)^2} \quad (1.29)$$

$$y = \frac{2E_\nu}{m_\mu}, \quad x_0 = \frac{m_e}{m_\mu}, \quad (1.30)$$

where $\eta = (-7 \pm 13) \cdot 10^{-3}$ [25, 26]. The flux is suppressed for energies near the end point of the spectrum due to different helicities of the decay products and angular momentum conservation[25]⁷.

Since $\bar{\nu}_\mu$ have the same helicity as e^+ the momentum distribution should be the same for both particles. The shape of the energy spectrum of $\bar{\nu}_\mu$ is given by the Michel spectrum[27, 28]

$$\Phi_\mu(E_\nu) = \frac{1}{2} \left[12x^2 - 12x^3 + \rho \left(\frac{32}{3}x^3 - 8x^2 \right) \right] \frac{dE_\nu}{dx} \quad (1.31)$$

$$x = \frac{E_\nu}{E_{\nu, max}}, \quad (1.32)$$

where $\rho = \frac{3}{4}$ in the standard model[25, 28]. In contrast to the ν_e spectrum the flux of $\bar{\nu}_\mu$ is highest for energies near the end point.

The left panel of figure 1.8 shows the combined recoil spectra for all neutrino flavors emitted in the π^+ decay. The right panel in figure 1.8 shows the count rate R_{th} versus the recoil energy threshold E_{th} . For the calculation of the recoil spectra as well as for the normalisation of the energy spectra shown in figure 1.7 an isotropic neutrino rate of $\sim 4 \cdot 10^{22}$ neutrinos per year and per flavour [23] was assumed. Thus, the neutrino flux for a detector located at a distance of 2 m to the stopped-pion source (beam dump) is

⁶If one neutrino would have more than half of the energy released in the μ^+ decay, $(m_\mu - m_e)$ momentum conservation would not be possible due to the too small momenta of the other neutrino and the positron.

⁷In the rest frame of the μ^+ , the angle between the momentum of the ν_e and the momenta of the e^+ and the $\bar{\nu}_\mu$ has to be 180° for an ν_e energy near the end point. However, due to different helicities (left-handed ν_e , right-handed for e^+ and $\bar{\nu}_\mu$) spin conservation is violated. Thus, the flux of energies near the end point is suppressed (see section 10.5 in [3] for more details).

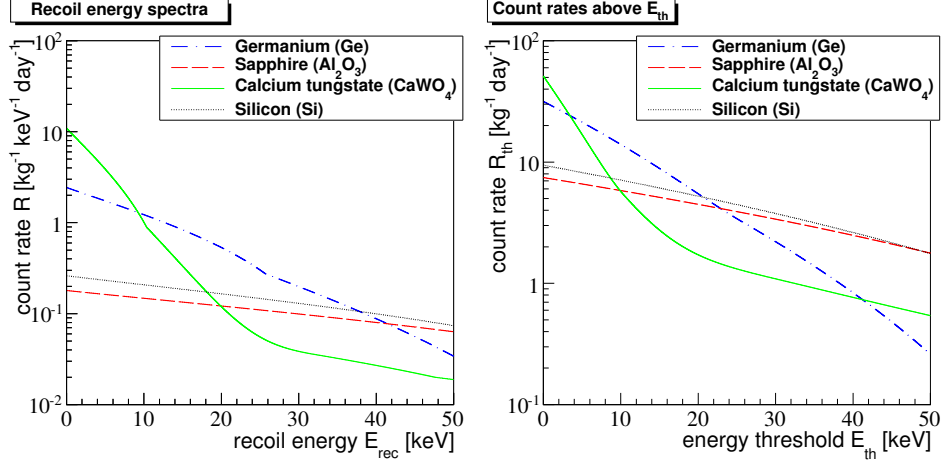


Figure 1.8: *Left:* Combined recoil energy spectra for all neutrinos from the π^+ -decay at rest for different target materials.

Right: Count rates above an energy threshold E_{th} for different target materials. Since a stopped pion source can be built in underground laboratories, experiments for direct dark matter searches could also be used for the observation of CNNS. The CDMS II experiment[29] (germanium-based low-temperature detectors) could detect ~ 2700 CNNS events with an exposure of 194.1 kg-days (see main text). For the same exposure only 2 background events were observed[29].

$\sim 2.5 \cdot 10^9 \text{ cm}^{-2} \text{ s}^{-1}$ for each neutrino flavour which is by a factor of $\sim 10^4$ smaller than the flux of reactor neutrinos in the standard scenario (distance of $\sim 17 \text{ m}$ to a reactor with a thermal power of $\sim 2 \text{ GW}$).

However, due to the E_ν^2 dependence of the cross section (see equation (1.5)) the larger neutrino energies produced in both the π^+ decay and the μ^+ decay are leading to comparable count rates for very small energy thresholds. For high recoil energies the count rates are significantly higher than for reactor neutrinos (see section 1.2.2). Thus, even detectors with an energy threshold of $E_{\text{th}} \sim 10 \text{ keV}$ are able to observe CNNS (e.g. for germanium ~ 14 counts per kg-day are expected for the neutrino flux quoted above).

Since it is also possible to build a stopped-pion source in an underground facility present experiments for direct dark matter search can be used for the observation of CNNS. The CDMS (Cryogenic Dark Matter Search)[29] experiment has an energy threshold of 10 keV and observed 2 background events in the expected region for dark matter[29]. For an exposure of 194.1 kg-days[29] ~ 2700 neutrino events from a stopped pion source as described in [23] would be expected in the same energy region. Thus, the observation of CNNS would also be possible, if the neutrino flux would be smaller by a factor of ~ 100 due to a weaker neutrino source or a larger distance between the

source and the detectors. For ~ 2700 neutrino events and only 2 background events the investigation of physics beyond the standard model like a magnetic moment of the neutrino or the search for sterile neutrinos would be possible (see chapter 7).

1.2.4 Supernova neutrinos

A further interesting neutrino source would be a core-collapse supernova (or type II supernova) in our galaxy. Such a supernova occurs at the end of the life of a massive star (mass $\gtrsim 9$ solar masses)[30]. About 99 % of the energy corresponding to $\sim 10^{53}$ erg is radiated as neutrinos of all flavours[31, 32]. Furthermore, the neutrinos are emitted promptly after the collapse, while the photon signal is delayed by several minutes to several hours[33]. The delay between the neutrino signal and the photon signal depends on the nature and the envelope of the progenitor star. Thus, a detection of neutrinos from a core-collapse supernova and the measurement of the delay between the neutrinos and the photons would lead to a better understanding of the explosion mechanisms of a core-collapse supernova[31, 32, 33]⁸.

The energy spectra $\Phi_i(E_\nu)$ of the neutrinos can be described by a Boltzmann distribution[31, 32]:

$$\Phi_i(E_\nu) = \frac{1}{4\pi d^2} \frac{N_i}{2T_i^3} E_\nu^2 e^{-\frac{E_\nu}{T_i}}, \quad (1.33)$$

where d is the distance to the supernova, N_i is the number of radiated neutrinos of flavour i , T_i is the temperature of flavour i and E_ν is the neutrino energy. The values for N_i and T_i are listed in table 1.6 for different neutrino flavours. The ν_e have more charged-current interactions than the $\bar{\nu}_e$. Thus, the $\bar{\nu}_e$ decouple in a denser region from thermal equilibrium than ν_e . So their temperature T_i is higher. All other neutrino flavours ν_x (i.e. ν_μ , ν_τ , $\bar{\nu}_\mu$ and $\bar{\nu}_\tau$) have only neutral current interactions with the matter of the collapsing star. Thus, the temperature of ν_x is the highest.

Since the released energy is distributed among all 6 neutrino flavors the neutrino numbers N_i are given by

$$\frac{1}{6} \cdot 3 \cdot 10^{53} \text{ erg} = \int_0^\infty E_\nu \frac{N_i}{2T_i^3} E_\nu^2 e^{-\frac{E_\nu}{T_i}} dE_\nu \quad (1.34)$$

$$\Rightarrow N_i = \frac{3 \cdot 10^{53} T_i}{18}. \quad (1.35)$$

⁸The delay between the arrival times of neutrinos and photons is also influenced by the neutrino masses. Thus, limits on the neutrino masses could be obtained by a measurement of the arrival times.

Flavour	N_i	T_i
ν_e	$3.0 \cdot 10^{57}$	3.5 MeV
$\bar{\nu}_e$	$2.1 \cdot 10^{57}$	5 MeV
ν_x	$5.2 \cdot 10^{57}$	8 MeV

Table 1.6: Values for neutrino numbers N_i and their temperatures T_i used in equation (1.33) for different flavours (ν_x stands for ν_μ , ν_τ , $\bar{\nu}_\mu$ and $\bar{\nu}_\tau$)[31]. The temperature is higher for $\bar{\nu}_e$ than for ν_e because the ν_e have more charged-current interactions with matter than the $\bar{\nu}_e$. Thus, the $\bar{\nu}_e$ decouple in a denser and therefore hotter region than the ν_e [33]. The ν_x have only neutral-current interactions and, thus, they have the highest temperature.

The energy spectra of ν_e , $\bar{\nu}_e$ and ν_x are shown in figure 1.9. The different temperatures T_i of the Boltzmann distributions used for these spectra as given in table 1.6 are leading to different mean energies for different flavors, e.g., ν_e have the smallest temperature and, thus, also the smallest mean energy. For the calculation of these spectra as well as for the calculation of the recoil spectra shown in figure 1.10 a distance of 10 kpc was used, since this is the distance with the highest probability for a core-collapse supernova[32, 31].

The recoil-energy spectra shown in the left panel of figure 1.10 have a similar shape. The materials with the highest count rates are xenon and calcium tungstate.

The expected number of neutrino events shown in the right panel of figure 1.10 is very low (only a few events per ton) compared to reactor neutrinos (see section 1.2.2) or neutrinos from the π^+ decay (see section 1.2.3). However, the detectors can be mounted in underground laboratories to suppress background events. So experiments for direct dark matter searches can be used to detect supernova neutrinos and thus CNNS.

In table 1.7 the expected event numbers for supernova neutrinos are listed. The target masses of the present experiments CRESST[34], SuperCDMS (Phase A)[35], and XENON100[36] are too small to observe events from a core-collapse supernova in our galaxy. The planned next-generation experiments EURECA[37], SuperCDMS(Phase C)[35] and XENON1T[40] have ton-scale target masses. The EURECA experiment consists of two target materials CaWO_4 [38] and Ge[39]. In table 1.7 the event numbers for both materials are listed separately. For the calculation of the count rates for the next-generation dark matter searches it was assumed that the energy thresholds of the current experiments can be achieved also for the much

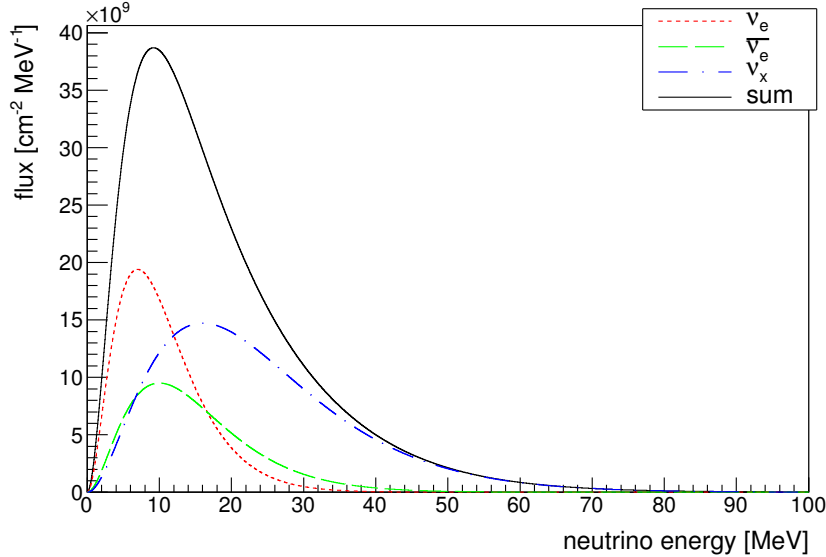


Figure 1.9: Energy spectra of supernova neutrinos for a supernova in a distance of 10 kpc and an energy release of $\sim 3 \cdot 10^{53}$ erg[31]. This released energy is distributed equally among the 6 neutrino flavors. The temperatures T_i of the Boltzmann distributions are correlated with the number of interactions of a flavor neutrino with matter. ν_e decouple in less dense regions than $\bar{\nu}_e$ and the other flavors ν_x . Thus, the ν_e distribution has a lower temperature and the mean energy is smaller than for the other flavors.

larger next-generation experiments⁹.

The expected event numbers (only ~ 2 for SuperCDMS(Phase C) and XENON1T) are too small for a study of the explosion mechanism of core-collapse supernovae. However, due to the small background rate (only a few events per year) the detection of a few neutrino events within ~ 10 s would be a strong evidence for the observation of CNNS, since the cross sections for other neutrino interactions are much smaller.

⁹For the energy threshold of the germanium-based detectors for EURECA the threshold (~ 20 keV) of the EDELWEISS detectors[39] was used.

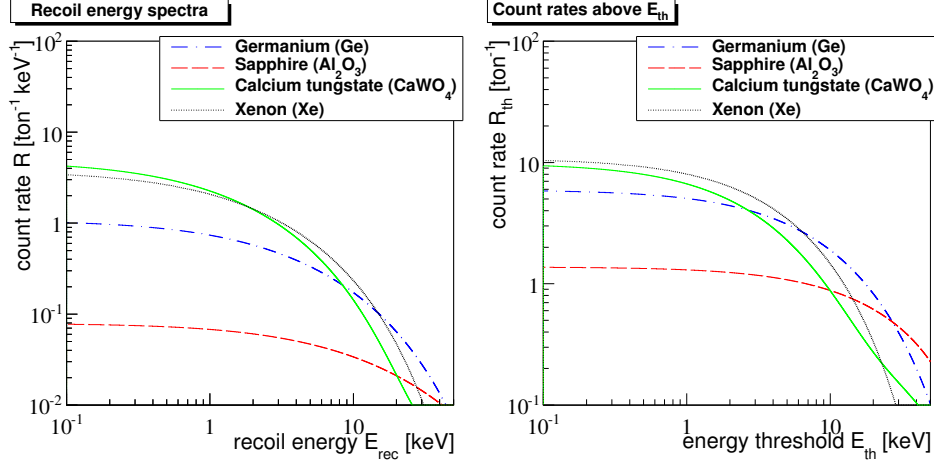


Figure 1.10: *Left:* Recoil energy spectra of supernova neutrinos for different target materials used in direct dark matter searches.

Right: Count rates above an energy threshold E_{th} for different target materials. For the detection of supernova neutrinos ton-scale target masses are needed. Thus, next-generation experiments for direct dark matter searches can be used to detect supernova neutrinos via CNNS. Although the expected event numbers (~ 2) are too small for a study of the explosion mechanism of core-collapse supernovae, a detection of a few neutrino events within ~ 10 s would be a strong evidence for CNNS, since the cross sections for other neutrino interactions are much smaller.

Experiment	Material	Mass	Threshold	ν events
CRESST[34]	CaWO_4	10 kg	12 keV	$6.5 \cdot 10^{-3}$
SuperCDMS (Phase A)[35]	Ge	25 kg	10 keV	$4.7 \cdot 10^{-2}$
XENON100[36]	Xe	48 kg	8.4 keV	$9.1 \cdot 10^{-2}$
EURECA(CaWO_4)[37, 38]	CaWO_4	0.5 ton	12 keV	0.3
EURECA(Ge)[37, 39] ⁹	Ge	0.5 ton	20 keV	0.4
SuperCDMS (Phase C)[35]	Ge	1 ton	10 keV	1.9
XENON1T[40]	Xe	1 ton	8.4 keV	1.9

Table 1.7: Expected supernova-neutrino events for different experiments for direct dark matter searches. The target mass of the current experiments is too small for the detection of supernova neutrinos. The next-generation experiments with ton-scale target masses could detect a few events from a supernova at a distance of 10kpc. Due to the low background rate, this observation would be a strong hint for CNNS, since the cross sections for other neutrino interactions are much smaller.

Chapter 2

Low-temperature detectors for the observation of CNNS

The expected CNNS count rates for different sources and target materials were calculated in chapter 1. The choice of the target material used for the observation of CNNS depends also on the type of the detector which is used.

Liquid noble gas detectors[36, 41, 42] use noble gases like argon or xenon as target material. The advantage of this type of detector is the easy scalability. Thus, large target masses up to $\mathcal{O}(\text{tons})$ can be reached. However, the energy thresholds $\mathcal{O}(10 \text{ keV})$ of the current detectors are too high[36, 41, 42] to observe CNNS.

A further well known type of detectors are semiconductor detectors based on germanium or silicon[43, 44]. The energy thresholds $\mathcal{O}(\text{keV})$ of these detectors are, however, also too high to observe CNNS.

Low-temperature detectors can be built from a lot of different materials, e.g. semiconductors[29, 39] like germanium or insulators like calcium tungstate [38] and sapphire[19, 20]. It has already been shown that the recoil-energy thresholds of low-temperature detectors can be low enough[19, 20] to observe CNNS. Thus, for the present work only low-temperature detectors were taken into account.

The most promising target materials to observe CNNS using low-temperature detectors are germanium and sapphire (see section 1.2.2). Sapphire has good phononic properties and it has already been shown that low energy thresholds $\mathcal{O}(0.1 \text{ keV})$ are possible with sapphire crystals. Since the phononic properties of germanium are not as good as the properties of sapphire, it is very difficult to build germanium-based low-temperature detectors with energy thresholds of $\lesssim 0.4 \text{ keV}$. Thus, for the present work only sapphire was used as target material.

A low-temperature detector consists of a target crystal and a sensitive

thermometer used to read out the temperature rise caused by an energy deposition in the target crystal. Figure 2.1 shows the setup of the low-

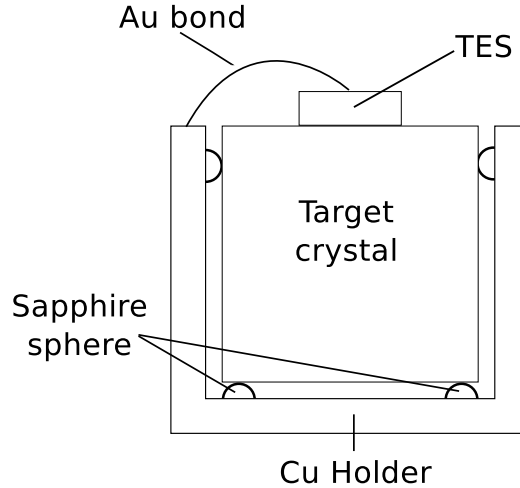


Figure 2.1: Basic setup of low-temperature detectors used for this work. The Transition Edge Sensor (TES) is used to measure the small temperature rise caused by an energy deposition inside the target crystal. The TES has a weak thermal coupling via a thin gold wire to the copper holder which serves as a heat sink. The target crystal is mounted to the copper holder using small sapphire spheres to minimize the thermal coupling between target crystal and copper holder.

temperature detector used for this work. The target crystal is mounted inside a copper holder using sapphire spheres. The sapphire spheres are used to minimize the thermal coupling between the target crystal and the copper holder. For this work a Transition Edge Sensor (TES, see section 2.2) was used to measure the temperature rise. The TES has a weak thermal coupling to the copper holder via a thin gold wire. Due to its large mass the copper holder serves as a heat sink for the TES and the target crystal.

2.1 Thermal model for low-temperature detectors

The energy deposited in the target crystal by an incident particle is converted into high-frequency optical phonons. These optical phonons are decaying into acoustical phonons on a time scale of a few 100 ps[45, 46]. The energy distribution of these high-frequency acoustical phonons is almost monoenergetic[45, 46] with a frequency of about half the Debye frequency¹.

¹For sapphire the Debye frequency is ~ 21.7 THz[46].

Due to the high frequencies these acoustical phonons are decaying rapidly into phonons with smaller frequencies via anharmonic three-phonon processes[46]. The decay rate Γ of anharmonic three-phonon processes strongly depends on the phonon frequency ω ($\Gamma \propto \omega^5$). After $\sim 10 \mu\text{s}$ the acoustical phonons with initial frequencies of $\mathcal{O}(10 \text{ THz})$ have a mean energy corresponding to frequencies of $\sim 600 \text{ GHz}$ [45, 46] and they are distributed homogeneously in the target crystal². These phonons are called non-thermal because frequencies of $\sim 600 \text{ GHz}$ correspond to a Planck distribution with a temperature of 10 K [46]. Due to the small decay rate ($\Gamma \propto \omega^5$) for low frequencies it takes $\sim 1 \text{ ms}$ for the non-thermal phonons to decay to even smaller frequencies. If the frequency distribution of the phonon population corresponds to a Planck distribution with a temperature near the operation temperature of the target crystal ($\mathcal{O}(10 \text{ mK})$), the non-thermal phonons are thermalized and thus called thermal phonons.

The typical collection times of the TES are $\mathcal{O}(100 \mu\text{s})$ [46]. Thus, a fraction ϵ of the non-thermal phonon population does not thermalize in the target crystal but in the TES leading to a thermal power input $P_e(t)$ into the electron system of the TES. The rest of the non-thermal phonons are thermalizing in the target crystal leading to a power input $P_a(t)$ into the thermal phonon system of the target crystal.

The power input $P_e(t)$ into the electron system of the TES is given by[45, 46]:

$$P_e(t) = \Theta(t)P_0e^{-\frac{t}{\tau_n}} \quad (2.1)$$

$$P_0 = \frac{\epsilon E_0}{\tau_n}, \quad (2.2)$$

where $\Theta(t)$ is the Heaviside function³, E_0 is the energy deposited in the target crystal by the incident particle, τ_n is the thermalization constant for the non-thermal phonon population and ϵ is the fraction of non-thermal phonons thermalizing in the TES. The thermalization constant τ_n depends on the size and the material of the TES as well as on the dimensions of the target crystal.

The power input $P_a(t)$ into the thermal phonon system of the target

²The average sound velocity for sapphire is $\sim 6500 \frac{\text{m}}{\text{s}}$ [45, 46]. The dimensions of the crystal are $\mathcal{O}(10 \text{ mm})$. So, after several reflections at the crystal surfaces ($\sim 6 \mu\text{s}$ [46, 47]) the phonons are equally distributed in the target crystal.

³Due to the fast decay of high-frequency phonons ($\sim 10 \mu\text{s}$) compared to the rise time of the signal ($\lesssim 1 \text{ ms}$) it was assumed that a homogeneous phonon distribution exists instantly after the energy deposition. This assumption is expressed by the Heaviside function $\Theta(t)$.

crystal is given by[45, 46]:

$$P_a(t) = \frac{1 - \epsilon}{\epsilon} P_e(t). \quad (2.3)$$

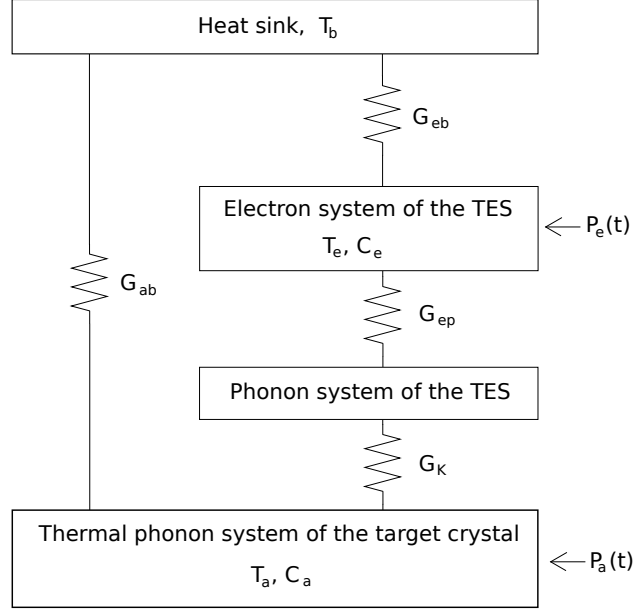


Figure 2.2: Thermal model of a low-temperature detector. T_b is the temperature of the heat sink (copper holder), T_a is the temperature of the thermal phonon system of the target crystal and T_e is the temperature of the electron system of the TES, C_a and C_e are their respective heat capacities. G_{ab} , G_{eb} , G_{ep} and G_K are the respective thermal couplings (see main text for further details). $P_e(t)$ is the power input into the electron system of the TES and $P_a(t)$ is the power input into the phonon system of the target crystal, respectively.

Figure 2.2 shows a thermal model for low-temperature detectors. The thermal phonon system of the target crystal (temperature T_a , heat capacity C_a) is coupled to the phonon system of the TES via Kapitza coupling G_K [45, 46]. The phonon and the electron systems of the TES (temperature T_e , heat capacity C_e) are coupled via G_{ep} . The electron system of the TES is coupled to the heat sink (temperature T_b) via G_{eb} , i.e., the gold bond wire shown in figure 2.1. The thermal phonon system of the target crystal is also directly coupled to the heat sink via G_{ab} , i.e., the sapphire spheres shown in figure 2.1.

Since the heat capacity of the phonon system of the TES is very small, an effective coupling G_{ea} between the thermal phonon system of the target

crystal and the electron system of the TES can be introduced[45, 46]:

$$G_{ea} = \left(\frac{1}{G_{ep}} + \frac{1}{G_K} \right)^{-1}. \quad (2.4)$$

The thermal model for low-temperature detectors shown in figure 2.2 can be described by a system of two coupled differential equations for the temperatures T_e and T_a of the electron system of the TES and the thermal phonon system of the target crystal, respectively[45, 46]:

$$C_e \frac{dT_e(t)}{dt} (T_e(t) - T_a(t)) G_{ea} + (T_e(t) - T_b) G_{eb} = P_e(t) \quad (2.5)$$

$$C_a \frac{dT_a(t)}{dt} (T_a(t) - T_e(t)) G_{ea} + (T_a(t) - T_b) G_{ab} = P_a(t). \quad (2.6)$$

For the initial conditions $T_e(t=0) = T_a(t=0) = T_b$ this system can be solved[45, 46] by:

$$T_e(t) = T_b + \Delta T_e(t) \quad (2.7)$$

$$\Delta T_e(t) = \Theta(t) \left[A_n \left(e^{-\frac{t}{\tau_n}} - e^{-\frac{t}{\tau_{in}}} \right) + A_t \left(e^{-\frac{t}{\tau_t}} - e^{-\frac{t}{\tau_n}} \right) \right], \quad (2.8)$$

where the intrinsic time constant τ_{in} of the TES and the thermal relaxation time τ_t of the combined system are given by[46]:

$$\tau_{in} = \frac{1}{\lambda_{in}} = \frac{2}{a + \sqrt{a^2 - 4b}} \quad (2.9)$$

$$\tau_t = \frac{1}{\lambda_t} = \frac{2}{a - \sqrt{a^2 - 4b}}, \quad (2.10)$$

with the constants a and b [46]:

$$a = \frac{G_{ea} + G_{eb}}{C_e} + \frac{G_{ea} + G_{ab}}{C_a} \quad (2.11)$$

$$b = \frac{G_{ea}G_{eb} + G_{ea}G_{ab} + G_{eb}G_{ab}}{C_e C_a}. \quad (2.12)$$

The non-thermal and thermal amplitudes A_n and A_t are given by[46]:

$$A_n = \frac{E_0 \left(\lambda_{in} - \frac{G_{ab}}{C_a} \right)}{\tau_n (\lambda_t - \lambda_{in}) (\lambda_{in} - \lambda_n)} \left(\frac{\lambda_t - \frac{G_{ab}}{C_a}}{G_{eb} - G_{ab} \frac{C_e}{C_a}} - \frac{\epsilon}{C_e} \right) \quad (2.13)$$

$$A_t = \frac{E_0 \left(\lambda_t - \frac{G_{ab}}{C_a} \right)}{\tau_n (\lambda_t - \lambda_{in}) (\lambda_t - \lambda_n)} \left(\frac{\lambda_{in} - \frac{G_{ab}}{C_a}}{G_{eb} - G_{ab} \frac{C_e}{C_a}} - \frac{\epsilon}{C_e} \right). \quad (2.14)$$

Depending on the ratio between τ_{in} and the decay time τ_n of the non-thermal component there are two different modes for a low-temperature detector. For a detector where $\tau_{in} \ll (\tau_n, \tau_t)$ the intrinsic time constant τ_{in} is the fast rise time of the pulse, τ_n is the fast decay time of the non-thermal component and τ_t is the slow decay time of the thermal component[45]. In this mode the non-thermal component is proportional to the power input $P_e(t)$ and the TES works as a bolometer measuring the flux of non-thermal phonons[45]. Thus, the integral over the pulse is proportional to the deposited energy. Since all time constants τ_{in} , τ_n and τ_t are independent of the deposited energy and only the amplitudes A_n and A_t are energy dependent, the height of the pulse is also proportional to the deposited energy.

On the other hand, if $\tau_{in} \gg \tau_n$, the non-thermal amplitude A_n (see equation (2.13)) becomes negative and the non-thermal time constant τ_n is the rise time of both components of the pulse (see equation (2.8)). Thus, all non-thermal phonons are collected in the TES before the heat is dissipated to the heat sink. In this mode the TES behaves like a calorimeter measuring the integrated power input $P_e(t)$. Thus, the pulse height is proportional to the deposited energy and independent of the decay times τ_{in} and τ_t . However, the pulse height strongly depends on the heat capacity of the TES.

For both modes the pulse height is proportional to the deposited energy:

$$\Delta T_e \propto E_0. \quad (2.15)$$

The thermal model presented in this section can not directly be compared with measured pulses because several effects⁴ on the pulse shape are not taken into account. However, the pulse shape given by equation (2.8) is still a good model for most low-temperature detectors. To fit this pulse shape to a measured standard event⁵ equation (2.8) has to be expanded by a time offset t_0 :

$$A(t) = \Theta(t - t_0) \left[A_n \left(e^{-\frac{t-t_0}{\tau_n}} - e^{-\frac{t-t_0}{\tau_{in}}} \right) + A_t \left(e^{-\frac{t-t_0}{\tau_t}} - e^{-\frac{t-t_0}{\tau_n}} \right) \right]. \quad (2.16)$$

Figure 2.3 shows the fit of equation (2.16) to the averaged pulse shape (see section 4.2) of the low-temperature detector used for the measurements described in chapter 3. The parameters obtained by this fit are listed in table 2.1. The non-thermal amplitude A_n is positive and $\tau_{in} \ll \tau_n, \tau_t$. Thus, this low-temperature detector behaves like a bolometer measuring the flux of non-thermal phonons through the TES.

⁴e.g., electro thermal feedback[48], finite thermal conductance along the TES[45], electric filters for data acquisition.

⁵A standard event is the average of several pulses. See chapter 4 for further details.

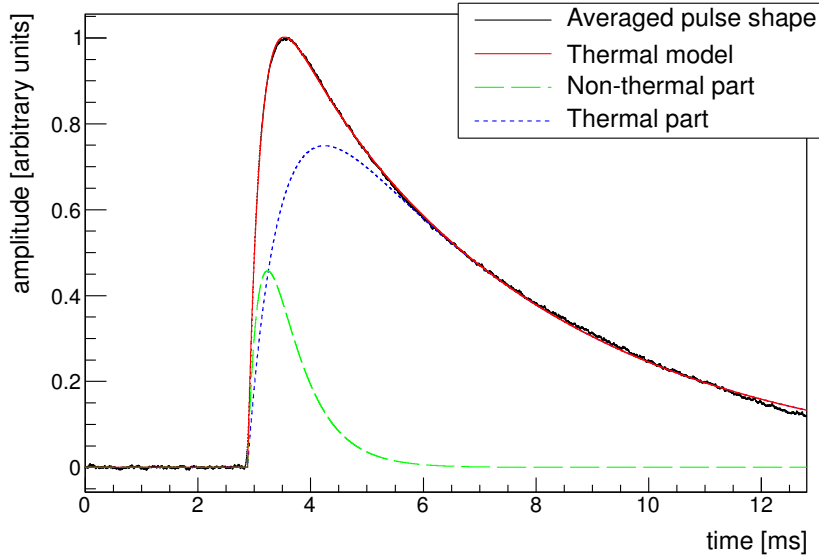


Figure 2.3: Fit of equation (2.16) to the pulse shape of the low-temperature detector used for this work (see chapter 3). The non-thermal component of the detector is smaller than the thermal component leading to a bad sensitivity of the detector. See main text for further details.

The non-thermal part of the pulse is much smaller than the thermal part. This indicates a small collection efficiency for non-thermal phonons. If the non-thermal part of the pulse were larger, the pulse would be faster and also higher. Thus, to improve the low-temperature detector used for this work the collection efficiency of non-thermal phonons has to be increased. This can be achieved by increasing the area covered by the TES.

However, a larger TES has also a larger heat capacity C_e leading to a smaller ΔT_e ⁶. The use of phonon collectors[49] can be a solution to this problem. A phonon collector is a structure attached to the TES. The phonon collector is superconducting at the operation temperature T_b of the TES. Since superconducting materials have no heat capacity, the heat capacity C_e of the TES is not increased by a phonon collector. If a phonon reaches the phonon collector it produces quasi-particles by exciting Cooper-pairs[49]. These quasi-particles are diffusing through the phonon collector and can enter the TES where they are thermalizing. Thus, phonon collectors are increasing the effective area covered by the TES without changing its heat capacity.

⁶In the bolometric mode the heat capacity C_e is not so important for the amplitude A_n as in the calorimetric mode. However, a larger C_e also leads to a larger decay time τ_t which in turn leads to a smaller pulse height, since the integral of the pulse is proportional to the deposited energy.

Parameter	value
A_n	1.4385 ± 0.0066
A_t	1.1517 ± 0.0004
t_0	(2.8807 ± 0.0001) ms
τ_{in}	(0.2349 ± 0.0006) ms
τ_n	(0.5742 ± 0.0063) ms
τ_t	(4.5999 ± 0.0015) ms

Table 2.1: The parameters obtained by a fit of equation (2.16) to the measured pulse shape of the low-temperature detector used for this work (see figure 2.3). Since the non-thermal amplitude A_n is positive and $\tau_{in} \ll (\tau_n, \tau_t)$ this detector behaves like a bolometer measuring the flux of non-thermal phonons.

In the present thesis, however, phonon collectors were not used.

2.2 Transition Edge Sensor (TES)

A Transition Edge Sensor (TES) is a sensitive thermometer based on the steep phase transition between normal and superconductivity of a thin metal film. As an example figure 2.4 shows the phase transition of an iridium-gold

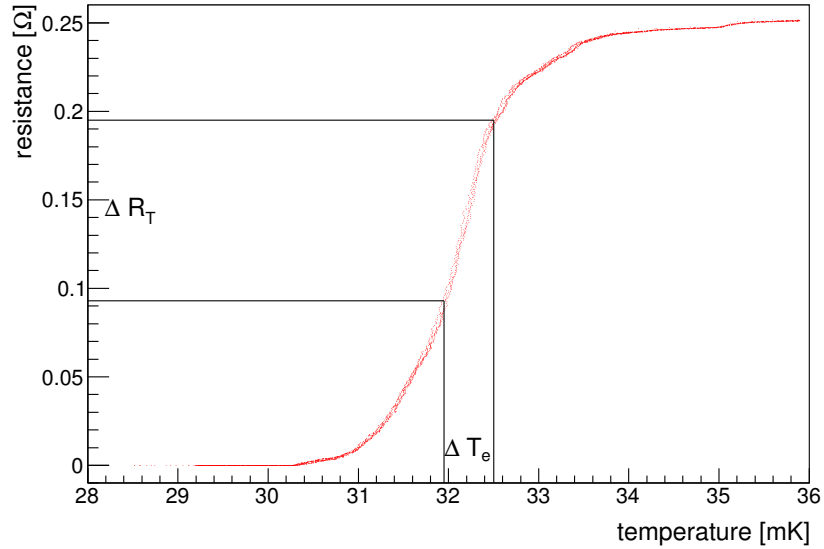


Figure 2.4: Typical phase transition between normal and superconductivity of an iridium-gold bilayer with a critical temperature $T_c \approx 32$ mK. Due to the steep transition a small rise ΔT_e in temperature leads to a large rise ΔR_T in resistance.

bilayer. The critical temperature⁷ of this transition is ~ 32 mK. Due to the steepness of the transition a small rise ΔT_e in temperature leads to a large rise ΔR_T in resistance. For temperatures near the critical temperature the phase transition is approximately linear. Thus, the resistance change ΔR_T is proportional to ΔT_e .

The TES has to be operated at temperatures near the critical temperature T_c . Due to the temperature dependence of the specific heat of both the target crystal ($\propto T^3$) and the TES ($\propto T$) the critical temperature should be as low as possible. Different materials can be used for a TES. The crystalline α -phase tungsten has a critical temperature of ~ 15 mK[34]. Depending on the environmental conditions (e.g. temperature or pressure) during the fabrication process of the TES the lattice structure can be distorted leading to critical temperatures between ~ 10 and ~ 100 mK[51]. Thus, by tuning the conditions during the fabrication process the critical temperature of thin tungsten films can be adjusted.

Another possibility to adjust the critical temperature of thin metal films is the proximity effect[52, 53]. A bilayer of a superconducting and a normal conducting metal is produced. The critical temperature T_c of this bilayer depends on the thickness of both the superconducting and the normal conducting metal. For pure iridium the critical temperature is 112 mK[53]. For an iridium-gold bilayer the critical temperature can be adjusted between 20 and 100 mK[52, 53] by varying the thickness of both the iridium and the gold layer.

For the low-temperature detector used in this work (see chapter 3) an iridium-gold bilayer with a critical temperature $T_c \lesssim 10$ mK was used as TES.

2.3 Read-out system

The rise ΔR_T in resistance is read out with a Superconducting Quantum Interference Device (SQUID, [54]). The SQUIDs used for this work are based on the DC-Josephson effect[55, 56] and are able to measure small changes of a magnetic flux very precisely.

Figure 2.5 shows the electric circuit used for the read out of the resistance rise of the TES. The resistance R_T of the TES is in series to the input coil of the SQUID system and parallel to a shunt resistance R_S ($\mathcal{O}(10 \text{ m}\Omega)$). The constant bias current I_B applied to the circuit is divided according to R_T and R_S . A change of the TES resistance R_T due to a change of the TES

⁷The $\mathcal{O}(\text{mK})$ temperatures needed for the operation of low-temperature detectors with TESs were provided by a dilution refrigerator[50].

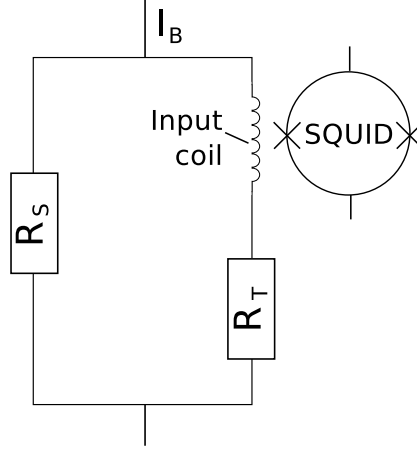


Figure 2.5: Electric read-out circuit: The TES resistance R_T is in series to the input coil of the SQUID system and parallel to a shunt resistance R_S ($\mathcal{O}(10\text{ m}\Omega)$). The constant bias current I_B is divided according to R_T and R_S . If R_T changes due to a change of the temperature of the TES also the current through R_T and thus the magnetic flux generated by the input coil is changed. This change of the magnetic flux is measured by the SQUID.

temperature leads to a change of the magnetic flux through the input coil. This flux change is measured by the SQUID.

The magnetic flux B generated by the input coil is proportional to the current I_T [57] through the right path of figure 2.5. The current I_T is given by:

$$I_T = \frac{R_S}{R_T + R_S} I_B. \quad (2.17)$$

The current change ΔI_T induced by the change ΔR_T of the TES resistance is given by:

$$\Delta I_T = \frac{\Delta R_T}{\Delta R_T (R_T + R_S) + (R_T + R_S)^2}. \quad (2.18)$$

For small ΔR_T the current change ΔI_T is proportional to ΔR_T :

$$\Delta I_T \approx \frac{1}{(R_T + R_S)^2} \cdot \Delta R_T. \quad (2.19)$$

The change ΔB of the magnetic flux is consequently proportional to the temperature change ΔT_e of the TES, if ΔR_T is small. For large ΔR_T also the phase transition between normal and superconductivity is no longer linear.

The output voltage ΔU_{SQUID} of the SQUID is proportional to the change of the magnetic flux ΔB . Thus, together with the thermal model described

in section 2.1 the height of the pulse measured with the SQUID system is proportional to the deposited energy E_0 :

$$\Delta U_{SQUID} \propto \Delta B \propto \Delta I_T \propto \Delta R_T \propto \Delta T_e \propto E_0. \quad (2.20)$$

2.4 Calibration methods

The calibration with an X-ray source is a well-known method to study the performance of a single low-temperature detector. For this method the characteristic X-ray radiation of a source is used to calibrate the detector by determining the pulse heights corresponding to the energy depositions of the different X-ray lines. A ^{55}Fe source is often used for this method (see chapter 3). ^{55}Fe decays into the ground state of ^{55}Mn via electron capture[58]. The resulting characteristic X-ray radiation of ^{55}Mn is used to calibrate the detector.

For most (massive) low-temperature detectors only the K_α (~ 5.90 keV [58]) and K_β (~ 6.49 keV[58]) lines are visible due to the low intensities of the L lines (see chapter 3). Thus, only the two K lines can be used for an energy calibration.

A more complicated fluorescence source, where a ^{55}Fe source is used to generate X-ray fluorescence of materials consisting of lighter atoms with less electrons like aluminum and titanium[59], can be used to obtain more calibration points at low energies.

However, for an experiment aimed at the observation of CNNS the calibration with X-ray sources has several disadvantages. For a compact detector array as described in the previous section it is not possible to equip all detectors with an X-ray source. Furthermore, due to the high probability for the generation of Auger-electrons ($\sim 70\%$ [58]) X-ray sources are producing background events in the energy region ($\lesssim 4$ keV) used for the observation of CNNS. Thus, X-ray sources are not suitable to test the stability of the detectors during the measurements for the observation of CNNS.

However, there are methods without radioactive sources that are appropriate for energy calibration as well as for stability tests. Two of these methods will be described in the following sections, the LED calibration and the direct TES calibration

2.4.1 LED calibration

The LED calibration is based on the Poisson statistics of the photons emitted by a pulsed Light Emitting Diode (LED). This calibration method was suc-

cessfully applied for low-temperature light detectors based on silicon crystals using a LED with a wavelength of ~ 430 nm[60].

The photons emitted by the pulsed LED are guided through a fiber optic to the target crystal of the detector. A large part of these photons is absorbed in the crystal. The energy E deposited in the target crystal is proportional to the number of absorbed photons N :

$$E = E_0 \cdot N, \quad (2.21)$$

where E_0 is the energy of one photon (~ 2.9 eV for a wavelength of ~ 430 nm). The number of absorbed photons is Poisson distributed, but due to the large number ($\gtrsim 10$) of photons needed for the calibration the distribution of the number of absorbed photons can be approximated by a normal distribution with a width of \sqrt{N} .

For the energy calibration the LED is operated with several pulse durations⁸ ($\mathcal{O}(10$ ns)). The LED-pulse durations are much shorter than the rise times of the pulses produced by low-temperature detectors (~ 1 ms) so that the energy deposition of the photons can be assumed to be instantaneous.

For each LED intensity about 500 to 2000 pulses are recorded. The peaks in the resulting pulse-height spectrum are fitted by Gaussians. There are several independent contributions to the total width σ_{tot} of these peaks. However, it is assumed that only the contribution σ_{ph} by the photon number distribution is energy dependent. All other contributions are assumed to be constant with energy and can be summed up to a width σ_0 . Thus, the total width σ_{tot} is given by:

$$\sigma_{tot} = \sqrt{\sigma_0^2 + \sigma_{ph}^2}. \quad (2.22)$$

Due to Poisson statistics the width σ_{ph} is proportional to \sqrt{N} :

$$x = a \cdot N \quad (2.23)$$

$$\sigma_{ph} = a\sqrt{N}, \quad (2.24)$$

where x is the pulse height in ADC channels and a is a scaling factor. With equation (2.22) the total width σ_{tot} can be written as

$$\sigma_{tot} = \sqrt{\sigma_0^2 + a^2 N} = \sqrt{\sigma_0^2 + ax}. \quad (2.25)$$

For an energy calibration the scaling factor a has to be determined since the energy E can be written as

$$E = E_0 N = \frac{E_0}{a} x. \quad (2.26)$$

⁸The pulse duration is proportional to the number N of absorbed photons.

To determine a , equation (2.25) has to be fitted to a set of calibration points which are given by the positions x and the widths σ_{tot} of the peaks in the pulse-height spectrum.

This method has been proven to work very well for silicon-based low-temperature light detectors[60]. However, sapphire crystals as used in the present thesis are transparent for wavelengths $\gtrsim 250$ nm[61]. Thus, to use this calibration method for the observation of CNNS all sapphire detectors have to be equipped with LEDs and also fiber optic for a wave length of ~ 250 nm. Up to now, this method was never used for sapphire-based low-temperature detectors. So, additional tests of this method are needed.

2.4.2 Direct TES calibration

For a direct TES calibration small heat pulses are applied to the TES[62] via an electrical current through a gold stripe attached to the TES. The resulting pulse height of the low-temperature detector can be compared to the pulse heights produced by external and internal radioactive sources leading to an energy calibration of the heat pulses sent directly into the TES[62]. Small heat pulses are used for calibration and linearity tests of the detectors while larger heat pulses are used to stabilize the temperature of the detectors[62].

This method has already been used for the low-temperature detectors in the experiment Cryogenic Rare Event Search with Superconducting Thermometers (CRESST)[34, 62].

2.5 Setup of a future experiment for the observation of CNNS

For the first observation of CNNS a target mass of $\mathcal{O}(\text{kg})$ is needed (see section 1.2.2). As was already pointed out in chapter 1 it is very difficult to produce a low-temperature detector with a recoil-energy threshold of $\lesssim 0.5$ keV and a mass of ~ 1 kg. Thus, it might be convenient to produce a larger number of low-temperature detectors with small target masses.

It has been shown that it is possible to produce sapphire-based low-temperature detectors with a mass of ~ 32 g and a recoil-energy threshold $\lesssim 0.1$ keV[19]. For the setup presented in this section, $20 \times 20 \times 20$ mm³ sapphire crystals with a mass of ~ 32 g were used. Figure 2.6 shows a possible setup of 125 sapphire crystals leading to a total target mass of ~ 4 kg.

Each detector is equipped with a TES which is connected to a SQUID read out circuit (see figure 2.5) by two superconducting wires. These two wires are arranged as a shielded twisted pair cable to minimize electronic

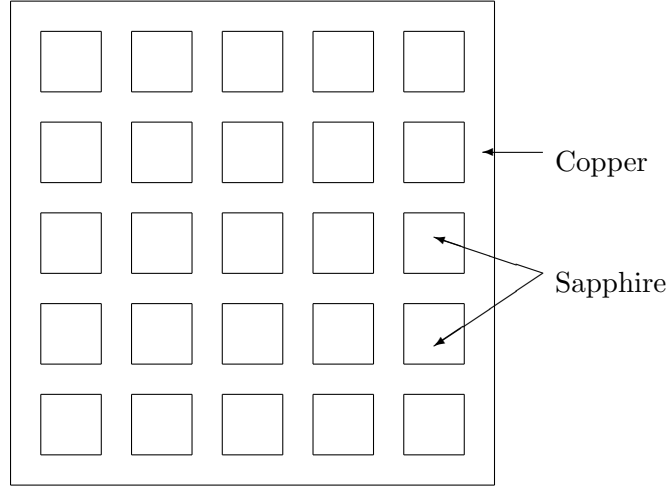


Figure 2.6: One plane of the detector array suggested for the first observation of CNNS. Every plane consists of 5x5 sapphire-based low-temperature detectors mounted in a copper lattice. Each detector consists of a $20 \times 20 \times 20 \text{ mm}^3$ sapphire crystal with a mass $\sim 32 \text{ g}$. The complete detector array consists of 5 such planes leading to a target mass of $125 \cdot 32 \text{ g} \approx 4 \text{ kg}$.

noise. Thus, 125 twisted pair cables are needed for the SQUID read-out of the complete detector array.

Since the critical temperatures of all TESs are slightly different the operation temperatures of all detectors have to be adjusted individually for each detector. For the detector used for the present work the operation temperature was adjusted by a thermometer and a heater mounted to the copper holder. However, this is not possible for a detector array because all detectors are mounted to the same copper structure. To solve this problem all TESs can be equipped with a gold stripe to heat the TES directly by applying a small constant current to the gold stripe. By applying additional pulses to the gold stripe the temperature stability of the TESs can be monitored and improved[62]. For this heating and temperature stabilization method two additional superconducting wires are needed for every TES. Thus, in total the detector array has to be connected to 500 superconducting wires arranged in 250 shielded twisted pair cables.

In addition to the cables connected directly to the detector array, every TES has its own SQUID read out circuit with its own bias current. Thus, 125 more shielded twisted pair cables are needed for the bias currents. Furthermore, every detector has to be read out by a SQUID. So 125 SQUIDs are required to read out all detector channels. Every SQUID requires 3 shielded twisted pair cables for its operation. Thus, in total there are 500 additional

shielded twisted pair cables needed to read out all 125 low-temperature detectors, i.e., altogether 750 cables.

It is possible to reduce the number of cables needed for the read-out of the detectors by using a multiplexed read-out system[63]. With such a multiplexed system several detectors can be read out by one SQUID and so the number of cables is reduced drastically. There are two different multiplexing schemes. At time-domain multiplexed systems the detectors are read out sequentially one detector at a time. Since the revisit rate, i.e., the rate between two consecutive read-outs of the same detector, is much higher than the frequencies occurring in the signals produced by low-temperature detectors ($\mathcal{O}(10\text{ kHz})$), the output signals of several detectors can be sampled with sufficient accuracy[63].

With frequency-domain multiplexed systems every detector is biased by a unique $\sim\text{MHz}$ carrier wave[63] and so every detector has its own region in frequency space. Thus, all detectors can be read out simultaneously. Since both electronic and microphonic noise have mainly frequencies $\lesssim 100\text{ kHz}$ [62, 63] frequency-domain multiplexed systems are also able to reduce the noise level.

For the detector array shown in figure 2.6, 125 low-temperature detectors have to be produced. If their TESs are evaporated directly onto the crystal similar to the detector used for this work (see chapter 3), it would take about one year to produce all 125 detectors assuming that two detectors are produced per week and that all produced detectors can be used for the observation of CNNS. By using the composite detector design[51] it is possible to reduce this time drastically. For the composite detector design the TES is not directly evaporated onto the target crystal but onto a small carrier substrate, e.g. a $10\times 10\text{ mm}^2$ sapphire substrate for a $6\times 4\text{ mm}^2$ TES. This carrier substrate is then glued onto the target crystal. Since the carrier substrates are much smaller than the target crystals, it is possible to process several carrier substrates simultaneously. Thus, about four detectors can be produced per week.

Furthermore, it is also possible to measure the phase transitions of the TESs before the carrier substrates are glued to the target crystals. The poor TESs can be rejected before they are glued onto a target crystal. Thus, the efficiency for producing good detectors is improved.

Chapter 3

Measurements with a low-temperature detector

For the measurements presented in this chapter a low-temperature detector based on a $10 \times 20 \times 40 \text{ mm}^3$ sapphire crystal with a mass of $\sim 32 \text{ g}$ was produced. The detector was equipped with an iridium-gold TES (see section 2.2) which was evaporated directly onto the sapphire crystal. The TES covers an area of $6 \times 4 \text{ mm}^2$ and is made up of a structure of three layers. The first $\sim 5 \text{ nm}$ thick iridium layer is used to compensate the different lattice constants of sapphire and iridium. This layer was evaporated at a temperature of $\sim 300 \text{ }^\circ\text{C}$ to increase the mobility of the iridium atoms so that dislocations in the iridium lattice can be removed.

The second layer is a gold layer with a thickness of $\sim 80 \text{ nm}$. This gold layer was evaporated at a temperature of $\sim 150 \text{ }^\circ\text{C}$ to reduce the diffusion of gold atoms into the iridium layer.

The last layer is $\sim 40 \text{ nm}$ thick and consists again of iridium. This iridium layer was evaporated at a temperature of $\sim 30 \text{ }^\circ\text{C}$ to avoid diffusion of the gold atoms of the second layer into this iridium layer.

After the evaporation of the three layers the detector was annealed in vacuum for about two hours at a temperature of $\sim 220 \text{ }^\circ\text{C}$ to reduce the number of dislocations in the iridium and gold layers.

The full phase transition of this TES could not be measured since its critical temperature is below the base temperature ($\sim 10 \text{ mK}$) of the cryostat used for the measurements described in this chapter. However, due to the finite width of the phase transition it was still possible to operate this detector at a temperature close to the base temperature of the cryostat.

Figure 3.1 shows the setup of the low-temperature detector used for the measurements presented in this chapter. The left panel shows the top view the right panel the cross section of the setup. The target crystal, a

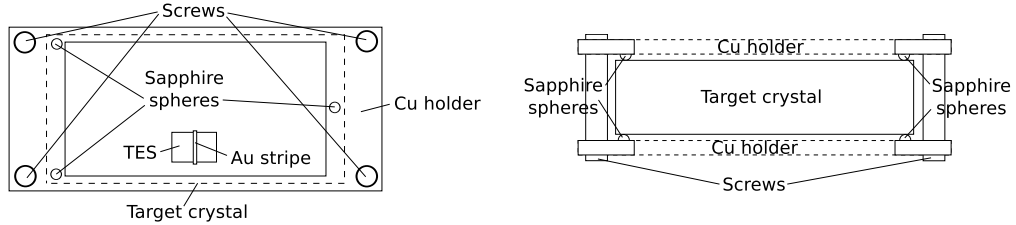


Figure 3.1: The left panel shows the top view and the right panel the cross section of the setup of the low-temperature detector used for the calibration and the background measurements. A $40 \times 20 \times 10 \text{ mm}^3$ sapphire crystal is mounted inside a copper holder using sapphire spheres to minimize the thermal coupling between target crystal and copper holder (see chapter 2). The iridium-gold TES is also shown. The TES is equipped with a gold stripe which provides a homogeneous thermal contact between TES and copper holder.

$40 \times 20 \times 10 \text{ mm}^3$ sapphire crystal, is mounted to a copper holder. Sapphire spheres are used for contacts to minimize the thermal coupling between the holder and the target crystal (see chapter 2). With the design of the copper holder shown in figure 3.1 a large area of the target crystal is not covered by the holder. Thus, the low-temperature detector can be calibrated with x-rays, gammas or light from almost any direction.

Figure 3.1 also shows the $6 \times 4 \text{ mm}^2$ TES evaporated onto the target crystal. This TES is equipped with a gold stripe for a homogeneous thermal contact between the TES and the copper holder.

3.1 Calibration measurement

The low-temperature detector was calibrated using a ^{55}Fe source mounted below the detector. Figure 3.2 shows the setup of this calibration measurement. The ^{55}Fe source is mounted in a copper housing with a small aperture. The copper housing allows an easy and safe handling of the ^{55}Fe source. Furthermore, the housing provides a good thermal contact between the source and the cryostat. Although the copper housing has a small aperture, the rate of x-ray photons leaving the housing is too high for a low-temperature detector. Thus, the rate was reduced by an additional aperture mounted between the copper housing of the ^{55}Fe source and the low-temperature detector.

^{55}Fe is decaying via electron capture (i.e., the capture of a K-shell electron) into the ground state of ^{55}Mn [58]. The vacancy in the K-shell is occupied by an electron of an outer shell. Thus, the characteristic x-ray radiation of ^{55}Mn is produced.

In table 3.1 the energies and intensities of the characteristic x-ray radi-

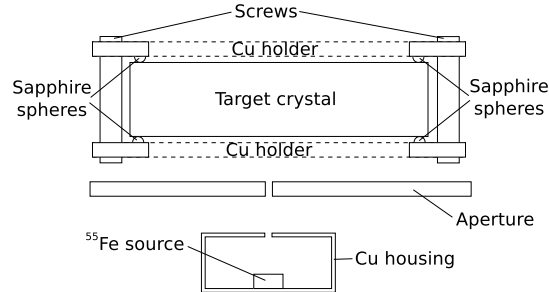


Figure 3.2: Setup for a calibration measurement using a ^{55}Fe source. The ^{55}Fe source is mounted in a copper housing with a small aperture. This housing is positioned below the target crystal. An additional aperture between the source and the detector is used to reduce the flux of ^{55}Mn x-rays onto the target crystal, since low-temperature detectors are too slow to cope with high count rates ($\gtrsim 50$ Hz).

Line	Energy [keV]	Intensity [%]
K_α	5.90	27.6
K_β	6.49	3.23
L_α	0.64	0.29
L_β	0.66	0.23
L_γ	0.56	0.06

Table 3.1: Energies and intensities for the characteristic x-ray radiation of ^{55}Mn [58]. The intensities given in the last column are the probabilities that a specific line is occurring. The probability for the production of x-ray radiation is $\sim 30\%$ and $\sim 70\%$ for the production of Auger electrons[58].

ation of ^{55}Mn are listed[58]. The most intense line is the K_α line which is ~ 9 times more intense than the K_β line. The intensities of the L lines are much smaller and thus they are not used for the calibration of the low-temperature detector developed for this work. In total $\sim 30\%$ of the K-shell vacancies of ^{55}Mn generate x-ray radiation. The rest of the K-shell vacancies ($\sim 70\%$) generate Auger electrons[58].

For the calibration of the low-temperature detector used in this work the position of the K_α and K_β lines were used. The left panel of figure 3.3 shows the pulse-height spectrum of the characteristic x-ray radiation of ^{55}Mn ¹. The larger peak corresponds to the K_α line and the smaller one to the K_β line of ^{55}Mn . To determine the positions of the two lines the sum $f(x)$ of two Gaussians (blue line in the left panel of figure 3.3) is fitted to the pulse-height

¹The methods used to obtain the spectrum shown in figure 3.3 are described in chapter 4.

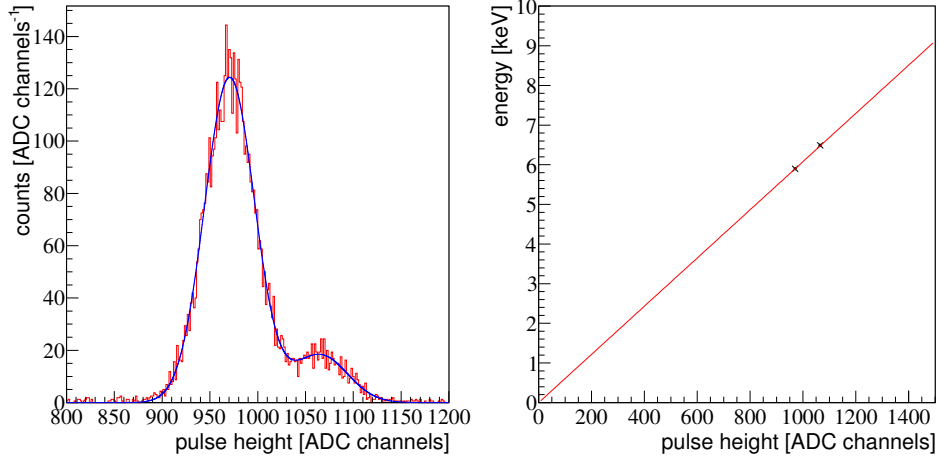


Figure 3.3: *Left panel:* Pulse-height spectrum of the K lines of the characteristic x-ray radiation of ^{55}Mn . The blue line represents a fit of the sum of two Gaussians to the spectrum (equation (3.1)).

Right panel: The red line represents the energy calibration of the low-temperature detector which is assumed to be linear for energies $\lesssim 10$ keV. The energy calibration was obtained by fitting equation (3.2) to the positions (black crosses) of the two K lines of ^{55}Mn .

spectrum:

$$f(x) = A_\alpha \left(\frac{1}{\sigma_\alpha \sqrt{2\pi}} e^{-\frac{(x-\mu_\alpha)^2}{2\sigma_\alpha^2}} + \frac{p}{\sigma_\beta \sqrt{2\pi}} e^{-\frac{(x-\mu_\beta)^2}{2\sigma_\beta^2}} \right), \quad (3.1)$$

where x is the pulse height in ADC channels, A_α is the number of events in the K_α peak, μ_α and μ_β are the positions of the K_α and K_β peak, σ_α and σ_β their widths, and p is the ratio of the intensities of K_β and K_α .

In table 3.2 the fitted parameters of equation (3.1) are listed. The value for p is larger than the expected value of ~ 0.12 . Thus, there are more K_β events than expected. This can be explained by a higher absorption coefficient for the K_α events inside the ^{55}Fe source[59].

The values of μ_α and μ_β are used for the calibration of the low-temperature detector since their corresponding energies are the energies of the K lines of ^{55}Mn (see table 3.1). It is assumed that the low-temperature detector is linear² for energies $\lesssim 10$ keV, i.e., the measured pulse height x of the detector signal is proportional to the deposited energy E :

$$E = a \cdot x, \quad (3.2)$$

²This assumption is always justified for small energy depositions (see chapter 2)

Parameter	Fitted value
A_α	$(8.159 \pm 0.125) \cdot 10^3$ counts
p	0.161 ± 0.009
μ_α	971 ± 0.47 ADC channels
μ_β	1065 ± 2.00 ADC channels
σ_α	26.18 ± 0.39 ADC channels
σ_β	28.68 ± 1.41 ADC channels

Table 3.2: Parameters for the fit of equation (3.1) to the uncalibrated spectrum (left panel of figure 3.3). The value for p is larger than the expected value of ~ 0.12 due to the higher absorption of K_α in the ^{55}Fe source[59].

where a is a scaling factor. The right panel of figure 3.3 shows the two calibration points, i.e., the K_α and the K_β line, as black crosses. Equation (3.2) was fitted to these pulse-height positions to obtain a value for the scaling factor a :

$$a = (6.080 \pm 0.003) \cdot 10^{-3} \frac{\text{keV}}{\text{ADC channel}}. \quad (3.3)$$

This value of the scaling factor a was used for the energy calibration of the low temperature detector built for this work. Figure 3.4 shows the calibrated

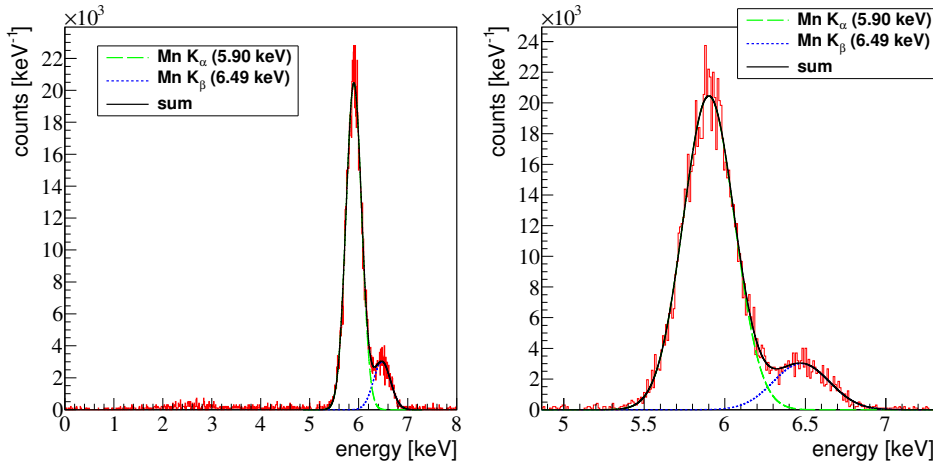


Figure 3.4: *Left panel:* Calibrated energy spectrum of the ^{55}Mn x-ray radiation. Equation (3.2) was used for the energy calibration. The energy resolution of the detector developed for this work is ~ 0.16 keV for the 5.9 keV K_α line. The resolution was determined by fitting equation (3.4) to the spectrum. The resulting function $f(E)$ as well as the contributions by the two K lines are also shown.

Right panel: Zoom into the K lines of ^{55}Mn .

spectrum of the ^{55}Mn x-ray radiation. To determine the energy resolution of

the detector the sum $f(E)$ of two Gaussians was fitted to the two peaks in the spectrum:

$$f(E) = A_\alpha \left(\frac{1}{\sigma_\alpha \sqrt{2\pi}} e^{-\frac{(E-\mu_\alpha)^2}{2\sigma_\alpha^2}} + \frac{p}{\sigma_\beta \sqrt{2\pi}} e^{-\frac{(E-\mu_\beta)^2}{2\sigma_\beta^2}} \right), \quad (3.4)$$

where E is the energy deposited in the target crystal of the detector. All other parameters of equation (3.4) have the same meaning as the parameters of equation (3.1).

Parameter	Fitted value
A_α	$(8.159 \pm 0.098) \cdot 10^4$ counts
p	0.161 ± 0.001
μ_α	5.9010 ± 0.0002 keV
μ_β	6.4751 ± 0.0009 keV
σ_α	0.1592 ± 0.0002 keV
σ_β	0.1744 ± 0.0007 keV

Table 3.3: Fitted parameters of equation (3.4) of the calibrated ^{55}Mn x-ray spectrum. The energy resolution of the used low-temperature detector is ~ 0.16 keV for the 5.9 keV K_α line of ^{55}Mn . The values for A_α and p are comparable to those of the fit for the uncalibrated spectrum (see table 3.2).

In table 3.3 the fitted parameters of equation (3.4) are listed. The values of A_α and p are comparable to those obtained by the fit of equation (3.1) to the uncalibrated spectrum (see table 3.2). The energy resolution of the low-temperature detector used for this work is ~ 0.16 keV for the 5.9 keV K_α line of ^{55}Mn .

The resolution of the detector used in this work is much worse than the resolutions of the detectors described in [19]. Since the target crystal and the dimensions of the TES are similar, this can only be explained by the poor properties of the phase transition of the TES of the detector used for this work (see chapter 2). The critical temperature of this TES is below the base temperature (~ 10 mK) of the cryostat. Thus, unfortunately, it was not possible to operate the detector in the steepest region of the phase transition of the TES.

Although the low-temperature detector employed for this work has a worse energy resolution and threshold than those detectors described in [19], it still can be used to study the low energetic background spectrum (see section 3.2).

3.2 Background spectrum for low energies

The ^{55}Fe source used for the energy calibration (see section 3.1) was removed for the measurement of the background spectrum. If the low-temperature detector was in the same working point³ for both the calibration and the background measurement, equation (3.2) can be used to calibrate the background spectrum. To test if the detector was in the same working point for both measurements, the pulse shapes obtained by both measurements have to be compared. Figure 3.5 shows the normalized pulse shapes obtained by

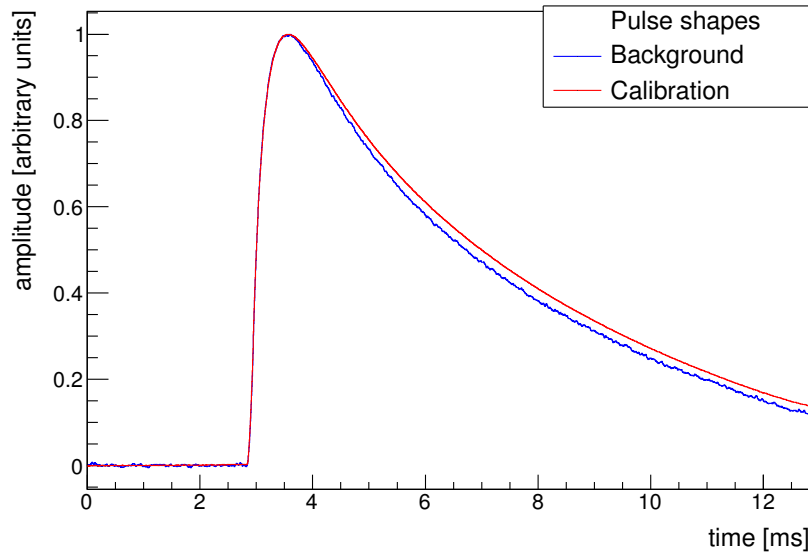


Figure 3.5: Normalized pulse shapes obtained by the calibration and background measurement. There is a small deviation between the two pulse shapes. Thus, equation (3.2) has to be modified for the calibration of the background spectrum. Since the detector behaves like a bolometer, the integrals of both pulse shapes can be used for this modification (see main text for further details).

the calibration and the background measurement. A deviation between both pulse shapes is clearly visible. However, since the deviation is small and the pulse shapes are comparable, equation (3.2) can be modified for the calibration of the background spectrum: the low-temperature detector used for the measurements discussed in this chapter behaves like a bolometer (see chapter 2). Thus, the integral of the pulse is proportional to the deposited energy. This can be used to modify equation (3.2).

³The working point is determined by the operation temperature of the TES and the bias current (see chapter 2).

Figure 3.5 shows normalized pulse shapes. Since the integral I_{back} of the pulse shape obtained from the background measurement is smaller than the integral I_{cal} of the pulse shape obtained by the calibration measurement, the same pulse height in both measurements corresponds to a slightly smaller energy deposition in the background measurement compared to the calibration measurement. Thus, equation (3.2) has to be modified by the ratio of the integrals of the two pulse shapes:

$$E = \frac{I_{cal}}{I_{back}} \cdot a \cdot x \quad (3.5)$$

$$\frac{I_{cal}}{I_{back}} = 0.95589, \quad (3.6)$$

where a is the scaling factor of equation (3.2) and x is the pulse height in ADC channels. Since the pulses in figure 3.5 are not recorded completely (for large times), there is a systematic error of $\sim 2\%$ on the energy calibration of the background spectrum.

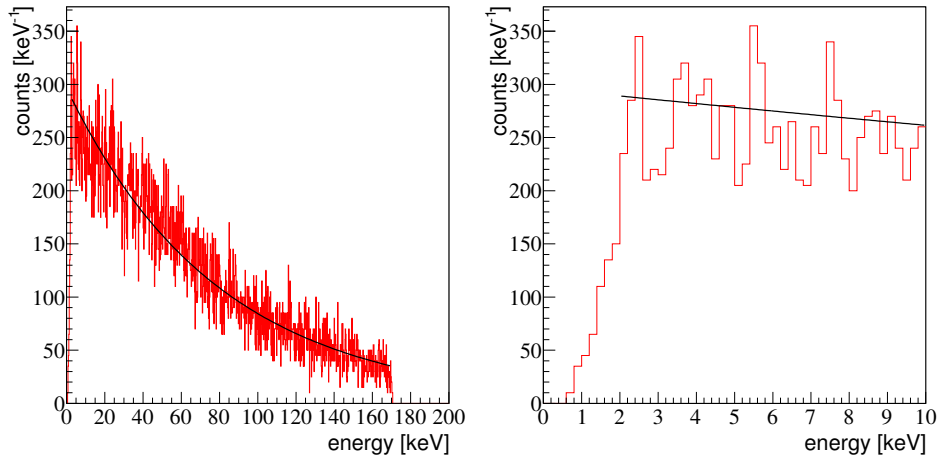


Figure 3.6: *Left panel:* Calibrated background spectrum measured with a sapphire-based low-temperature detector with a target mass of ~ 32 g. The background spectrum is a featureless and exponential spectrum. The total background rate was ~ 2.8 Hz. The black line represents the fit of an exponential to the spectrum. *Right panel:* Background spectrum for energies below 10 keV. The spectrum is approximately flat in this energy region. The drop below ~ 2 keV is due to a smaller cut efficiency for small pulse heights (see chapter 4). The rate below 4 keV was ~ 0.1 Hz. The black line represents the fit of an exponential to the complete background spectrum displayed in the left panel.

Deviations from the black line in both panels are due to the poor statistics caused by the short measuring time (~ 2 h).

Figure 3.6 shows the calibrated background spectrum. The left panel displays a featureless and exponential background spectrum for energies up to ~ 200 keV. Due to an electronics cut off⁴ only energies $\lesssim 200$ keV could be recorded properly. Since the detector was only calibrated with a ^{55}Fe source, it is not possible to test the linearity of the detector for energies $\gtrsim 10$ keV. The black line represents the fit of an exponential $a_0 e^{-E/a_1}$ to the background spectrum, where E is the deposited energy, $a_0 = 296.4 \pm 1.6$ and $a_1 = 79.6 \pm 0.5$ keV are fit parameters.

The right panel of figure 3.6 shows the background spectrum for energies below 10 keV. For low energies the background spectrum is approximately flat. The drop below ~ 2 keV is due to a smaller cut efficiency for small pulse heights. The cut efficiency, i.e., the fraction of accepted good events, has to be taken into account for the determination of the background rate and for the comparison of the background spectrum with the neutrino spectrum. The cut efficiency is determined in chapter 4.

Although the cut efficiency still has to be determined, the background rate can be calculated. Therefore, the live time, i.e., the time where the detector was actually able to record events, has to be calculated. The real time, i.e., the time difference of the last and the first recorded event, was ~ 2.19 h for the background measurement. During this time 76076 events were recorded⁵. However, 55706 events had to be rejected due to electronic noise and pile up⁶ (see chapter 4 for further details). For each event a time window of $4096 \cdot 3.125 \mu\text{s} = 12.8$ ms is recorded. Thus, all time windows of the rejected events have to be subtracted from the real time to obtain a live time of ~ 1.99 h. The detector was blind for $\sim 9.0\%$ of the time.

With 20380 events in a live time of ~ 1.99 h the total rate of background events below ~ 200 keV is 2.84 ± 0.02 Hz. The background rate in the energy region below 4 keV used for the observation of CNNS is 0.097 ± 0.004 Hz.

Assuming that the background rate below 4 keV is constant in time and the same for all low-temperature detectors used in the detector array described in chapter 2, the background rate for an experiment for the observation of CNNS would be $(2.63 \pm 0.10) \cdot 10^5$ background events per kg-day.

The actual background rate can be higher due to the cut efficiency (see section 4.4) and variations of the background rate, e.g., annual modulation of the muon flux[64, 65]. This modulation of the muon flux is $\mathcal{O}(1\%)$ and

⁴The SQUID output (see chapter 2) was recorded with a 16-bit ADC with a voltage range from -10 V to 10 V. Thus, the maximum pulse height is ~ 33000 ADC channels.

⁵All event numbers and rates in this section were obtained from integrals of the spectrum depicted in figure 3.6. The numbers and rates were not corrected for the cut efficiency discussed in section 4.4.

⁶i.e., two or more overlapping pulses

the rate at energies below 4 keV can be higher by a factor of ~ 2 due to the cut efficiency (see section 4.4). Thus, for a conservative estimation, the background rate can be higher by a factor of ~ 10 than the measured rate of $(2.63 \pm 0.10) \cdot 10^5$ background events per kg-day.

The allowed background rate for the observation of CNNS using reactor neutrinos is ~ 1000 background events per kg-day (see chapter 1). Thus, the observation of CNNS requires a good background suppression by a factor of $\sim 10^4$. In chapter 5 a dedicated shielding for background suppression is described.

Chapter 4

Data analysis: template fit and applied cuts

The output pulses of low-temperature detectors are relatively slow. The rise and decay times of the pulses are of $\mathcal{O}(\text{ms})$. The pulse height is used as a measure of the deposited energy (see chapters 2 and 3). Electronic and microphonic noise is present mainly at low frequencies[62, 66]. Due to the slow rise and decay times the output pulses are also at low frequencies ($\lesssim 20 \text{ kHz}$)[62, 66]. Thus, the determination of the pulse height of the output signals of low-temperature detectors suffers from electronic and microphonic noise. However, the shape of the pulses is different from that of electronic and microphonic noise and can thus be used for noise discrimination and the determination of the pulse height.

4.1 Determination of pulse parameters

The left panel of figure 4.1 shows a recorded pulse. Since the pulses are sampled discretely, all pulses are given as a sequence of N_r samples $P(i)$, where N_r is called the record length. The time base t_0 , i.e., the time difference between two consecutive samples, is determined by the read-out electronics. For the measurements discussed in this chapter and in chapter 3 the time base was $\sim 3 \mu\text{s}$.

If no pulse is present, the output voltage of the SQUID is almost constant. The small fluctuations around a constant mean value are caused by electronic and microphonic noise. This region of the recorded time window is called the base line. For the measurements in the present work the first 20% of the time window with a length of $\sim 13 \text{ ms}$ were used to fit a straight line to the base line. Thus, the baseline is characterised by a constant P_0 and a slope

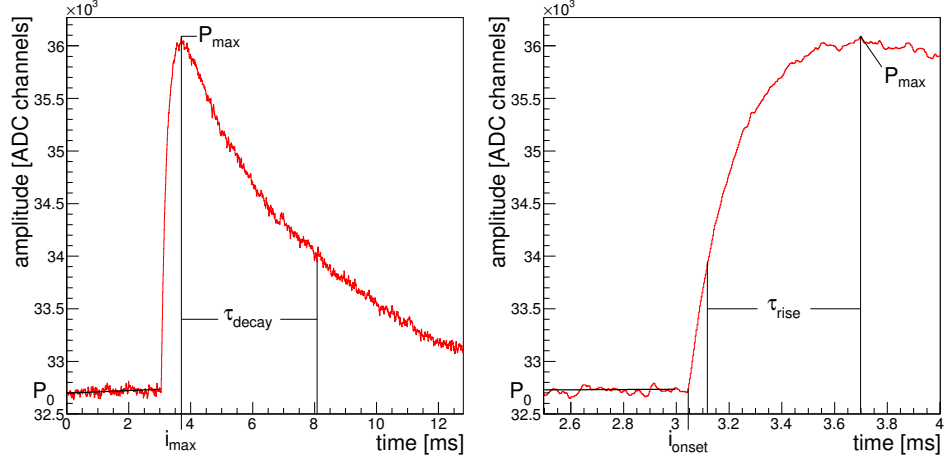


Figure 4.1: *Left panel:* A recorded pulse with all pulse parameters used for the data analysis described in this chapter.

Right panel: A zoom into the fast rise of the pulse.

The base line is fitted by a straight line ($f_{BL}(i) = P_0 + m_{BL} \cdot i \cdot t_0$). The maximum P_{max} (see equation (4.3)) of all samples $P(i)$ of the pulse is a rough estimate of the pulse height. The peak position i_{max} is the index of the maximum sample, i.e., $P(i_{max}) = P_0 + P_{max}$. The decay time τ_{decay} and the rise time τ_{rise} are associated with the shape of the pulse. The onset i_{onset} of the pulse is correlated with the trigger time. See main text for further details.

m_{BL} :

$$f_{BL}(i) = P_0 + m_{BL} \cdot i \cdot t_0. \quad (4.1)$$

The function f_{BL} , especially the slope m_{BL} , can be used to reject pulses with distorted shapes due to an inclined base line. However, f_{BL} can not be used to correct those distorted shapes. There are several processes leading to an inclined base line. In most cases a pulse with an inclined base line is recorded shortly after an event with a large energy deposition in the detector. For events with large energy depositions the recorded time window is too short to contain the complete pulse. So the base line of pulses following shortly after events with a large energy deposition is inclined due to the decay of the previous pulse also contained in the recorded time window. Thus, the base line of such events has to be described by the pulse model given in equation (2.8) in section 2.1. Also for the other processes like electronic or microphonic noise the base line can not be described by a linear equation.

Since pulses with inclined base lines can not be described uniformly, they have to be rejected using a cut on the fitted slope m_{BL} (see section 4.3.2). For accepted pulses, m_{BL} can be neglected and, thus, only the constant P_0 is used to determine the position of the base line.

The width σ_{BL} of the base line is given by

$$\sigma_{BL} = \sqrt{\frac{1}{N} \sum_{i=1}^{N_{BL}} (P(i) - f_{BL}(i))^2}, \quad (4.2)$$

where N_{BL} is the number of samples used for the determination of the base line, i.e., the first 20% of the recorded time window.

The most important parameter is the pulse height. A rough estimate¹ for the pulse height is given by P_{max} :

$$P_{max} = \max(P(i)) - P_0, \quad (4.3)$$

where $\max(P(i))$ is the maximum of all N_r recorded samples $P(i)$. Since P_{max} is given by the maximum of all samples, P_{max} is in most cases slightly larger than the actual pulse height.

The peak position i_{max} is the index of the maximum sample, i.e., $P_{max} = P(i_{max}) - P_0$. For large pulse heights the trigger threshold is reached earlier relative to the peak position than for small pulse heights. Since the time window recorded for each pulse is relative to the trigger time (i.e. the time when the sampled value is larger than the trigger threshold), the peak positions of larger pulses are shifted to larger times. Thus, the peak position i_{max} can be used to correct this trigger walk.

The decay time τ_{decay} is defined as the time difference between the peak position i_{max} , and the first sample $P(i)$ where

$$P(i) - P_0 < e^{-1} P_{max} \text{ with } i > i_{max}. \quad (4.4)$$

The right panel of figure 4.1 shows a zoom into the fast rise of the pulse. Similar to the decay time τ_{decay} the rise time τ_{rise} is given by the time difference between the peak position i_{max} and the last sample $P(i)$ where

$$P(i) - P_0 < e^{-1} P_{max} \text{ with } i < i_{max}. \quad (4.5)$$

Both the decay time τ_{decay} and the rise time τ_{rise} are associated with the shape of the recorded pulse. Thus, they can be used for a rough pulse shape discrimination.

The onset i_{onset} of the pulse is the last sample $P(i)$ where

$$P(i) - P_0 < 5\sigma_{BL} \text{ with } i < i_{max}. \quad (4.6)$$

The onset i_{onset} is correlated with the trigger time. Thus, the onset can be used to reject events where electric or microphonic noise triggered the read out system.

¹This estimate for the pulse height is a rather good approximation for pulses accepted by the cuts described in section 4.3.

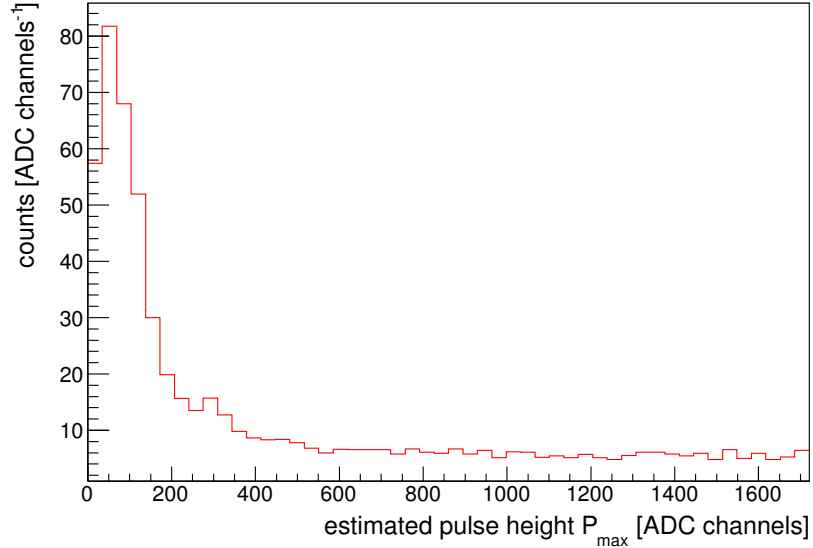


Figure 4.2: Raw-data spectrum of the estimated pulse height P_{max} for the background measurement. The peaks below ~ 400 ADC channels are due to electronic and microphonic noise. Those events have to be rejected in the data analysis described in this chapter to generate the background spectrum shown in figure 3.6.

Although P_{max} is only a rough estimate for the pulse height, it can still be used to generate the raw-data spectrum for the background measurement shown in figure 4.2 (see section 3.2). The peaks below ~ 400 ADC channels are due to poor events, i.e., events dominated by electronic and microphonic disturbances. These poor events have to be rejected to obtain the background spectrum shown in figure 3.6.

All parameters described in this section can be used for the rejection of such events. These rejection methods are described in the following sections. Also the efficiency of these rejection methods is estimated.

4.2 Template fit

A well known method for pulse-shape discrimination and the determination of the pulse height is the template fit[67]. For this method a template for the pulse shape is fitted to every recorded pulse to determine the pulse height. The goodness of this fit can be used for pulse-shape discrimination.

4.2.1 Generation of a template

The template-fit method is based on a pulse-shape template. This template is obtained by averaging N_t recorded pulses with a normalized height:

$$T(i) = \frac{1}{N_t} \sum_{j=1}^{N_t} \frac{P_j(i) - P_{0,j}}{P_{max,j}}, \quad (4.7)$$

where $T(i)$ is the i th sample of the template, $P_j(i)$ is the i th sample of the j th pulse, $P_{0,j}$ is the base line of the j th pulse, and $P_{max,j}$ is the estimated pulse height of the j th pulse (see equation (4.3)). The pulse height of the template is normalized to one. The pulse shapes shown in figure 3.5 (see section 3.2) are the templates obtained by the calibration and the background measurements.

Since the template $T(i)$ is correlated with both the base line P_0 and the estimated pulse height P_{max} of each pulse, the reliability of determination of these two pulse parameters is crucial for the quality of the template.

The reliability of the base line determination can be improved by increasing the time window and thus increasing the number of samples containing only the base line. However, this improvement also leads to an increase of the recorded amount of data. Furthermore, the probability for pile-up, i.e., to have two or more pulses in one time window, is increased. For the measurements presented in chapter 3 a record length of 4096 was used for the time window of each pulse. The first 20% of these time windows (corresponding to ~ 800 samples) were used for the determination of the base line (see figure 4.1).

The dependence of the template quality on the estimated pulse height P_{max} can be reduced by using pulses with similar pulse heights for the generation of the template. For the calibration measurement (see section 3.1) the pulses in the K_α -peak were used for the generation of the template shown in figure 3.5.

Obviously it is very important that all pulses used for the generation of the template have the same shape. This can be tested with both the rise times and the decay times of the pulses.

Furthermore, a time shift of the pulses used for averaging can deteriorate the quality of the template. This can be avoided by choosing pulses with similar peak positions i_{max} and onsets i_{onset} .

At last, it is also possible that the base line is not constant but exhibits a finite slope. Since the pulses generated by high energetic events like direct muon hits are longer than the recorded time windows, a pulse following shortly after such a high energetic pulse has a base line with a negative slope

due to the decreasing flank of the prior pulse. The slope m_{BL} of the straight line fitted to the base line can be used to reject such events.

4.2.2 Goodness of fit and χ^2 Minimization

The template obtained by equation (4.7) has to be fitted to each recorded pulse to determine its pulse height. To fit the template $T(i)$ to a recorded pulse $P(i)$ three free parameters are used. The template is scaled with an amplitude A which is a good estimation of the actual height of the pulse. The template has an offset B to correct for a poor determination of the base line of the pulse. And the template is also shifted in time to correct for the trigger walk. However, for simplification of the following equations this time shift t_s is not considered at first.

The likelihood $P(A, B|P)$ that a parameter set (A, B) is describing the recorded pulse P is given by[6]:

$$P(A, B|P) = \prod_{i=1}^{N_r} p(A, B, T(i)|P(i)), \quad (4.8)$$

where $p(A, B, T(i)|P(i))$ is the probability that the template sample $T(i)$ scaled by the amplitude A and shifted by the offset B is describing the recorded sample $P(i)$.

For equation (4.8) it was also assumed that all samples $P(i)$ are independent of each other. The accuracy of this assumption depends on the frequency distribution of the electronic and microphonic noise during the measurement. If this noise has a flat frequency spectrum (white noise) the samples are independent of each other. However, if for example low frequencies are dominating the frequency spectrum, it is more likely that the value of a sample $P(i)$ is near the value of its antecessor $P(i-1)$. Thus, the recorded samples $P(i)$ are not independent of each other and equation (4.8) can not be used for the calculation of the likelihood $P(A, B|P)$.

Figure 4.3 shows averaged Amplitude Spectral Densities (ASD) of both noise and signal. The ASDs were calculated following chapter 13 in [7] and the appendix of [66]. The ASD of electronic and microphonic noise was obtained from randomly recorded time windows containing only the flat base line. The ASD of the signal was obtained from the pulses used for the generation of the template.

The ASD of the noise is not flat. However, the intensity of lowest frequencies (~ 0.1 kHz) is only larger by a factor of ~ 5 than the intensity

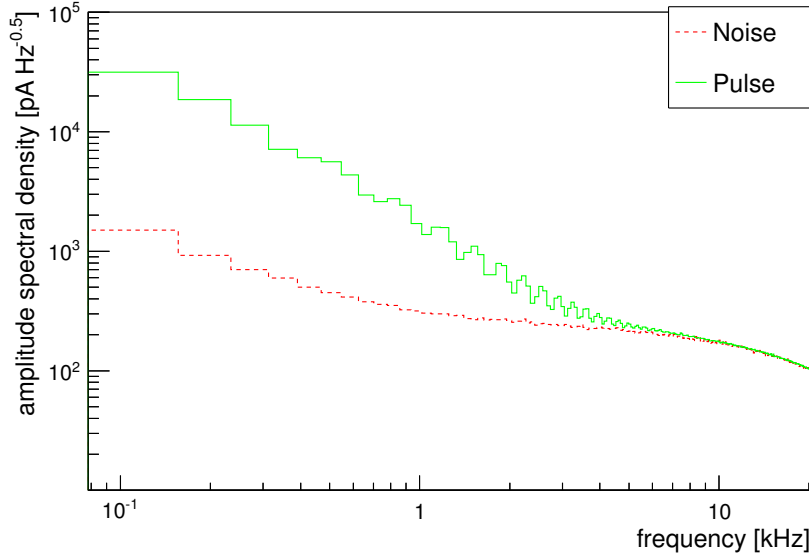


Figure 4.3: Amplitude spectral densities (chapter 13 in [7], appendix of [66]) of both noise (dotted red line) and signal (solid green line). The frequency spectrum of electronic and microphonic noise is not flat. However, since the intensity of the lowest frequencies of ~ 0.1 kHz is only a factor of ~ 5 larger than that of the highest frequencies present in the signal² (~ 10 kHz), it can be assumed that all recorded samples are independent of each other.

of the highest frequencies (~ 10 kHz) present in the signal². Thus, the recorded samples $P(i)$ can be assumed to be independent of each other and equation (4.8) can be used to calculate the likelihood $P(A, B|P)$.

The likelihood $P(A, B|P)$ has to be maximized to fit the template to a recorded pulse. For numerical reasons the logarithm of equation (4.8) is used to maximize the likelihood:

$$\ln P(A, B|P) = \sum_{i=1}^{N_r} \ln p(A, B, T(i)|P(i)), \quad (4.9)$$

If the samples $P(i)$ are normal distributed $p(A, B, T(i)|P(i))$ is given by:

$$p(A, B, T(i)|P(i)) = \frac{1}{\sqrt{2\pi\sigma_i^2}} e^{-\frac{(P(i)-AT(i)-B)^2}{2\sigma_i^2}}, \quad (4.10)$$

²For frequencies above ~ 10 kHz the ASDs of both noise and signal are the same. Thus, only frequencies below ~ 10 kHz are important for the template fit. In this frequency range the ASD of the noise is almost flat.

where σ_i are the uncertainties of the measured samples $P(i)$. This leads to

$$\ln P(A, B|P) = \sum_{i=1}^{N_r} \ln \frac{1}{\sqrt{2\pi\sigma_i^2}} - \sum_{i=1}^{N_r} \frac{(P(i) - AT(i) - B)^2}{2\sigma_i^2}. \quad (4.11)$$

In figure 4.4, a histogram of the values of $P(100)$ of all recorded pulses is

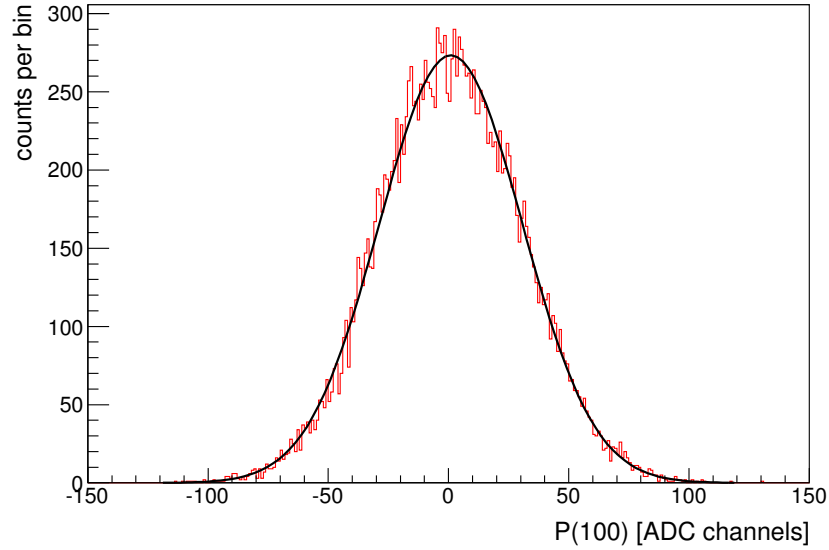


Figure 4.4: Histogram of the values of $P(100)$ (red line) of all recorded pulses (after rejection of poor pulses). A Gaussian (black line) is fitted to this histogram. Since the Gaussian describes the data very well, the recorded samples $P(i)$ can be assumed to be normal distributed.

displayed. Poor pulses were not taken into account for this histogram. A Gaussian, represented by the black line, was fitted to the histogram. The recorded samples $P(i)$ can be assumed to be normal distributed, since the Gaussian fits the data very well.

The first sum in equation (4.11) is independent of the amplitude A and the offset B . Thus, to maximize the likelihood $P(A, B|P)$ the second sum has to be minimized. To simplify equation (4.11) a new quantity, $\chi^2(A, B)$, is introduced³:

$$\chi^2(A, B) = \sum_{i=1}^{N_r} \frac{(P(i) - AT(i) - B)^2}{\sigma_i^2}. \quad (4.12)$$

$\chi^2(A, B)$ has to be minimized to maximize the likelihood $P(A, B|P)$. Both derivations $\frac{\partial \chi^2(A, B)}{\partial A}$ and $\frac{\partial \chi^2(A, B)}{\partial B}$ are vanishing at the minimum of $\chi^2(A, B)$.

³The derivation of the fitted values for the amplitude A and the offset B follows section 15.2 in [7].

Thus, the minimum of (A_{min}, B_{min}) of $\chi^2(A, B)$ is the solution of the following two coupled equations:

$$\frac{\partial \chi^2(A, B)}{\partial A} = -2 \sum_{i=1}^{N_r} \frac{T(i)(P(i) - AT(i) - B)}{\sigma_i^2} \stackrel{!}{=} 0 \quad (4.13)$$

$$\frac{\partial \chi^2(A, B)}{\partial B} = -2 \sum_{i=1}^{N_r} \frac{P(i) - AT(i) - B}{\sigma_i^2} \stackrel{!}{=} 0. \quad (4.14)$$

For convenience equations (4.13) and (4.14) can be rewritten as:

$$S_{PT} - AS_{TT} - BS_T = 0 \quad (4.15)$$

$$S_P - AS_T - BS = 0, \quad (4.16)$$

where

$$\begin{aligned} S &= \sum_{i=1}^{N_r} \frac{1}{\sigma_i^2} \\ S_P &= \sum_{i=1}^{N_r} \frac{P(i)}{\sigma_i^2} & S_T &= \sum_{i=1}^{N_r} \frac{T(i)}{\sigma_i^2} \\ S_{TT} &= \sum_{i=1}^{N_r} \frac{T(i)^2}{\sigma_i^2} & S_{PT} &= \sum_{i=1}^{N_r} \frac{P(i)T(i)}{\sigma_i^2}. \end{aligned} \quad (4.17)$$

The solution of the equations (4.15) and (4.16) is given by

$$A_{min} = \frac{SS_{PT} - S_P S_T}{\Delta} \quad (4.18)$$

$$B_{min} = \frac{S_{TT} S_P - S_P S_{PT}}{\Delta} \quad (4.19)$$

$$\Delta = SS_{TT} - (S_T)^2. \quad (4.20)$$

The errors of the amplitude A_{min} and the offset B_{min} are given by:

$$\sigma_A^2 = \frac{S}{\Delta} \quad (4.21)$$

$$\sigma_B^2 = \frac{S_{PP}}{\Delta}. \quad (4.22)$$

$\chi^2(A, B)$ (equation (4.12)) depends on the errors σ_i of all samples $P(i)$. It is assumed that those errors σ_i are the same for all samples. Thus, the values for the amplitude A_{min} and the offset B_{min} are independent of the error of all recorded samples, since the uncertainties σ_i are cancelled out.

However, the errors σ_A and σ_B and also $\chi^2(A, B)$ depend on the error of the recorded samples $P(i)$. Since this error is the same for all recorded samples, the width σ_{BL} is used as an estimation for the error of all recorded samples.

Up to now, the time shift t_s due to a trigger walk of the pulse was not taken into account. Since the pulses as well as the template are given as discrete samples, the time shift t_s is given in units of the time base t_0 . To account for the time shift equation (4.12) has to be modified:

$$\chi^2(A, B, t_s) = \sum_{i=\max(1, 1+t_s)}^{\min(N_r, N_r+t_s)} \frac{(P(i) - AT(i + t_s) - B)^2}{\sigma_i^2}. \quad (4.23)$$

Equation (4.23) can not be minimized analytically. It is, however, possible to minimize equation (4.23) for a fixed time shift by expanding the derivation above.

Since the time shift t_s is an integer in the interval $[-N_r, N_r]$, it is possible to calculate the minimum of $\chi^2(A, B)|_{t_s}$ for each time shift t_s with respect to the amplitude A and the offset B . The minimum of all $\chi^2(A, B)|_{t_s}$ is obtained for the optimal time shift $t_{s,min}$.

For a large amount of recorded pulses the calculation of all $\chi^2(A, B)|_{t_s}$ is very time consuming. Thus, it is convenient to apply a minimization algorithm (e.g., chapter 10 in [7]) to find the optimal time shift $t_{s,min}$. Such minimization algorithms are based on the approximation of a function $f(t_s)$ by a parabola near the minimum of the function. Since a parabola is determined by three points, it is possible to find a good estimate for the minimum of $\chi^2(A, B, t_s)$ with a few evaluations of $\chi^2(A, B)|_{t_s}$.

Figure 4.5 shows a template fitted to a recorded pulse. The fitted values are:

$$A_{min} = 3316.59 \pm 1.42 \text{ ADC channels} \quad (4.24)$$

$$B_{min} = 4.85 \pm 0.66 \text{ ADC channels} \quad (4.25)$$

$$t_{s,min} = -29 \cdot t_0 \quad (4.26)$$

$$\chi^2(A_{min}, B_{min}, t_{s,min}) = 1.236 \cdot 10^3, \quad (4.27)$$

where t_0 is the time base, i.e., the time difference between two successive samples $P(i)$ and $P(i+1)$. For the measurements described in chapter 3 the time base t_0 was $\sim 3 \mu\text{s}$. χ^2 is a measure for the goodness of the template fit. Its expected value is the Number of Degrees of Freedom (NDF)[7]:

$$NDF = N_r - |t_s| - 3, \quad (4.28)$$

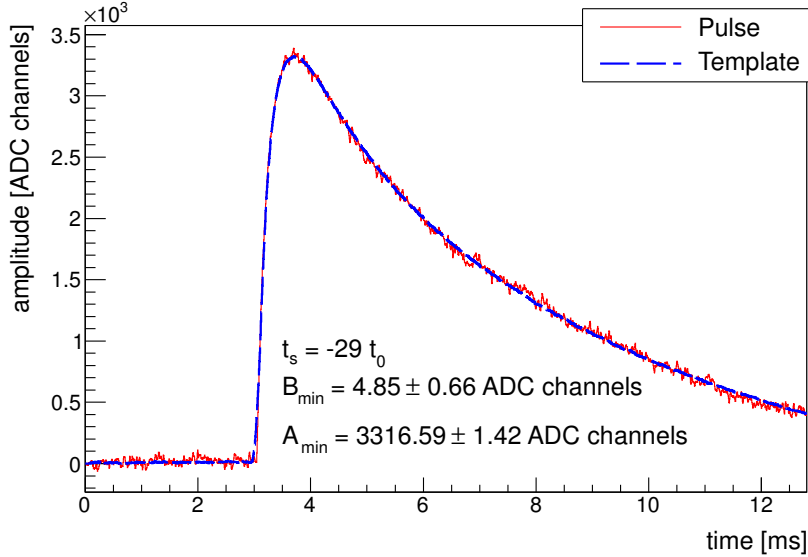


Figure 4.5: A template (blue dashed line) fitted to a pulse (red). The fitted values for the amplitude A_{min} , the offset B_{min} , and the time shift $t_{s,min}$ are also given. The reduced χ^2 (see main text) for this fit is ~ 0.30 indicating that the real errors of the recorded samples are smaller than σ_{BL} .

where $N_r - |t_s|$ is the number of samples used for the template fit and 3 is the number of parameters⁴. Since NDF depends on the time shift t_s , the reduced $\chi^2_{red} = \frac{\chi^2}{NDF}$ can be used to compare the χ^2 of the fits of the template to different pulses. The expected value for the reduced χ^2_{red} is one.

The reduced $\chi^2_{red} = 0.304$ of the fit shown in figure 4.5 is smaller than one. This indicates that the real errors of the recorded samples $P(i)$ of this pulse are smaller than the width σ_{BL} of the base line. However, the amplitude A_{min} , the offset B_{min} and also the time shift $t_{s,min}$ are independent of the errors of the recorded samples.

4.3 Rejection of poor events

Figure 4.6 shows the energy spectrum of all events recorded in the background measurement (see section 3.2). The fitted amplitude A_{min} (see equation (4.18)) of each pulse was calibrated using equations (3.2), (3.3), and (3.5). The resulting energy spectrum contains many poor pulses which have to be rejected to obtain the energy spectrum shown in figure 3.6. This section describes the cuts used to reject those poor events. The cuts are based

⁴Amplitude A , offset B , time shift t_s .

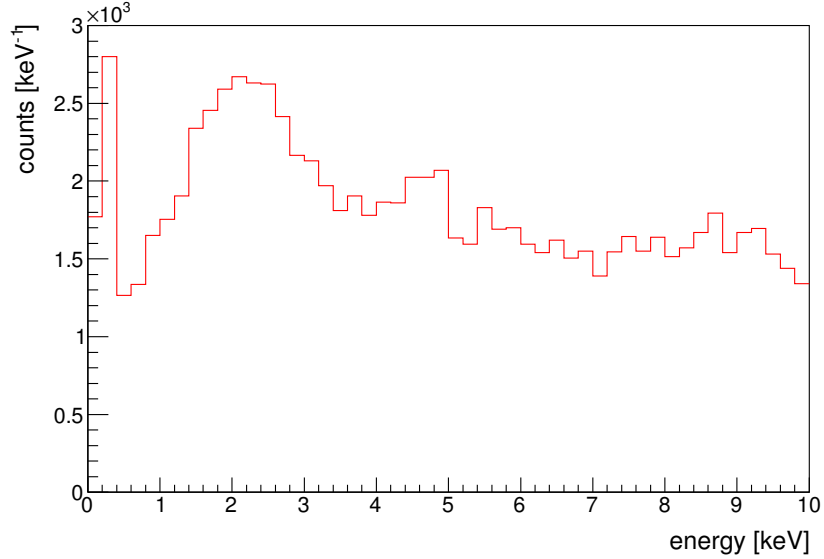


Figure 4.6: Energy spectrum of all events recorded in the background measurement (see section 3.2). The fitted amplitude A_{min} of each pulse was calibrated using equations (3.2), (3.3), and (3.5) to generate this spectrum. A lot of poor events are contained in this spectrum. These poor events have to be rejected to obtain the spectrum shown in figure 3.6.

on the pulse parameters described in section 4.1.

4.3.1 Cut on the base-line width σ_{BL}

The width σ_{BL} of the base line is proportional to the goodness of the fit of a straight line to the base line. Thus, it can be used to reject events with large electronic or microphonic disturbances. The left panel of figure 4.7 shows the spectrum of the base-line width σ_{BL} of all events. A large fraction of the recorded events have a width of ~ 30 ADC channels. Thus, only events with a base-line width between ~ 15 and ~ 45 ADC channels events were accepted, all other events were rejected. The lower threshold of ~ 15 ADC channels is needed to reject events where the read-out electronic was triggered by a SQUID failure.

The right panel of figure 4.7 depicts the energy spectra of all events before the cut on the base-line width and of the events accepted after this cut. If the readout electronics was triggered due to electronic or microphonic disturbances, the estimated pulse height P_{max} is small⁵. Thus, a large part

⁵For the present detector the pulse height P_{max} is comparable to the pulse height of events for deposited energies $\lesssim 10$ keV.

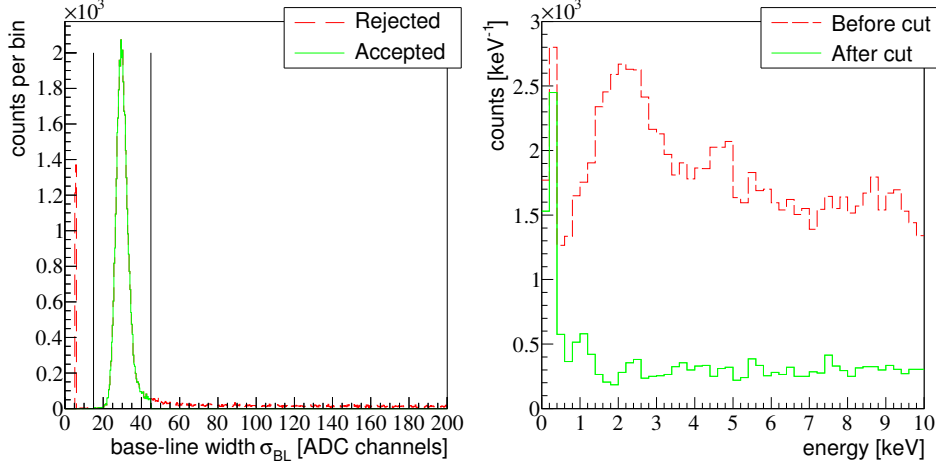


Figure 4.7: *Left panel:* Spectrum of the base-line width σ_{BL} . Only events with a width σ_{BL} between ~ 15 and ~ 45 ADC channels were accepted. All other events were rejected.

Right panel: The energy spectra of the events before and after the cut on the base-line width σ_{BL} . Since electronic and microphonic disturbances lead to events with a small estimated pulse height P_{max} , the cut on the base-line width σ_{BL} rejects a lot of low energetic ($\lesssim 10$ keV) events. The high energetic part ($\gtrsim 10$ keV) of the spectrum is neither shown in this nor in the following figures, since energies above ~ 10 keV are not important for the observation of CNNS.

of the events with a base-line width $\gtrsim 45$ ADC channels was assigned to small energies and so a large part of the low-energetic ($\lesssim 10$ keV) events is rejected by the cut on the base-line width σ_{BL} .

Only the low-energetic part ($\lesssim 10$ keV) of the spectrum is used for the observation of CNNS. Thus, in figure 4.7 and all following figures the spectra are shown for energies $\lesssim 10$ keV.

4.3.2 Cut on the base-line slope m_{BL}

For the generation of the template only pulses with a base-line slope m_{BL} (see equation (4.1)) near to 0 were used. Thus, the shape of pulses with a larger slope is distorted with respect to the template. Those pulses have to be rejected, since their fitted amplitude A_{min} is not proportional to the corresponding energy deposition.

The left panel of figure 4.8 depicts the spectrum of the base-line slopes m_{BL} of all pulses accepted by the cut on the base-line width σ_{BL} (see section 4.3.1). All events with a slope m_{BL} between ~ -40 and $\sim 40 \frac{\text{ADC channels}}{\text{ms}}$ are accepted by this fit, while all other events are rejected.

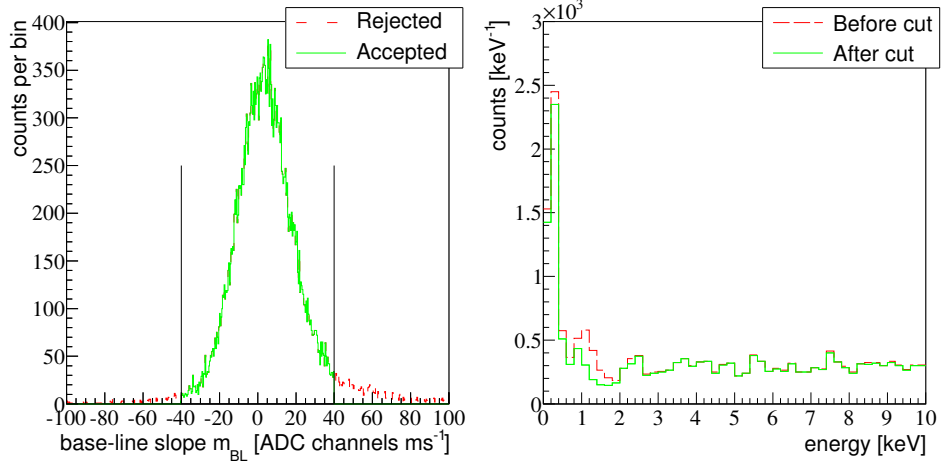


Figure 4.8: *Left panel:* Spectrum of the base-line slopes m_{BL} of all events accepted by the cut on the base-line width. All events with a slope between ~ -40 and $\sim 40 \frac{\text{ADC channels}}{\text{ms}}$ are accepted. All other events are rejected.

Right panel: Energy spectra of the events before and after the cut on the base-line slope m_{BL} . Since the main part of the rejected events is at high energies ($\gtrsim 10$ keV), the spectra shown here are only slightly affected by this cut.

The energy spectra before and after this cut on the base-line slope are shown in the right panel of figure 4.8. The main part of the events rejected by this cut is at high energies ($\gtrsim 10$ keV). Thus, the low-energy spectra shown in figure 4.8 are only slightly affected by this cut.

4.3.3 Cut on the goodness of the template fit

Up to now, only the base line of the recorded pulses was used to reject poor events. The results of the template fit (section 4.2) can be used for a further rejection of poor events. The reduced χ_{red}^2 is a measure for the goodness of the template fit.

The left panel of figure 4.9 shows $\log_{10}(\chi_{red}^2)$ of the template fit versus energy. The expected value of the reduced χ_{red}^2 is one for pulses with the same shape as the template. Thus, all events with $\log_{10}(\chi_{red}^2)$ near 0 are accepted while events with larger reduced χ_{red}^2 are rejected.

The right panel of figure 4.9 shows the spectra before and after the cut on the goodness of the template fit. Most low-energetic events with a distorted pulse shape also have a distorted base line. These events are already rejected with the cut on the base-line width σ_{BL} (section 4.3.1) and slope m_{BL} (section 4.3.2). Thus, the spectra shown in figure 4.9 are only slightly affected by this cut on the goodness of the template fit.

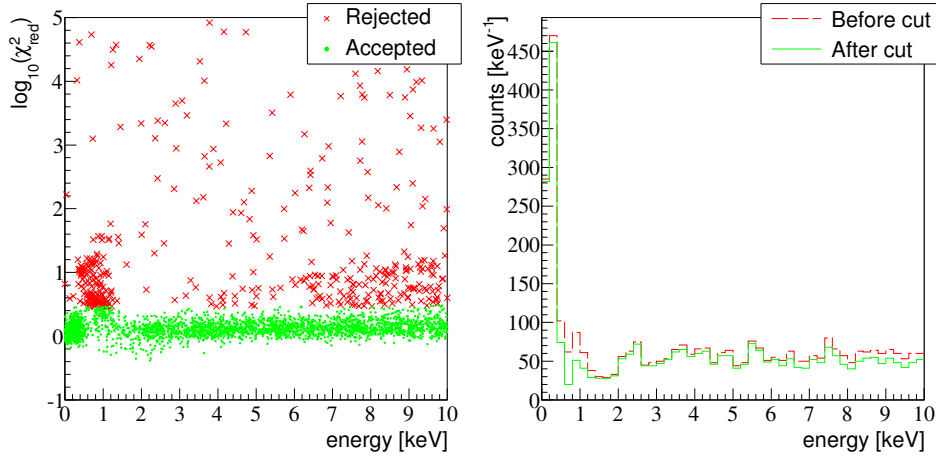


Figure 4.9: *Left panel:* $\log_{10}(\chi_{red}^2)$ of the template fit (see section 4.2.2) versus energy. The expected value for χ_{red}^2 is one. Thus, all events with $\log_{10}(\chi_{red}^2)$ near 0 are accepted, while events with larger χ_{red}^2 are rejected.

Right panel: The energy spectra before and after this cut on the goodness of the template fit. The main part of the rejected events are at high energies ($\gtrsim 10$ keV). Thus, the spectra for energies $\lesssim 10$ keV are only slightly affected by this cut.

4.3.4 Cut on peak position and onset channel

All events accepted by the previous cuts have a flat base line without electronic or microphonic disturbances. These events have also the same shape as the template.

However, if the readout electronics is triggered by electronic or microphonic noise, an event is recorded although no energy was deposited in the detector. Such events are also accepted by the previous cuts, if the amplitudes of the disturbances are small enough. The cuts on the base line width (section 4.3.1) and slope (section 4.3.2) are able to reject events where the complete recorded time window suffers from electronic and microphonic disturbances. However, events with one disturbance on a clean base line can not be rejected by cuts on the base line. Disturbances with small amplitudes can also be fitted very well with the template (see section 4.2). Thus, the cut on the goodness of the template fit (see section 4.3.3) is not able to reject disturbances with small amplitudes.

The peak position i_{max} and the onset i_{onset} of the remaining events can be used to distinguish between events caused by energy depositions in the detector and events triggered by electronic or microphonic noise.

Figure 4.10 shows the difference $D_{rise} = i_{max} - i_{onset}$ between the peak position with index i_{max} and the onset with index i_{onset} for randomly recorded

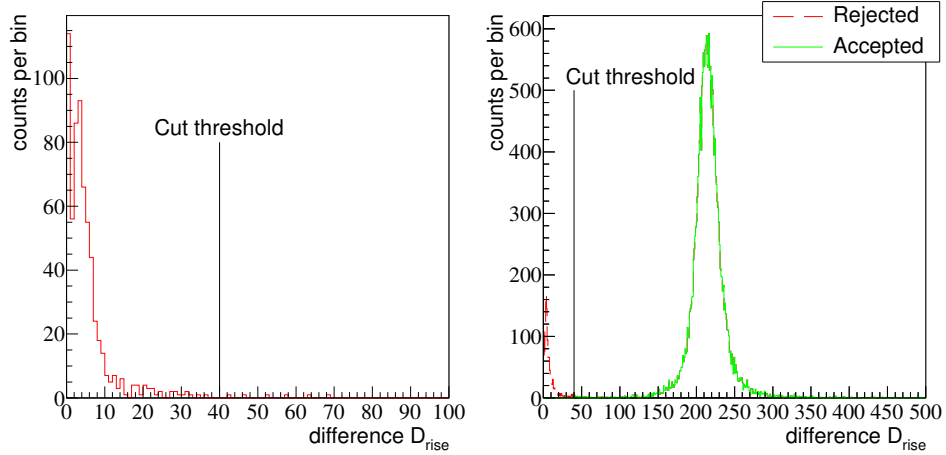


Figure 4.10: *Left panel:* The spectrum of the difference D_{rise} between peak position with index i_{max} and onset with index i_{onset} for randomly recorded time windows. Since these time windows are only containing a flat base line, this spectrum of $D_{rise} = i_{max} - i_{onset}$ can be used to determine the cut threshold ($D_{rise} = 40$). *Right panel:* The spectrum of D_{rise} for the events remaining after the previous cuts. The value for the cut threshold was determined by the spectrum of D_{rise} for a flat base line (left panel).

events (left panel) and for the events remaining after the previous cuts. For most events caused by an energy deposition the value of D_{rise} is correlated to the rise time of the pulses. Those events form the peak at $D_{rise} \approx 200$ in the right panel. However, for events caused by a very small energy deposition ($\lesssim 1$ keV) as well as for randomly recorded events the difference D_{rise} is small.

To determine the cut threshold for the difference D_{rise} its spectrum for the randomly recorded events shown in the left panel of figure 4.10 was used. Thus, all events with a difference D_{rise} below ~ 40 were rejected by this cut.

For events caused by an energy deposition in the detector the values of peak position i_{max} and onset i_{onset} are in the same small region due to the same pulse shape. Thus, a few events accepted by the cut on the difference D_{rise} have to be rejected due to their improper values for the peak position and the onset.

The left panel of figure 4.11 shows the $i_{max} - i_{onset}$ plane. The events with proper values for i_{max} and i_{onset} form a cluster (green dots) at a peak position of ~ 1100 and an onset of ~ 900 . The events outside of this cluster have a different pulse shape than the events inside the cluster (green dots). Thus, the events outside of the cluster have to be rejected after applying all cuts. For comparison also the events rejected by the cut on the difference

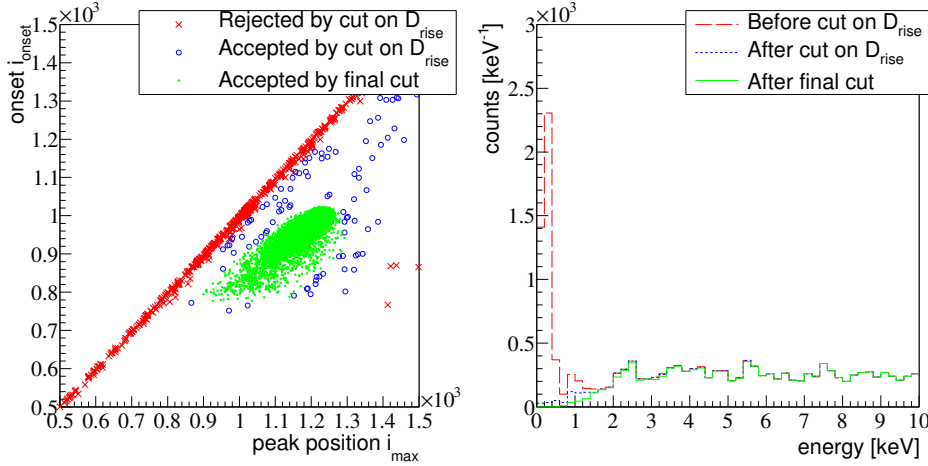


Figure 4.11: *Left panel:* Final cut on peak position i_{max} and onset i_{onset} . Only a few events (blue open circles), which were accepted by the cut on the difference D_{rise} , are rejected due to improper values for i_{max} and i_{onset} . For comparison also the events (red crosses) rejected by the cut on D_{rise} (see figure 4.10) are shown in this figure.

Right panel: Energy spectra before and after the cut on peak position i_{max} and onset i_{onset} (final cut). For comparison also the energy spectrum before the cut on the difference D_{rise} is shown. Both cuts are only rejecting events with small amplitudes.

D_{rise} (red crosses) are shown. The (blue) open circles denote events which are accepted by the cut on D_{rise} . The green dots represent the cluster of events accepted by the final cut on peak position and onset.

The right panel of figure 4.11 exhibits the energy spectra before and after the final cut on peak position and onset. For comparison also the energy spectrum before the cut on the difference D_{rise} is shown. Both cuts are mainly rejecting events with small amplitudes.

The spectrum after the cuts on the difference D_{rise} and on the peak position and onset is the final energy spectrum for the background measurement shown in figure 3.6 (see section 3.2).

4.4 Determination of the cut efficiency

The cuts described in section 4.3 were designed to reject all poor events and to accept as many good events⁶ as possible. Thus, the final background spectrum shown in figure 3.6 contains no poor events which are dominated

⁶Events caused by an energy deposition in the detector.

by electronic or microphonic disturbances.

However, especially at low energies a lot of good events were also rejected. It is crucial to know this fraction of rejected good events to compare the measured spectrum to the expected neutrino spectra described in chapter 1.

To determine the cut efficiency η_{cut} , i.e., the fraction of accepted good events, a data set containing pulses with different heights was generated in a simulation. The time base t_0 , the record length N_r , and the length N_{BL} of the base line were the same as for measured pulses. Each generated pulse sample $G(i)$ is a random number following the normal distribution $p_g(G(i))$:

$$p_g(G(i)) = \frac{1}{\sqrt{2\pi\sigma_{BL}^2}} e^{-\frac{(G(i)-A_g \cdot A_{temp}(i \cdot t_0))^2}{2\sigma_{BL}^2}}, \quad (4.29)$$

where $\sigma_{BL} = 30$ ADC channels is the mean width of the base line (see section 4.3.1 and figure 4.7), A_g is the height of the generated pulse, and

$$A_{temp}(i \cdot t_0) = \Theta(i \cdot t_0) \frac{1}{A_0} \left[A_n \left(e^{-\frac{i \cdot t_0}{\tau_n}} - e^{-\frac{i \cdot t_0}{\tau_{in}}} \right) + A_t \left(e^{-\frac{i \cdot t_0}{\tau_t}} - e^{-\frac{i \cdot t_0}{\tau_n}} \right) \right] \quad (4.30)$$

is the pulse model (see equation (2.8) in section 2.1) fitted to the template. The values used for A_n , A_t , τ_{in} , τ_n and τ_t are listed in table 2.1 (see section 2.1). The normalization constant A_0 is the maximum of

$$A_n \left(e^{-\frac{i \cdot t_0}{\tau_n}} - e^{-\frac{i \cdot t_0}{\tau_{in}}} \right) + A_t \left(e^{-\frac{i \cdot t_0}{\tau_t}} - e^{-\frac{i \cdot t_0}{\tau_n}} \right),$$

so that the height of $A_{temp}(i \cdot t_0)$ is normalized to one.

The generated data set contains pulses with different heights between 0 and 1000 ADC channels in steps of 10 ADC channels. For each height 2000 pulses were generated. All cuts described in section 4.3 were applied to the generated pulses. Figure 4.12 shows the cut efficiency η_{cut} for all generated pulse heights. The cut efficiency η_{cut} is given by the ratio of the number of accepted events $N_{acc}(A_g)$ and the number of generated events (2000) for each pulse height A_g . For the errors of the pulse height the bin width of 10 ADC channels was used. The errors of the cut efficiency η_{cut} were assumed to be 0.01. The values for the cut efficiency of the generated pulses were fitted by the empirical equation:

$$\eta(A_g) = \left(1 - \frac{1}{e^{\frac{A_g - a_0}{a_1}} + 1} \right) \left(1 - a_2 e^{-\frac{A_g}{a_3}} \right). \quad (4.31)$$

The first Fermi-distribution like term of equation (4.31) describes the steep drop of the cut efficiency at a fitted amplitude A_{min} of ~ 180 ADC channels.

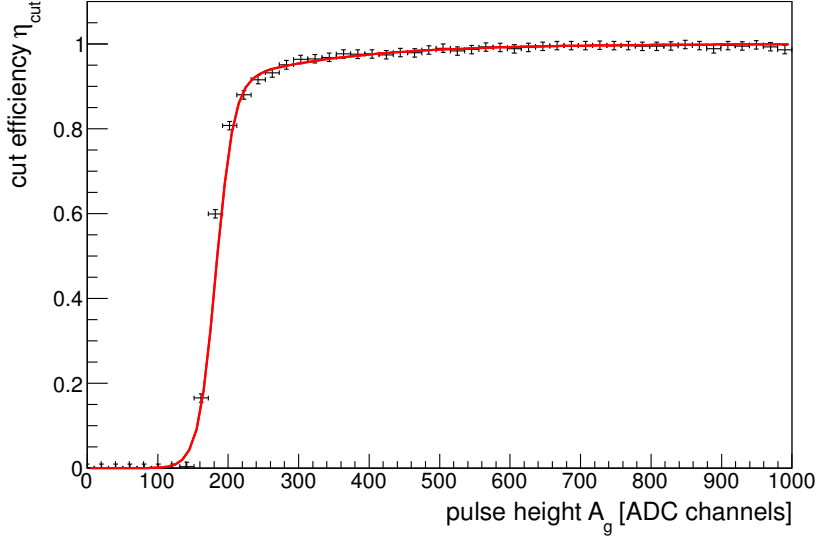


Figure 4.12: Cut efficiency η_{cut} for generated pulses with different heights. For each pulse height between 0 and 1000 ADC channels 2000 pulses were generated. The cut efficiency η_{cut} is the ratio between the number of accepted events $N_{acc}(A_g)$ and the number of generated events. The errors for the pulse height are the bin width (10 ADC channels). The errors for η_{cut} were assumed to be 0.01.

The second term accounts for the slow rise of the cut efficiency towards higher amplitudes A_{min} . The parameter a_0 is the position of the steep drop of the cut efficiency and is used as energy threshold of the detector, a_1 is the width of the step drop, a_2 is the amplitude and a_3 the slope of the slow rise of the cut efficiency at high amplitudes A_{min} .

The red line in figure 4.12 represents the fit of equation (4.31) to the values of η_{cut} for the generated pulses. The fitted values for the parameters

Parameter	Parameter
a_0	182.2 ± 5.6 ADC channels
a_1	12.58 ± 2.61 ADC channels
a_2	0.286 ± 0.134
a_3	163.9 ± 35.59 ADC channels

Table 4.1: Results of the fit of equation (4.31) to the values of η_{cut} for the generated pulses. The parameter a_0 is used as energy threshold of the detector. Equations (3.2), (3.3) and (3.5) (see chapter 3) were used to convert the fitted value of a_0 to an energy of $\sim 1.06 \pm 0.03$ keV.

a_i are listed in table 4.1. The energy threshold of the present low-temperature

detector is given by parameter a_0 . With equations (3.2), (3.3) and (3.5) of chapter 3 the energy threshold is found to be 1.06 ± 0.03 keV.

To compare the cut efficiency $\eta_{cut}(A_g)$ with the final background spectrum the pulse height A_g and the parameters a_i are converted into energy using again equations (3.2), (3.3) and (3.5). Figure 4.13 shows the final back-

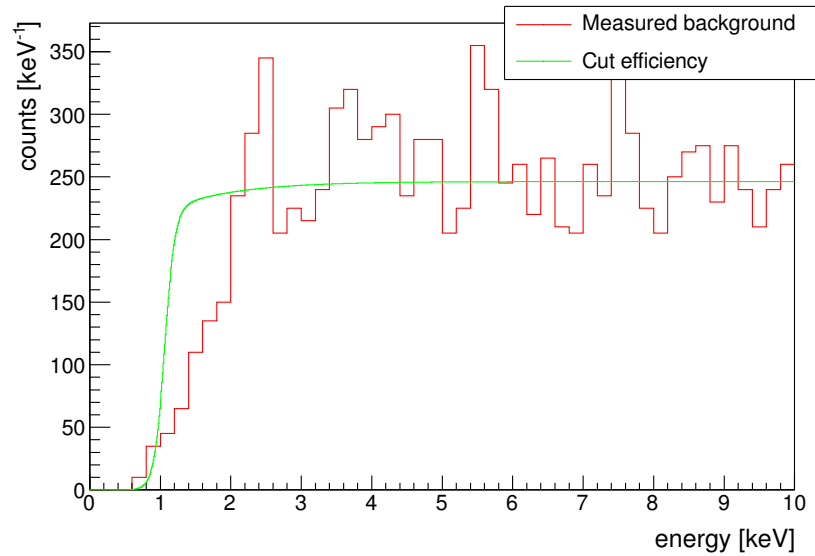


Figure 4.13: Comparison of the cut efficiency $\eta_{cut}(E)$ and the final background spectrum. For the energy calibration of $\eta_{cut}(E)$ equations (3.2), (3.3) and (3.5) of chapter 3 were used. Furthermore, $\eta_{cut}(E)$ was scaled to the integral of the background spectrum (number of background events below 10 keV). For energies between 1 and 2 keV more events are rejected than predicted by $\eta_{cut}(E)$ (see main text).

ground spectrum and the calibrated cut efficiency $\eta_{cut}(E)$. The cut efficiency was scaled so that the integrals of both the background spectrum shown in figure 4.13 and the cut efficiency curve are equal to the number of background events below 10 keV.

In the energy region between 1 and 2 keV more events ($\mathcal{O}(10)$) are rejected than predicted by the cut efficiency. This can be explained by the different noise distributions of the measured and generated data. All samples $G(i)$ of a generated pulse are independent of each other and the distribution $p_g(G(i))$ (see equation 4.29) is symmetric with respect to the mean values $A_g \cdot A_{temp}(i \cdot t_0)$. If, for example, the value of the sample $G(i)$ is larger than its mean value, the probability that $G(i+1)$ is also larger than the mean is equal to the probability that $G(i+1)$ is smaller than the mean value. Thus, the frequencies are equally distributed leading to a flat noise distribution for the

generated data. However, for the measured data the spectral density for low frequencies is slightly higher than that for high frequencies (compare figure 4.3) due to electric and microphonic noise. Thus, especially at low energies ($\lesssim 2$ keV) the distributions of all pulse parameters used for the cuts described in section 4.3 are broader than the corresponding distributions of the generated data. This leads to a larger fraction of rejected events of the measured spectrum especially at low energies.

Most of the cuts described in section 4.3 are robust against changes of the thresholds used for this cuts. Only a change of the threshold of the cut on the difference D_{rise} (see section 4.3.4 and figure 4.10) affects the final background spectrum shown in figure 4.13. However, the threshold for this cut is well motivated by randomly recorded time windows depicted in the left panel of figure 4.10.

The low-temperature detector used for the present work has an energy threshold of ~ 1 keV which is too large for the observation of CNNS (see chapter 1). The energy threshold as well as the energy resolution of this detector suffers from low-frequency noise as well as a small fraction of non-thermal phonons contributing to the pulses (see figure 2.3 in section 2.1). The collection efficiency of non-thermal phonons can be improved by the use of phonon-collectors (see section 2.1). Since a large part of the low-frequency noise is due to microphonics, it is possible to reduce the low-frequency noise by improving the mounting of both the low-temperature detector and the cryostat used to provide the low temperatures.

A large fraction of events with low energies ($\lesssim 10$ keV) are rejected due to their base-line width σ_{BL} (see section 4.3.1). This can be explained by a large number of pulses suffering from electronic disturbances. Thus, to reduce the number of rejected events the electric connections between the detector and the read-out electronics as well as the electric shielding have to be improved.

Concerning the simulations, the measured noise distribution (see figure 4.3) has to be taken into account for the generation of a data set used for the determination of the cut efficiency. Such a data-set can also be used to study the distributions of the pulse parameters used by the cuts described in section 4.3. In this way, the optimal thresholds for these cuts can be determined, so that all poor pulses are rejected and as many good pulses as possible are accepted.

However, for the generation of such a data set taking into account the measured noise distribution a large number of recorded time windows containing only the empty base line is needed. Thus, due to the small measurement time (~ 2 h) for the background spectrum it was not possible to generate such a data set.

Chapter 5

Background investigations for a future CNNS experiment

In chapter 3 the background spectrum measured by a sapphire-based low-temperature detector is described. To study the origin of this spectrum and also to study the background suppression of a future experiment for the observation of CNNS several simulations were performed. These simulations are based on the Geant4 simulation toolkit[68] and are presented in this chapter.

5.1 Simulation of the background measurement

In section 3.2 the measurement of the background spectrum using a low-temperature detector is described. This background spectrum is used as an estimate for the expected background for the observation of CNNS. As has been pointed out in section 3.2 this background spectrum has to be suppressed by a factor of $\sim 10^4$ to observe CNNS during a one-year measurement at a reactor site (see also section 1.2.2). The composition of the different background sources is crucial to study the suppression of the expected background.

In the present chapter the origin of the background spectrum shown in figure 3.6 is studied by the comparison of the measured spectrum to simulated spectra of different possible background sources. These simulations are based on the simulations performed in [59]. The setup of the cryostat shown in figure 5.1 was also adopted from [59]. The low-temperature detector used for the measurement of the background spectrum is operated at mK temperatures. These low temperatures are provided by a dilution cryostat. Only

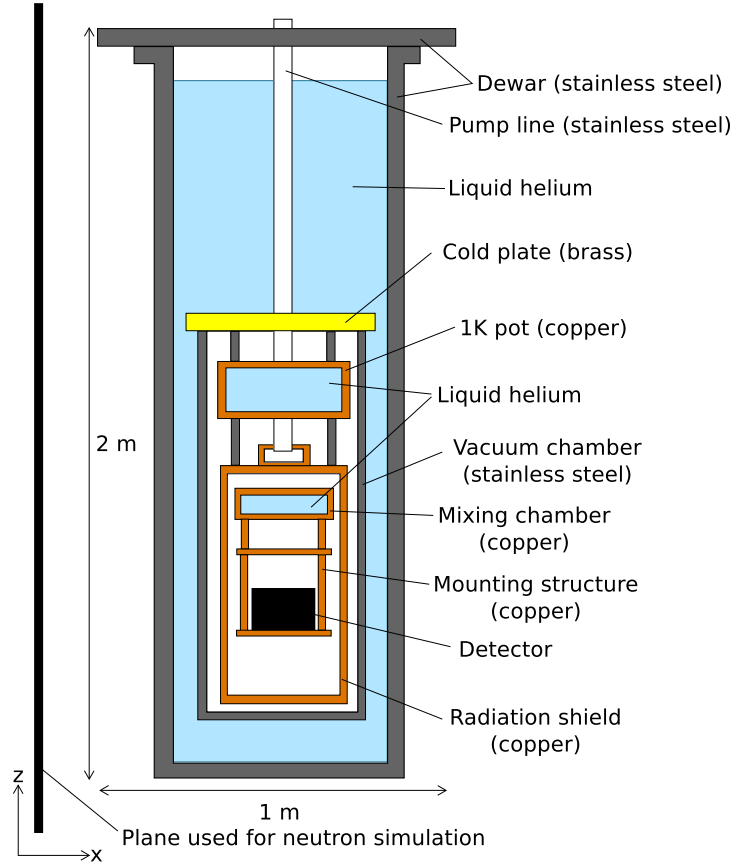


Figure 5.1: Setup of the simulations of the background measurement. To obtain the low temperatures needed for the operation of the detector used for the measurement of the background spectrum (see chapter 3) a dilution cryostat was used. The large and heavy parts of this cryostat are implemented in the simulation[59]. The setup of the detector is shown in figure 3.1 in chapter 3.

the large and heavy parts of this cryostat are implemented in the simulation. The setup of the detector shown in figure 3.1 of chapter 3 has also been implemented.

5.1.1 Muon background

Muons are produced by cosmic rays interacting with the earth's atmosphere. Their energy spectrum follows the energy spectrum of cosmic rays[6]. For the simulation of the muon background the energy spectrum of cosmic muons was approximated by:

$$\frac{dN_\mu}{dE_\mu} \propto E_\mu^{-2.7}, \quad (5.1)$$

where N_μ is the number of muons and E_μ is the muon energy.

The angular distribution of cosmic muons is approximately proportional to $\cos^2(\theta)$ [6], where θ is the polar angle of the incoming muon. Furthermore, a dedicated algorithm to generate random starting points and momenta of the muons was additionally implemented[59]. Due to this algorithm only muons which are directed towards the detector are simulated leading to a further reduction of computation time.

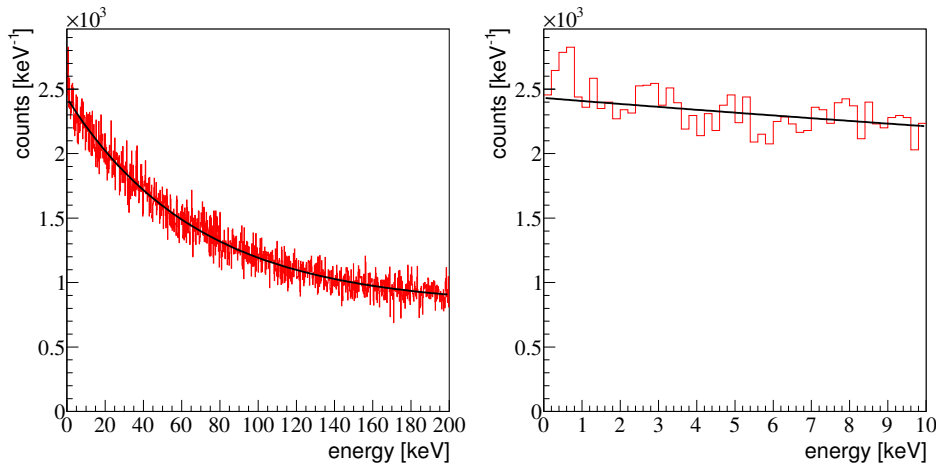


Figure 5.2: *Left panel:* Simulated energy spectrum of the muon contribution to the measured background spectrum (see section 3.2 and figure 3.6). For this energy spectrum the tracks of 10^8 muons and their secondary particles were simulated. The black line in both panels represents the fit of the function $a_0 e^{-E/a_1} + a_2$ to the simulated spectrum. The decay constant $a_1 = 68.3 \pm 0.6$ keV is comparable to the decay constant of the measured spectrum (see section 3.2). However, since the measured spectrum is only calibrated below ~ 10 keV, the constant offset a_2 can not be compared to the measured spectrum.

Right panel: For low energies ($\lesssim 10$ keV) the shape of the simulated spectrum is comparable to the measured spectrum (see section 3.2 and figure 3.6).

Figure 5.2 shows the resulting energy spectrum of the simulation of 10^8 muons and their secondary particles. The left panel shows the simulated spectrum up to an energy of 200 keV. The black line represents the fit of the function $a_0 e^{-E/a_1} + a_2$ to the simulated spectrum. The decay constant $a_1 = 68.3 \pm 0.6$ keV is comparable to the decay constant of the measured spectrum ($a_1 = 79.6 \pm 0.5$ keV, see section 3.2 and figure 3.6). The parameters $a_0 = 1612 \pm 5$ and $a_2 = 820 \pm 4$ depend on the number of simulated muons. The constant offset a_2 describes the difference between the measured and the simulated spectra for energies $\gtrsim 50$ keV. However, since the measured spectrum is only calibrated for energies $\lesssim 10$ keV, the energy calibration using

equations (3.2), (3.3) and (3.5) can not be applied for energies $\gtrsim 10$ keV. Thus, both spectra can only be compared at low energies ($\lesssim 10$ keV). Nevertheless, the shape of a spectrum decaying towards high energies can well be reproduced by the simulation of cosmic muons.

For a detailed discussion of the spectra for energies $\gtrsim 10$ keV one of the methods described in section 2.4 can be used for an energy calibration for energies above ~ 10 keV. However, since the expected recoil energies of reactor neutrinos are small ($\lesssim 4$ keV), the high-energetic parts of both the simulated and the measured spectra are not important for a future experiment aimed at the observation of CNNS.

The right panel of figure 5.2 depicts a zoom into the low-energetic part of the simulated spectrum. For these low energies ($\lesssim 10$ keV) the spectrum is almost flat and very similar to the measured spectrum. For the comparison of the simulated and the measured spectra the simulated spectrum has to be convoluted with a Gaussian describing the energy resolution of $\sim 2.7\%$ (see section 3.1 and table 3.3). The cut efficiency $\eta_{cut}(E)$ (see section 4.4 and equation (4.31)) has also to be taken into account.

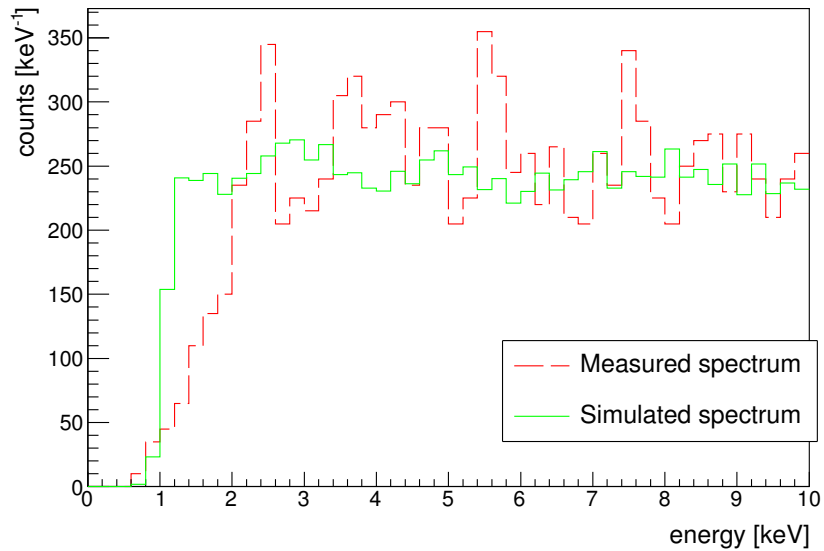


Figure 5.3: Comparison of the energy spectrum obtained by the simulation of 10^8 muons (solid green line) and the measured background spectrum (dashed red line). Both spectra are in good agreement above ~ 2 keV. The discrepancies below ~ 2 keV are due to the differences between the cut efficiency and the measured background spectrum (see section 4.4 and figure 4.13).

Figure 5.3 shows both the measured and the simulated spectrum which are in good agreement above an energy of ~ 2 keV. Below ~ 2 keV the sim-

ulated spectrum follows the steep drop of the cut efficiency (see section 4.4 and figure 4.13). Since the cut efficiency underestimates the number of rejected events below ~ 2 keV, the simulated spectrum also exhibits more events below ~ 2 keV than the measured spectrum. Nonetheless, cosmogenic muons are most likely the origin of the measured background spectrum.

5.1.2 Neutron background

Another possible background source are ambient neutrons. These neutrons are produced by cosmogenic muons in the vicinity of the experiment, e.g., in the walls or the ceiling of the laboratory. The energy spectrum of these ambient neutrons can be approximated by[69]:

$$\frac{dN}{dE_n} \propto \frac{e^{-7E_n}}{E_n} + B(E_\mu)e^{-2E_n} \quad (5.2)$$

$$B(E_\mu) = 0.52 - 0.58e^{-0.0099E_\mu}, \quad (5.3)$$

where E_n is the neutron energy and $E_\mu \approx 10.3$ GeV[69] is the mean energy for muons in a depth of ~ 20 m water equivalent.

Since the majority of the ambient neutrons are produced in the walls surrounding the cryostat, the starting points of the $2 \cdot 10^8$ simulated neutrons were randomly chosen on the 2.7×2.7 m² plane shown in figure 5.1. All simulated neutrons were directed parallel to the x-axis (see figure 5.1) towards the inside of the cryostat and the detector. According to these start conditions a large part of the simulated neutrons are entering the detector only due to scattering off the materials surrounding the detector (see figure 5.1).

Figure 5.4 depicts the energy spectrum obtained by the simulation of $2 \cdot 10^8$ ambient neutrons and their secondary particles. The left panel exhibits the spectrum up to ~ 200 keV, while the right panel shows a zoom into the low-energetic part (below ~ 10 keV) of the simulated energy spectrum. The spectrum generated by ambient neutrons is, unlike the measured background spectrum, very steep. The comparison¹ of the simulated and the measured spectra shown in figure 5.5 emphasizes the disagreement between both spectra. Thus, it is unlikely that ambient neutrons produced by cosmogenic muons are the main contribution to the measured background spectrum.

¹For this comparison, the simulated spectrum was convoluted by a Gaussian describing the energy resolution of $\sim 2.7\%$ (see section 3.1 and table 3.3). The resulting spectrum was then multiplied by the cut efficiency $\eta(E)$ (see section 4.4 and equation 4.31).

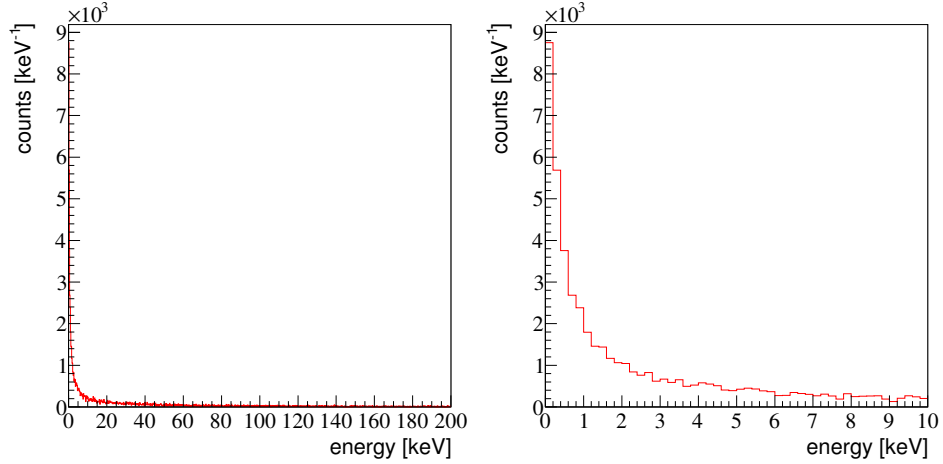


Figure 5.4: *Left panel:* Simulated energy spectrum obtained by the simulation of $2 \cdot 10^8$ neutrons and their secondary particles.

Right panel: Zoom into the low-energetic part ($\lesssim 10$ keV) of the simulated spectrum.

5.1.3 Gamma background

Also gammas produced by natural radioactivity can contribute to the measured background spectrum. However, since low-energetic gammas are absorbed or scattered in the material surrounding the detector (see figure 5.1), a simulation was performed to estimate the probability that a gamma produced outside of the cryostat deposits energy in the detector. This simulated probability is depicted in the left panel of figure 5.6 for different incident gamma energies up to ~ 2.5 MeV. For each gamma energy 10^7 gammas and their secondary particles were simulated. The starting points of the simulated gammas are uniformly distributed over a cylindrical surface outside of the cryostat. The incident momentum direction was chosen to point to the detector. For low incident energies ($\lesssim 0.2$ MeV) the gammas are absorbed in the different walls of the cryostat (see figure 5.1) leading to a small probability for an energy deposition. Gammas with energies of ~ 0.5 MeV have the highest probability to deposit energy in the detector crystal. However, due to Compton scattering in the different walls of the cryostat this probability is still $\lesssim 40\%$. For higher gamma energies ($\gtrsim 0.5$ MeV) the probability for an energy deposition is decreasing due to a higher probability for Compton scattering for such high gamma energies.

The right panel of figure 5.6 exhibits the probability that a gamma deposits less than 10 keV in the detector crystal. This probability is highest for gammas with an incident energy of ~ 0.2 MeV. Thus, gammas with such en-

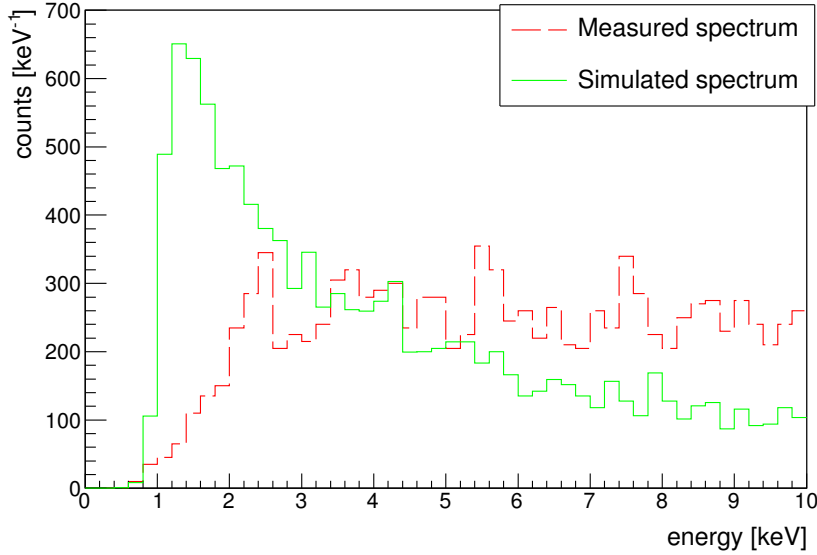


Figure 5.5: Comparison of the simulated energy spectrum obtained by the simulation of $2 \cdot 10^8$ ambient neutrons and the measured background spectrum (see section 3.2 and figure 3.6). Due to the steep decay of the simulated spectrum it is unlikely that the measured background has its origin in ambient neutrons produced by cosmic muons.

energies could be a background source for the observation of CNNS, although, due to their small energies, the majority of those gammas is absorbed in the walls of the cryostat or a dedicated shielding (see section 5.1 and figure 5.8 below).

The left panel of figure 5.7 shows as an example the energy spectrum obtained by the simulation of gammas with an incident energy of 0.2 MeV. This simulated spectrum was scaled so that the integrals below 10 keV are the same for both the simulated and the measured background spectrum (see section 3.2 and figure 3.6). The shape of the simulated spectrum is dominated by the Compton effect. The Compton edge of 0.2 MeV gammas is clearly visible at ~ 88 keV. Also the photo peak, i.e., deposition of the complete incident gamma energy, at 200 keV is visible. The structure between 100 and 140 keV is due to multiple Compton scattering.

The right panel of figure 5.7 exhibits a zoom into the energy region below ~ 10 keV. In this region both the simulated gamma spectrum and the measured background spectrum (see section 3.2 and figure 3.6) are in good agreement. The disagreement below ~ 2 keV is due to the cut efficiency (see section 4.4). However, for energies above ~ 10 keV (see left panel of figure 5.7) both spectra are in strong disagreement. In section 5.1.1 is mentioned

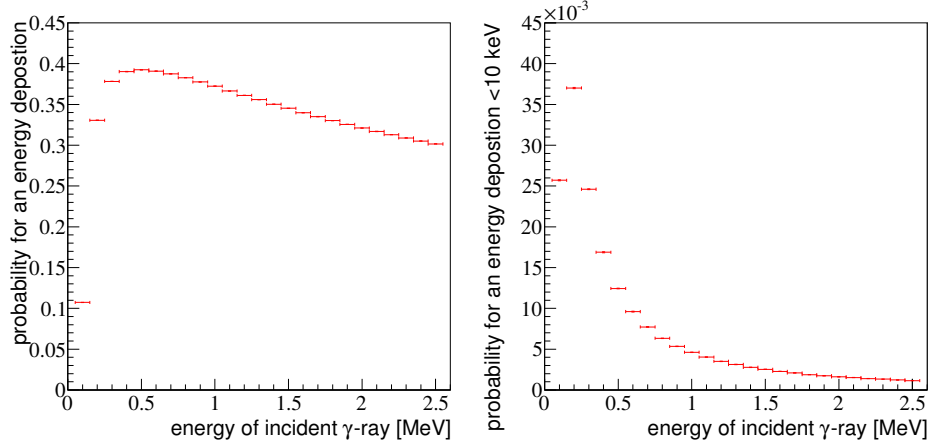


Figure 5.6: *Left panel:* Simulated probability for an energy deposition (including the range from 0 to 10 keV) by gammas produced outside of the cryostat (see figure 5.1). This probability was simulated for different gamma energies up to ~ 2.5 MeV. For small energies ($\lesssim 0.5$ MeV) most of the gammas are absorbed in the different walls of the cryostat. For energies $\gtrsim 0.5$ MeV the probability for an energy deposition is decreasing due to a higher probability for Compton scattering. *Right panel:* Simulated probability for an energy deposition below 10 keV in the detector. Gammas with energies of ~ 0.2 MeV have the highest probability ($\sim 3.7\%$) to deposit less than ~ 10 keV in the detector crystal.

that the measured spectrum is not calibrated for energies above ~ 10 keV. Thus, small deviations between measured and simulated spectra, e.g., the additional constant a_2 which is needed to describe the simulated muon spectrum, can be explained by the non-linearity of the detector and the missing calibration for energies above ~ 10 keV. However, while the measured spectrum follows an exponential decay, the simulated gamma-spectrum is constant and even rising towards the Compton edge of ~ 88 keV. This large disagreement between the measured and the simulated spectrum can not be explained by non-linearity of the detector or a missing calibration. Thus, gammas generated by natural radioactivity are a minor contribution to the measured background spectrum.

In summary, cosmic muons are the main contribution to the measured background spectrum. Thus, for a future experiment aiming at the observation of CNNS the suppression of muon-induced events is crucial. Ambient neutrons and gammas produced by natural radioactivity are minor contributions to the background spectrum. However, after the rejection of muon-induced events neutron and gamma background could become more important.

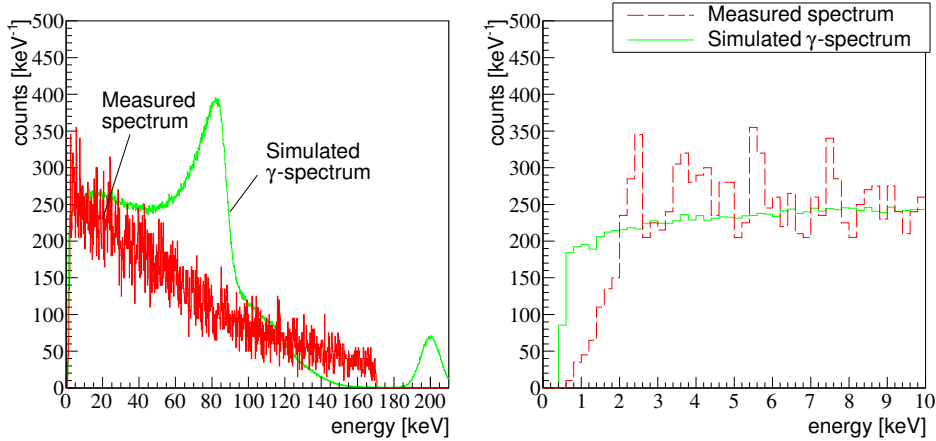


Figure 5.7: *Left panel:* Energy spectrum obtained by the simulation of gammas with an incident energy of 0.2 MeV. The simulated spectrum was scaled so that its integral is the same as the integral of the measured spectrum. The shape of the simulated spectrum is dominated by the Compton effect. The Compton edge for 0.2 MeV gammas is at ~ 88 keV and the photo peak is at 200 keV. The structure between 100 and 140 keV is due to multiple Compton scattering. For energies $\gtrsim 10$ keV there is a strong disagreement between the simulated and the measured background spectrum (compare section 3.2 and figure 3.6). See main text for further details.

Right panel: Zoom into the energy region below 10 keV. In this energy region both simulated and measured spectra are in good agreement.

5.2 Simulation of a future experiment

For the first observation of CNNS the background rate given in section 3.2 has to be reduced by a factor of $\sim 10^4$ (see also section 1.2.2 and table 1.5). To achieve this background suppression the detectors have to be surrounded by shielding of different materials. Figure 5.8 exhibits a setup of an experiment for the observation of CNNS. For this setup 125 sapphire-based low-temperature detectors are arranged in a $5 \times 5 \times 5$ cubic array. The 125 detectors are mounted in a $13 \times 13 \times 13$ cm³ cubic detector holder made from copper. Thus, all detectors have a distance of 0.5 cm to their nearest neighbours. Since the 125 low-temperature detectors are operated at a temperature of ~ 10 mK, the detectors have to be thermally shielded against the environment at room temperature. Thus, the detector array is surrounded by three concentric cylindrical radiation shields. The outer shield (300 K stainless steel shield, see figure 5.8) acts also as a vacuum chamber for a thermal insulation of the low-temperature detectors. The vacuum chamber containing the detector array is surrounded by a shielding composed of 20 cm of polyethyl-

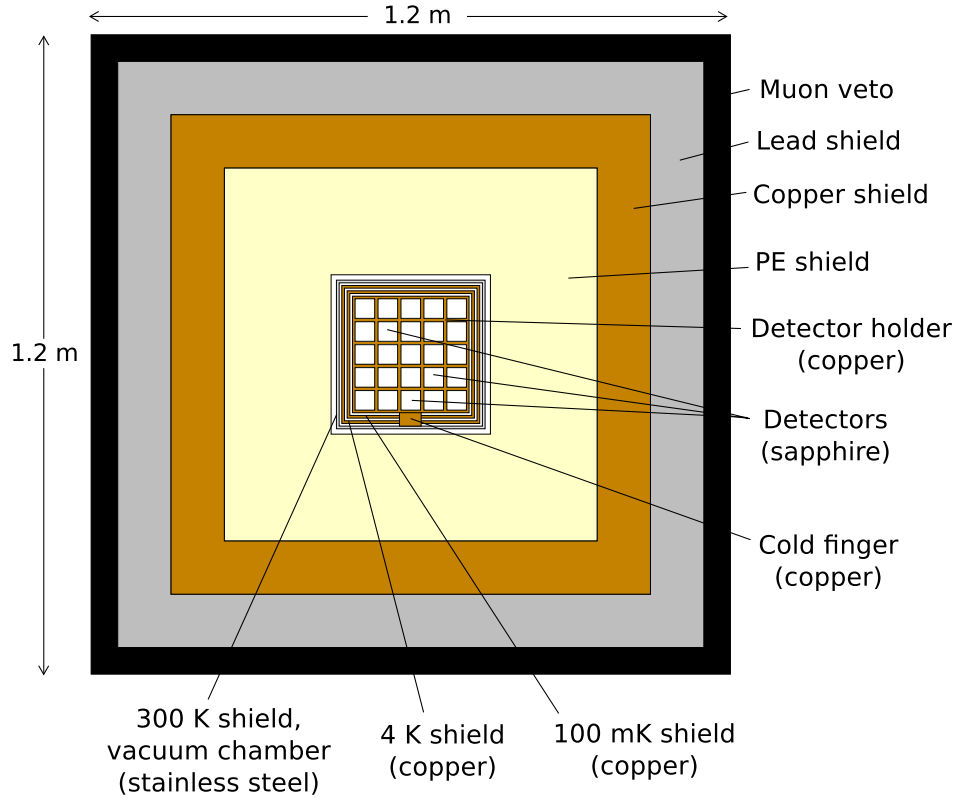


Figure 5.8: Setup of an experiment for the observation of CNNS. The 125 sapphire-based low-temperature detectors arranged in a 5x5x5 cubic array are surrounded by three radiation shields. The outer 300 K stainless steel shield is a vacuum chamber for thermal insulation of the low-temperature detectors. The vacuum chamber is surrounded by a shielding composed of 20 cm polyethylene (PE), 10 cm copper and 10 cm lead. The outer layer consisting of 5 cm plastic scintillator acts as an active muon veto.

ene (PE), 10 cm of copper and 10 cm of lead. This shielding is surrounded by an active muon veto system consisting of a 5 cm plastic-scintillator layer. A muon-veto system as the outermost layer has the advantage of detecting every muon which hits the other layers of the setup. Thus, depending on the efficiency of the muon veto a large fraction of muon-induced background events can be rejected. On the other hand, due to the large surface of an outer muon-veto system the probability that a neutrino event is rejected by the muon veto is relatively large. However, for an optimization of the setup of the shielding and the muon-veto system the fluxes of cosmic muons, gammas and ambient neutrons at the location of the experiment have to be known (see also the discussion at the end of this chapter).

For all following simulations and the resulting conclusions the setup depicted in figure 5.8 was used.

5.2.1 The use of coincident events to reject background

Since the probability for a neutrino interaction with one of the 125 detectors is very small, coincident neutrino interactions in different detectors are almost impossible. Thus, coincident events are due to background and can be rejected. The choice of the coincidence window, i.e., the maximal time difference between two events which are considered to be coincident, is crucial for the use of this background-rejection method. Too small a coincidence window leads to a poor background rejection efficiency while too wide a window leads to a large fraction of accidentally rejected neutrino events².

The length of the coincidence window depends on the time resolution σ_t of the used detectors. The time difference of the measured and the actual dates of an event is in good approximation normal distributed with width σ_t and mean 0. Thus, the time difference of two coincident background events is also normal distributed with mean 0 and width $\sqrt{2} \cdot \sigma_t$ [6]. Since $\sim 99.99\%$ of the time differences of coincident background events are contained in the interval $[-4\sqrt{2} \cdot \sigma_t, 4\sqrt{2} \cdot \sigma_t]$, the coincidence window is set to this interval.

With this rejection method it can happen that also neutrino events are rejected, if the time difference between the neutrino events and a background event in one of the other detectors is small enough. The probability for the rejection of a neutrino event due to coincident background events in other detectors depends on both the time resolution σ_t of the low-temperature detectors and the background rate R_{BG} in each detector. In addition, neutrino events can also be rejected due to pile-up, i.e., a background event in the same detector is overlapping with the neutrino event. Thus, the probability p_n that a neutrino event is not rejected is given by:

$$p_n = p(|\Delta t| \leq 4\sqrt{2} \cdot \sigma_t) \cdot p_{\text{no pile-up}}, \quad (5.4)$$

where $p(|\Delta t| \leq 4\sqrt{2} \cdot \sigma_t)$ is the probability that no background events of the 124 other detectors are in the coincidence window, i.e., the time difference Δt between the neutrino event and the background event is outside of the interval $[-4\sqrt{2} \cdot \sigma_t, 4\sqrt{2} \cdot \sigma_t]$ of the neutrino event. The second term $p_{\text{no pile-up}}$ is the probability that the neutrino event is not rejected due to pile-up.

Since the occurrence of background or neutrino events is Poisson distributed and the coincidence window has a length of $8\sqrt{2} \cdot \sigma_t$, the probability

²If a neutrino and a background event are accidentally in the coincident window, the neutrino event is rejected.

$p(|\Delta t| \leq 4\sqrt{2} \cdot \sigma_t)$ is:

$$p(|\Delta t| \leq 4\sqrt{2} \cdot \sigma_t) = e^{-124R_{BG} \cdot 8\sqrt{2} \cdot \sigma_t}, \quad (5.5)$$

assuming that the background rate R_{BG} is the same for all 125 detectors.

The probability $p_{\text{no pile-up}}$ that a neutrino event is not rejected due to pile-up depends - in addition to the background rate R_{BG} - on the length of the recorded time window $t_0 N_r$ for each pulse, where t_0 is the time base and N_r is the record length (see section 4.1). Since a background event leading to pile-up can be before or after the neutrino event, the time window for pile-up events is assumed to be two times the recorded time window. Thus, the probability $p_{\text{no pile-up}}$ is given by:

$$p_{\text{no pile-up}} = e^{-R_{BG} \cdot 2t_0 N_r}. \quad (5.6)$$

Combining equations (5.4), (5.5) and (5.6) the probability p_n that a neutrino event is not rejected can be written as:

$$p_n = e^{-124R_{BG} \cdot 8\sqrt{2} \cdot \sigma_t - R_{BG} \cdot 2t_0 N_r}. \quad (5.7)$$

For the sapphire-based low-temperature detector used in the present work with a background rate of ~ 3 Hz (see section 3.2), a time resolution of $\lesssim 1$ ms and a recorded time window of ~ 10 ms (see section 4.1) the probability that a neutrino event is *not* rejected is:

$$p_n = e^{-124 \cdot 3 \text{ Hz} \cdot 8\sqrt{2} \cdot 1 \text{ ms} - 3 \text{ Hz} \cdot 2 \cdot 10 \text{ ms}} = 1.4 \%. \quad (5.8)$$

Thus, for the measured background rate of ~ 3 Hz (see section 3.2) the present detector is much too slow for the use of the rejection of pile-up and coincident events.

For the given length of the recorded time window the probability to reject a neutrino event due to pile up is $\sim 6\%$ ($p_{\text{no pile-up}} \approx 94\%$). However, this probability can be reduced, for instance, by fitting the sum of several templates to a pulse with pile-up. In [70] a method is described to fit a template to one of the pulses in a pile-up event. This method could be expanded to fit each pulse in a pile-up event as long as enough information of each pulse is contained in the recorded time window. If two pulses in a pile-up event are too close together, it will not be possible to separate the pulses. Such events will most likely be treated as a single event. Thus, the probability to accept a neutrino event is modified to

$$p_n^{\text{mod}} = e^{-125R_{BG} \cdot 8\sqrt{2} \cdot \sigma_t}. \quad (5.9)$$

For an acceptance of 90 % of the neutrino events the time resolutions σ_t of the low-temperature detectors have to be:

$$\sigma_t = -\frac{\ln(0.9)}{125 \cdot 3 \text{ Hz} \cdot 8\sqrt{2}} \approx 25 \mu\text{s}. \quad (5.10)$$

If the method to use pile-up events described above can not be applied, e.g., due to limited calculation time, the time resolution has to be $\sim 10 \mu\text{s}$ for an acceptance of 90 % for neutrino events. Since low-temperature detectors can have time resolutions of $\sim 6 \mu\text{s}$ [70], an acceptance of $\gtrsim 90 \%$ for neutrino events can be reached for the use of coincident events to reject background.

5.2.2 Cosmic muon background

To study cosmic muons as a background source $\sim 27 \cdot 10^6$ muons and their secondary particles have been simulated. The energy and the angular distributions were the same as the distributions used in section 5.1.1 and [59]. The left panel of figure 5.9 shows the simulated energy spectrum below $\sim 10 \text{ keV}$. The peak at $\sim 8 \text{ keV}$ is due to copper fluorescence in the detector holder. This copper fluorescence is induced by cosmic muons. The so-called single hits are events where energy above a threshold of 0.5 keV is deposited in only one detector. Thus, single hits with an energy deposition below $\sim 4 \text{ keV}$ have the same signature as neutrino events. There are also single hits with energy depositions above 4 keV . However, it is unlikely that events with energies above $\sim 4 \text{ keV}$ are due to neutrinos, since only $\sim 1 \%$ of all expected neutrino events are above 4 keV (see section 1.2.2). For the spectrum of all detectors the sum of the energy depositions above the threshold in all detectors was used. For energies $\lesssim 10 \text{ keV}$ the majority of the events are single hits. Thus, the efficiency for the rejection of the cosmic muon background using coincident events is only a few percent for this energy region (see right panel of figure 5.9).

Since the main part of the measured background spectrum (see section 3.2 and figure 3.6) is due to cosmic muons (see section 5.1.1), the muon background has to be suppressed by a factor of $\sim 10^4$ for the observation of CNNS (see section 1.2.2 and table 1.5). An active muon veto based on plastic scintillator is able to detect $\gtrsim 99.99 \%$ of all muons crossing the veto[71]. For the rejection of background events induced by cosmic muons the events in the low-temperature detectors have to be in coincidence with an event in the muon veto system. Due to the large time resolution of a low-temperature detector ($\sim 10 \mu\text{s}$) the events in the muon veto system have to be in a coincid-

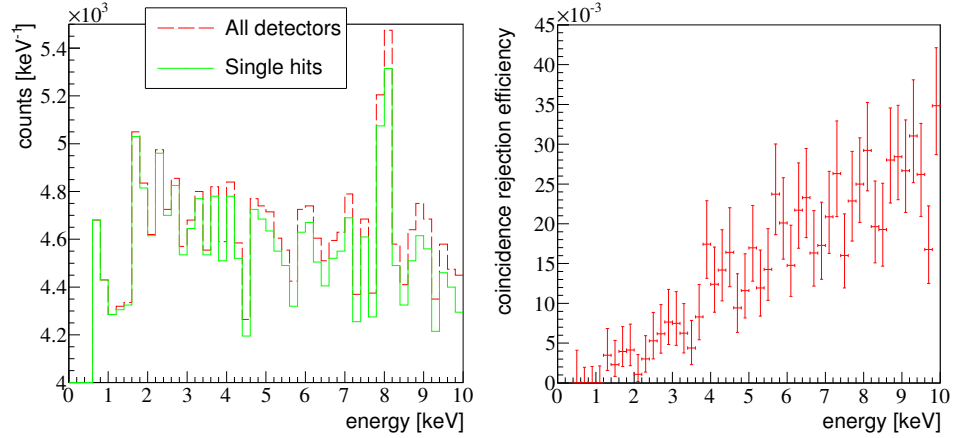


Figure 5.9: *Left panel:* Energy spectrum obtained by the simulation of $\sim 27 \cdot 10^6$ cosmic muons and their secondary particles. For the spectrum of single hits only events with an energy deposition above a threshold of 0.5 keV in only one detector were taken into account. For the spectrum of all detectors the sum of the energy depositions above the threshold in all detectors was used. Small energy depositions ($\lesssim 10$ keV) are mainly due to single hits. The peak at ~ 8 keV is due to copper fluorescence induced by cosmic muons in the detector holder.

Right panel: Simulated rejection efficiency concerning coincident events for deposited energies below ~ 10 keV. For this energy region only a few percent of the background events can be rejected. Thus, for the rejection of the cosmic muon background a good muon veto is needed. For energies $\gtrsim 10$ keV (not shown) the rejection efficiency increases to ~ 50 % for an energy of ~ 1 MeV.

ence window³ of ~ 80 μ s to reject ~ 99.99 % of the muon induced background events.

The flux of cosmic muons is ~ 1 $\text{cm}^{-2}\text{min}^{-1}$ [6] for horizontal detectors at sea level. Depending on the size of the shielding and the muon veto system (see figure 5.8) a fraction of the muons crossing the veto system are not depositing energy in any of the 125 low-temperature detectors. However, these muons can still cause the rejection of a neutrino event, if both events happen to be in coincidence. Since also the events in the muon veto system are Poisson distributed, the probability p_n^μ that a neutrino event is accepted

³The coincidence window is given by the length of the interval $[-4\sigma_t, 4\sigma_t]$. The factor $\sqrt{2}$ used for the coincidence window in section 5.2.1 is due to the bad time resolutions of two low-temperature detectors. This factor is not needed for the rejection of muon-induced background, since the time resolution of a plastic-scintillator based muon-veto is much better ($\lesssim 10$ ns).

by the muon veto system is given by:

$$p_n^\mu = e^{-A_{eff} \cdot \Phi_\mu \cdot 8\sigma_t} \approx 90\%, \quad (5.11)$$

where A_{eff} is the effective area of the muon veto system, $\Phi_\mu = 1 \text{ cm}^{-2}\text{min}^{-1}$ is the muon flux and $\sigma_t = 10 \mu\text{s}$ is the time resolution of the low-temperature detectors. Since the majority of muons are moving downward (polar angle $\theta < 90^\circ$), the bottom part of the muon veto system (see figure 5.8) is only crossed by muons which also cross either the top part or one of the side parts. Thus, the effective area A_{eff} is increased to $A_{eff} = 5 \cdot 1.2 \times 1.2 \text{ m}^2$ which is five times the size of the top part of the muon veto. The polar-angle distribution of cosmic muons is approximately proportional to $\cos^2 \theta$ [6] leading to a smaller muon flux through the side parts of the muon veto compared to the top part. Thus, the effective area A_{eff} is a rather conservative choice.

Depending on the depth and the wall thickness of the site chosen for an experiment for the observation of CNNS the muon flux $\Phi_\mu = 1 \text{ cm}^{-2}\text{min}^{-1}$ can be smaller by a factor of $\lesssim 3$. So even if a time resolution of $\sim 10 \mu\text{s}$ can not be reached, a probability $p_n^\mu \sim 90\%$ for the acceptance of a neutrino event is possible for a real experiment.

5.2.3 Ambient neutron background

In section 5.1.2 is pointed out that ambient neutrons are marginally contributing to the measured background spectrum (see section 3.2 and figure 3.6). However, after the rejection of a large part of the muon-induced background (see section 5.2.2) ambient neutrons are becoming an important background source. To study their suppression two simulations were performed.

For the first simulation about 10^8 neutrons and their secondary particles were simulated to study suppression of neutrons due to the shielding of the setup shown in figure 5.8. Therefore, the neutrons were started outside of the shielding and the number of neutrons crossing the shielding was recorded to determine the probability p_{shield} that a neutron is stopped by the shielding to:

$$p_{shield} = (98.633 \pm 0.002)\%. \quad (5.12)$$

To increase the suppression of ambient neutrons the thickness of the different layers of the shielding have to be increased. However, that would result in a larger muon veto leading to a decreased probability p_n^μ that a neutrino event is accepted by the muon veto system. Thus, the thickness of the shielding depends on the actual rate of ambient neutrons and cosmic muons at the site of an experiment for the observation of CNNS.

To study the rejection efficiency of neutron-induced background events using coincident events (see section 5.2.1) about 10^9 ambient neutrons and their secondary particles were simulated. For this simulation only the inner parts⁴ of the setup shown in figure 5.8 were taken into account to save computation time. Small variations of the energy spectrum of ambient neutrons are not important for the following statements. The energy spectrum is changed only slightly due to the shielding. Thus, for this simulation the same energy spectrum was used as that for the simulation of the suppression of neutrons due to the shielding and for the simulation of the neutron background for the measured spectrum (see section 5.1.2). The left panel of

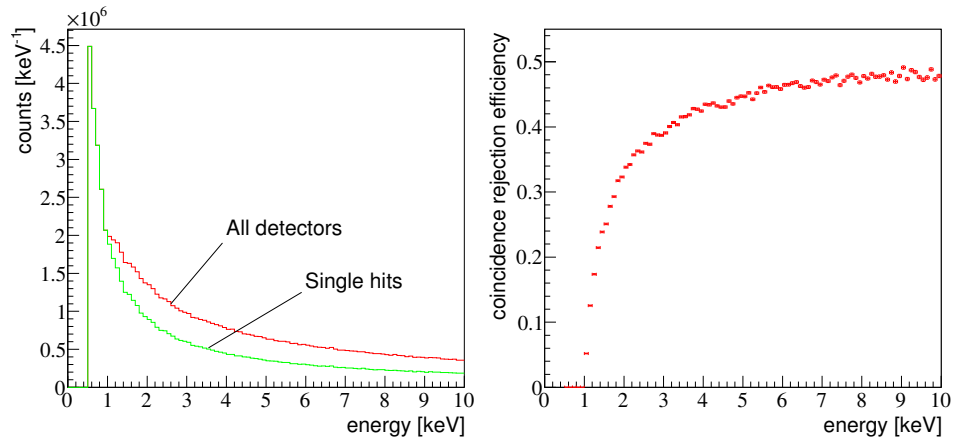


Figure 5.10: *Left panel:* Energy spectrum obtained by the simulation of $\sim 10^9$ ambient neutrons and their secondary particles. For this simulation only the inner parts (i.e., the radiation shields, the cold finger, the detector holder and the 125 detectors) were taken into account. For the spectrum of all detectors the sum of all energy depositions above a threshold of 0.5 keV in all detectors was used. For the spectrum of single hits only events with an energy deposition above the threshold (0.5 keV) in only one detector were taken into account.

Right panel: For the rejection of an event due to coincidences the energy deposition in at least two detectors has to be above the threshold of 0.5 keV. Thus, the rejection efficiency below a deposited energy of 1 keV is vanishing. For higher energies up to ~ 10 keV the rejection efficiency steeply increases to $\sim 50\%$.

figure 5.10 shows the energy spectrum obtained by the simulation of $\sim 10^9$ ambient neutrons and their secondary particles. For the spectrum of single hits only events with an energy deposition above the threshold of 0.5 keV in only one detector were used. For the energy spectrum of all detectors the sum of all energy depositions above the threshold was taken into account.

⁴i.e., the radiation shields, the cold finger, the detector holder and the 125 detectors.

Since for the rejection of an event due to coincidences the energy deposition in at least two detectors has to be above the energy threshold of 0.5 keV, the rejection of background events is only possible for deposited energies above 1 keV. Thus, the rejection efficiency (see the right panel of figure 5.10) vanishes for energies below ~ 1 keV. The efficiency steeply increases up to $\sim 50\%$ for energies of $\lesssim 10$ keV. For the energy region $\lesssim 4$ keV used for the observation of CNNS the rejection efficiency is about 20 to 30%. Thus, the suppression of background events induced by ambient neutrons is mainly due to the shielding surrounding the experiment (see figure 5.8).

5.2.4 External and internal gamma background

External gamma background generated by natural radioactivity is only a small contribution to the measured background spectrum (see section 5.1.3). Also for an experiment for the observation of CNNS external gammas are strongly suppressed ($\mathcal{O}(10^5)$ for 1 MeV gammas) due to the shielding surrounding the detector array (see figure 5.8). However, if the thickness of the shielding is reduced to increase the acceptance p_n^μ of neutrino events (see section 5.2.2), the external gamma background could become more important.

Internal radioactivity, i.e., radioactive decays inside the detector holder or the sapphire-based detectors, can be a serious background source, since such events can only be rejected due to coincidences. The majority of the naturally occurring long-lived radioactive isotopes are decaying into an alpha- or beta-particle and a daughter nucleus. Since both alphas and betas have a very short range in copper and sapphire, they deposit their energy in only one detector. However, since the energy deposited by alphas or betas is in most cases very large ($\gg 4$ keV), neither alphas nor betas are a serious background source for the observation of CNNS.

Events where a radioactive isotope is decaying directly at the surface of a detector and only the daughter nucleus deposits energy in the detector are a background source, since the energy deposited by the daughter nucleus can be very small. However, the rate for such events is typically much smaller than the allowed background rate (see section 1.2.2 and table 1.5).

In addition to the decay products (alphas, betas and daughter nuclei) also gammas are generated, since radioactive isotopes are frequently decaying into an excited state of the daughter nucleus. This excited state is relaxed by the emission of one or more gammas with energies up to ~ 2.6 MeV. These gammas can be a background source for the observation of CNNS, since they have long ranges and can also deposit a small amount of energy ($\lesssim 4$ keV) due to Compton scattering. However, due to their long range a large fraction of the gammas can be rejected using coincidences.

To study the influence and the rejection of gamma background generated by internal radioactivity a simulation was performed. For this simulation gammas with different energies between 0.1 and 2.5 MeV were simulated. For each gamma energy, 10^6 gammas and their secondary particles were simulated. The starting positions of the gammas were uniformly distributed in the detector array and the copper holder (see figure 5.8). In addition, the starting directions were chosen to be isotropic.

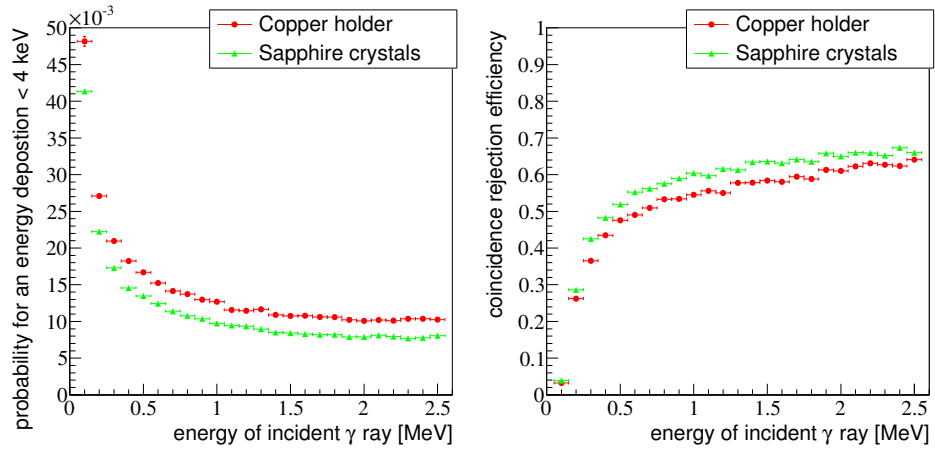


Figure 5.11: *Left panel:* Probability $p(E_{dep} < 4 \text{ keV})$ to generate a neutrino-like event for different gamma energies. An event is considered to be neutrino-like, if the deposited energy E_{dep} in one detector is below 4 keV but above the threshold of 0.5 keV. Events are also considered to be neutrino-like, if energy above the threshold is deposited in other detectors. The probabilities to generate neutrino-like events are shown separately for starting points in the copper holder and the sapphire crystals.

Right panel: Rejection efficiency for neutrino-like events using coincidences. For small gamma energies ($\lesssim 0.5 \text{ MeV}$) the rejection efficiency is small, since it is unlikely that energy above the threshold is deposited in more than one detector. For gamma energies $\gtrsim 1 \text{ MeV}$ the rejection efficiency reaches $\sim 60\%$.

The results of this simulation are depicted in figure 5.11. The left panel shows the probability $p(E_{dep} < 4 \text{ keV})$ to generate a neutrino-like event, i.e., an event with an energy deposition E_{dep} below 4 keV but above the threshold of 0.5 keV in at least one detector. Also events with energy depositions above the threshold in more than one detector are considered to be neutrino-like, if there is at least one detector with an energy deposition below 4 keV.

Thus, it is also possible to reject a fraction of these neutrino-like events due to coincidences in different detectors. The right panel of figure 5.11 exhibits the rejection efficiency $\eta_{\text{coincidence}}$ for neutrino-like events using coincidences. For gamma energies below $\sim 0.5 \text{ MeV}$ this rejection efficiency

is very small due to the small probability that energy is deposited in more than one detector for such low gamma energies. For gamma energies above ~ 1 MeV the rejection efficiency is $\sim 60\%$.

Using both the probability $p(E_{dep} < 4 \text{ keV})$ and the rejection efficiency $\eta_{coincidence}$ the maximal allowed activities A_{max} of the detector holder and the sapphire crystals can be estimated:

$$A_{max} = \frac{R_{BG}^{max}}{p(E_{dep} < 4 \text{ keV})(1 - \eta_{coincidence})}, \quad (5.13)$$

where R_{BG}^{max} is the maximal allowed rate for the gamma background induced by internal radioactivity. Figure 5.12 shows the maximal allowed activit-

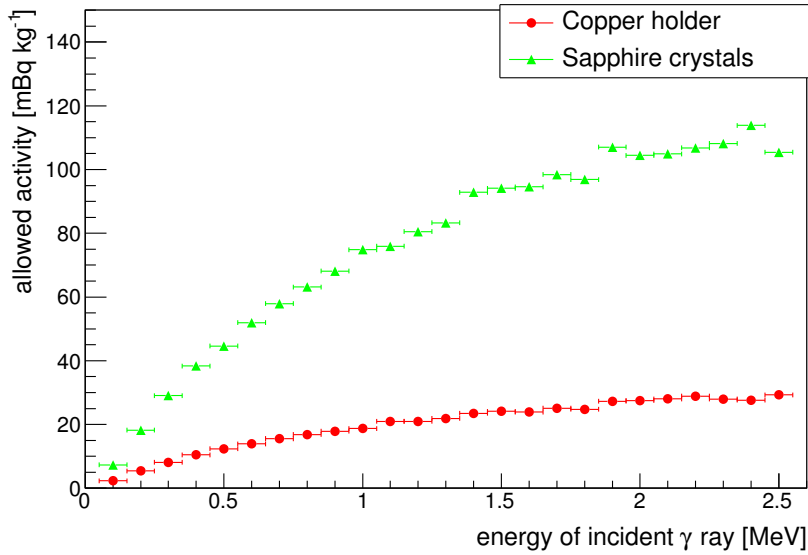


Figure 5.12: Allowed gamma activity for the copper holder and the sapphire crystals leading to ~ 100 accepted background events per day for each gamma energy. Since the copper holder used for the simulations described in this chapter (see figure 5.8) has a mass of ~ 11 kg, its allowed radioactivity is smaller than for the sapphire crystals. However, for an experiment for the observation of CNNS the detector holder has to provide space for the electric contacts of the detectors leading to a smaller mass and also to a larger allowed activity.

ies A_{eff} per mass for different gamma energies. For each gamma energy a maximal background rate of $R_{BG}^{max} = 100$ events per day with an energy deposition below 4 keV and accepted by a cut on coincident events in different detectors was chosen.

Since both the probability $p(E_{dep} < 4 \text{ keV})$ and the rejection efficiency $\eta_{coincidence}$ are given separately for gammas with starting points in the copper holder and the sapphire crystals, also the allowed activities are given

separately. The allowed activity per mass of the copper holder is smaller than for the sapphire crystals (~ 4 kg) due to the large mass of the copper holder (~ 11 kg). However, for an experiment for the observation of CNNS the copper holder has to provide space for the wires used for the electric contacts of the low-temperature detectors leading to a smaller mass and thus to a higher allowed activity.

For the majority of the different materials listed in [72] the activities of the gamma rays generated by natural radioactivity are of $\mathcal{O}(1 \text{ mBq kg}^{-1})$ which is well below the allowed activities for the copper holder as well as the sapphire crystals shown in figure 5.12. Although neither the activity of copper nor sapphire were measured in [72], it can be assumed that copper and sapphire can be produced with the same radiopurity as ordinary steel which was measured in [72].

In summary, it has to be pointed out that neither ambient neutrons nor gammas generated by internal radioactivity are serious background sources for the observation of CNNS. The suppression of cosmic muons as the main background is crucial for the observation of CNNS and strongly depends on the time resolution of the low-temperature detectors (see section 5.2.2) used in a CNNS experiment.

The site chosen for a future experiment aimed at the observation of CNNS has a big influence on the both background composition and rate. For the use of reactor neutrinos sites with different distances to the core have been studied (see section 1.2.2 and table 1.5). For technical, safety and security reasons the most favorable site would be in ~ 40 m distance to a power reactor with a thermal power of ~ 4 GW. In that distance the natural background (cosmic muons, ambient neutrons, natural radioactivity) is dominating. Depending on the wall thickness and the overburden of a laboratory the muon flux can be smaller by a factor of $\lesssim 3$ than at the surface. The flux of ambient neutrons depends on the muon flux and also on the wall thickness, since ambient neutrons are produced by cosmic muons in the walls surrounding the experiment. The external gamma background, however, depends only on the activity of the materials surrounding the experiment, e.g., the walls of the laboratory.

For the investigation of physics beyond the standard model (see chapter 7) a site with a smaller distance to the reactor core of $\lesssim 15$ m could be more suitable due to the much higher flux of neutrinos. For a site that close to the reactor core additional background sources like thermal neutrons and high-energetic gamma rays ($E_\gamma \gtrsim 3$ MeV) from the reactor core could appear. To handle this additional background it might be necessary to modify the setup shown in figure 5.8. For both thermal neutrons and high-energetic gamma rays the thickness of the shielding has to be increased. That would, however,

also increase the size of the muon veto leading to larger fraction of neutrino events rejected by the muon veto (see section 5.2.2). Thus, to have both an efficient shielding against thermal neutrons and high-energetic gamma rays and also a small muon veto rejecting only a small fraction of neutrino events, it could be necessary to build a muon veto surrounding only the detector array and its thermal shielding and a thick shielding surrounding this muon veto. With such a setup it can happen that a muon is producing a neutron in the shielding without crossing the muon veto. Thus, events generated by such neutrons can not be rejected as muon-induced events. However, depending on the muon flux the rate of such events can be small enough to allow the observation of CNNS and also physics beyond the standard model.

Thus, before the final setup of the experiment (e.g., design of the detector holder, thickness of the shielding, size of the muon veto system) is configured, the fluxes and energy spectra of cosmic muons, neutrons and gammas have to be measured in the laboratory used for the experiment. With these measured fluxes and energy spectra additional simulations can be performed to optimize the setup of the experiment for the chosen laboratory.

Chapter 6

Observation potential for a future CNNS experiment

In section 1.2.2 the allowed background rate for the observation of CNNS using reactor neutrinos was calculated. For this calculation, however, it was assumed that the uncertainty of the number of background events is only due to Poisson statistics. Also the spectral shapes neither of the neutrino signal nor of the background events were taken into account. In the present chapter the potential for the observation of CNNS is estimated using a Bayesian approach¹.

6.1 Hypothesis testing and Bayes' theorem

One way to claim an observation of CNNS is to reject the Hypothesis H: “*All events are due to background.*” on a certain confidence level. For that purpose the conditional probability $p(\text{H}|\text{Spectrum})$ - that the hypothesis H is true given the measured Spectrum - has to be calculated. This can be done using Bayes' theorem[73]:

$$p(\text{H}|\text{Spectrum}) = \frac{p(\text{Spectrum}|\text{H})p_0(\text{H})}{p(\text{Spectrum})}, \quad (6.1)$$

where $p(\text{Spectrum}|\text{H})$ is the conditional probability that the measured spectrum occurs given that hypothesis H is true, $p_0(\text{H})$ is the prior probability²

¹The calculations and fits in this chapter follow the Bayesian analysis described in [73]. The calculations and fits were performed using the Bayesian Analysis Toolkit (BAT)[74].

²Prior probabilities are used to model the prior belief in a parameter or a hypothesis before an experiment is performed.

for hypothesis H, and $p(\text{Spectrum})$ is the normalization and can be rewritten as:

$$p(\text{Spectrum}) = p(\text{Spectrum}|\text{H})p_0(\text{H}) + p(\text{Spectrum}|\bar{\text{H}})p_0(\bar{\text{H}}), \quad (6.2)$$

where $\bar{\text{H}}$ is the negation of hypothesis H and $p_0(\bar{\text{H}})$ its prior probability.

The prior probabilities $p_0(\text{H})$ and $p_0(\bar{\text{H}})$, respectively, depend on the prior knowledge and all additional information available for the experiment. However, since no experiment was able to observe CNNS up to now, there is no reason to favor or disfavor the background-only hypothesis H. Thus, the prior probabilities for both H and $\bar{\text{H}}$ are chosen to be equal:

$$p_0(\text{H}) = p_0(\bar{\text{H}}) = 0.5. \quad (6.3)$$

The probabilities $p(\text{Spectrum}|\text{H})$ and $p(\text{Spectrum}|\bar{\text{H}})$ are correlated with the expected numbers of background events B and signal events S:

$$p(\text{Spectrum}|\text{H}) = \int p(\text{Spectrum}|B)p_0(B)dB \quad (6.4)$$

$$p(\text{Spectrum}|\bar{\text{H}}) = \int p(\text{Spectrum}|B, S)p_0(B)p_0(S)dBdS, \quad (6.5)$$

where $p_0(B)$ and $p_0(S)$ are the prior probabilities for the expected number of background and signal events, respectively. Since the bin-entries n_i are Poisson distributed, the conditional probabilities $p(\text{Spectrum}|B)$ and $p(\text{Spectrum}|B, S)$ are given by:

$$p(\text{Spectrum}|B) = \prod_{i=1}^{N_b} \frac{\lambda_i(B, 0)^{n_i}}{n_i!} e^{-\lambda_i(B, 0)} \quad (6.6)$$

$$p(\text{Spectrum}|B, S) = \prod_{i=1}^{N_b} \frac{\lambda_i(B, S)^{n_i}}{n_i!} e^{-\lambda_i(B, S)}, \quad (6.7)$$

where N_b is the number of bins in the measured spectrum and $\lambda_i(B, S)$ is the expected value for each bin i and is given by:

$$\lambda_i(B, S) = B \cdot \int_{\Delta E_i} dE f_B(E) + S \cdot \int_{\Delta E_i} dE f_S(E), \quad (6.8)$$

where $f_B(E)$ and $f_S(E)$ are the normalized shapes³ of the known background and signal spectra.

³ $\int_0^\infty dE f_B(E) = \int_0^\infty dE f_S(E) = 1$

With the known normalized functions $f_B(E)$ and $f_S(E)$ and all prior probabilities p_0 described in this section the conditional probability $p(H|\text{Spectrum})$ that the background-only hypothesis H is true given a measured spectrum can be calculated. If the probability $p(H|\text{Spectrum})$ is below a predefined value, e.g. 10^{-4} , the background-only hypothesis is wrong, i.e., an observation of CNNS can be claimed (in this example on a confidence level of $> 3\sigma$).

It has to be mentioned that the probability $p(H|\text{Spectrum})$ - and hence also the claim of an observation of CNNS - strongly depends on the prior probabilities $p_0(B)$ and $p_0(S)$ for the number of background and signal events. Thus, the measurement of the background spectrum in reactor-off periods and also systematic errors on the background rate due to seasonal variations of the muon flux are crucial for the observation of CNNS.

6.2 Parameter estimation and observation potential

To study the observation potential of a future CNNS experiment four ensembles of energy spectra have been simulated. Different background rates R_B and neutrino rates R_S were used to simulate 2000 energy spectra of each ensemble. For one ensemble the neutrino rate was $R_S = 0$ in order to study, if an observation of CNNS could be claimed for a spectrum containing only background events. The background rate was set to $R_B = 1000 \text{ kg}^{-1} \text{ day}^{-1}$ for the simulation of these background-only spectra. For the other ensembles the neutrino rate was set to ~ 3.3 neutrino events per kg-day for the energy region between 0.5 keV (threshold) and 4 keV. For this neutrino rate a dead time of 20% due to the background rejection techniques described in chapter 5 was assumed. The background rates of these three ensembles containing neutrino events were set to 1000, 1500 and 2000 background events per kg-day in the energy region between 0.5 keV and 4 keV. These background rates R_B correspond to a background rejection of $\sim 99.9\%$ of the measured background (see section 3.2).

For the simulation of a spectrum first the numbers of neutrino and background events are chosen randomly following a Poisson distribution, the expected numbers for the neutrino signal and background events being the

means of the distributions:

$$p(N_S) = \frac{(T_0 R_S)^{N_S}}{N_S!} e^{-T_0 R_S} \quad (6.9)$$

$$p(N_B) = \frac{(T_0 R_B)^{N_B}}{N_B!} e^{-T_0 R_B}, \quad (6.10)$$

where N_S is the total number of neutrino events and N_B the total number of background events, respectively. For all simulated spectra an exposure T_0 of 4 kg-years was assumed corresponding to a measuring time of one year using the setup depicted in figure 5.8 of section 5.2. It has to be emphasized that N_B and N_S are the total numbers of background and neutrinos events which were used to generate the spectra. So for each simulated spectrum N_B and N_S are the actual numbers of background and neutrino events contained in the spectrum. On the other hand, the numbers B and S are free parameters describing the total number of background and neutrino events. The numbers B and S are obtained from a fit of a model to the simulated spectra. Thus, N_B and N_S are the expected values for B and S , respectively.

To generate an energy spectrum the energies of $(N_S + N_B)$ events were chosen randomly according to the functions $f_S(E)$ for the N_S neutrino events and $f_B(E)$ for the N_B background events. Since cosmic muons are the main background source (see chapter 5), an exponential was used for the normalized function $f_B(E)$ describing the shape of the background spectrum:

$$f_B(E) = \frac{1}{a_0} e^{-\frac{E}{a_0}}, \quad (6.11)$$

where the parameter $a_0 = 79.6$ was obtained by the fit of an exponential to the measured background spectrum (see section 3 and figure 3.6). For a future experiment aiming at the observation of CNNS the background spectrum measured during reactor-off periods should be used for the background model $f_B(E)$.

The calculated recoil-energy spectrum for reactor neutrinos (see section 1.2.2 and figure 1.6) was used for the signal model $f_S(E)$. Also this calculation has to be adjusted to the actual fuel composition of the reactor used in a future CNNS experiment. In figure 6.1 a simulated spectrum with $R_B = 1000 \text{ kg}^{-1} \text{ day}^{-1}$ and $R_S \approx 3.3 \text{ kg}^{-1} \text{ day}^{-1}$ is depicted. To calculate the conditional probability $p(\text{H}|\text{Spectrum})$ that the background-only hypothesis H is true given the simulated spectrum, the prior probabilities for both the number of background events B and the number of neutrino events S have to be determined. Since CNNS has not been observed up to now, the prior

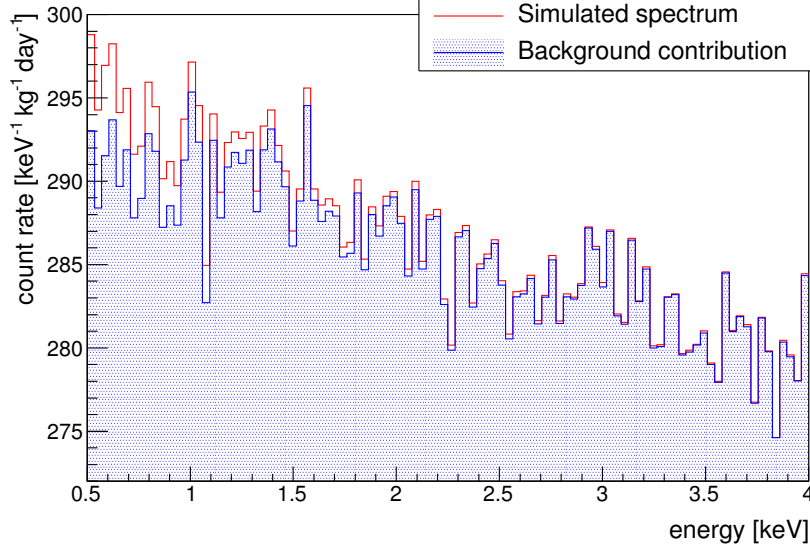


Figure 6.1: Simulated spectrum for an experiment aiming at the observation of CNNS. For the background contribution an average rate R_B of 1000 background events per kg-day was used. For the shape of the background distribution the exponential fitted to the measured background spectrum (see section 3.2 and figure 3.6) was used. The average neutrino rate R_S used for this spectrum was ~ 3.3 neutrino events per kg-day. The shape of the neutrino contribution follows the calculated recoil-energy spectrum for reactor neutrinos (see section 1.2.2 and figure 1.6). For the simulation of this spectrum an exposure of 4 kg-years was assumed.

probability $p_0(S)$ for the numbers of neutrino events is chosen to be flat:

$$p_0(S) = \begin{cases} \frac{1}{S_{max}} & \text{for } S \leq S_{max} \\ 0 & \text{for } S > S_{max} \end{cases}, \quad (6.12)$$

where S_{max} is the maximal allowed number of neutrino events. For the calculations and fits described in this chapter S_{max} was set to $2T_0R_S$ which is twice the mean of S (see equation (6.9)).

The background rate can be estimated by the measurement of the background spectrum during reactor-off periods. Since a power reactor is turned off for about one month per year, the uncertainty of the background rate is dominated by systematical errors like seasonal modulations of the muon flux or background generated by the reactor. Thus, for the prior probability $p_0(B)$ for the number B of background events a normal distribution with T_0R_B as mean and a width of 10% was chosen:

$$p_0(B) = \frac{1}{0.1 \cdot T_0R_B \sqrt{2\pi}} e^{-\frac{1}{2} \left(\frac{B - T_0R_B}{0.1 \cdot T_0R_B} \right)^2}. \quad (6.13)$$

With these prior probabilities $p_0(B)$ and $p_0(S)$, with the functions $f_B(E)$ and $f_S(E)$ (the calculated recoil-energy spectrum for reactor neutrinos, see section 1.2.2 and figure 1.6), and with the equations given in section 6.1 the conditional probability $p(H|\text{Spectrum})$ can be calculated. For the simulated spectrum shown in figure 6.1 the result of this calculation is

$$p(H|\text{Spectrum}) = 1.953 \cdot 10^{-5}. \quad (6.14)$$

Thus, for this simulated spectrum the background-only hypothesis is strongly disfavored and an observation of CNNS could be claimed.

As a further check of the plausibility of the claimed observation of CNNS the numbers B of background events and S of neutrino events included in the simulated spectrum can be estimated. The number B of background events is the only free parameter for the background-only model. To estimate its most likely value the conditional probability $p(B|\text{Spectrum})$ that the given spectrum contains B background events has to be maximized. For a model containing both background and signal events the conditional probability $p(B, S|\text{Spectrum})$ has to be maximized to obtain the most likely values for the parameters B and S . According to Bayes' theorem these probabilities are given by:

$$p(B|\text{Spectrum}) = \frac{p(\text{Spectrum}|B)p_0(B)}{\int p(\text{Spectrum}|B)p_0(B)dB} \quad (6.15)$$

$$p(B, S|\text{Spectrum}) = \frac{p(\text{Spectrum}|B, S)p_0(B)p_0(S)}{\int p(\text{Spectrum}|B)p_0(B)p_0(S)dBdS}, \quad (6.16)$$

where the conditional probabilities $p(\text{Spectrum}|B)$ and $p(\text{Spectrum}|B, S)$ are given by equations (6.6) and (6.7).

To find the global maxima of the conditional probabilities $p(B|\text{Spectrum})$ and $p(B, S|\text{Spectrum})$ a Markov chain[74][75] was used to scan the complete parameter space. The resulting maxima are then used as starting points for a minimization algorithm for a precise estimation of the parameters B and S . Figure 6.2 depicts the results of the fits of the background-only model $f_B(E)$ and a model $f_S(E)$ containing background and signal to the simulated spectrum. The background rate estimated by the background-only model is

$$R_B = \frac{B}{T_0} = 1003.38 \pm 0.83 \text{ kg}^{-1} \text{ day}^{-1}, \quad (6.17)$$

which is *not* in agreement with the rate of $R_B = 1000 \text{ kg}^{-1} \text{ day}^{-1}$ used for the simulation of the spectrum. For the model containing background and

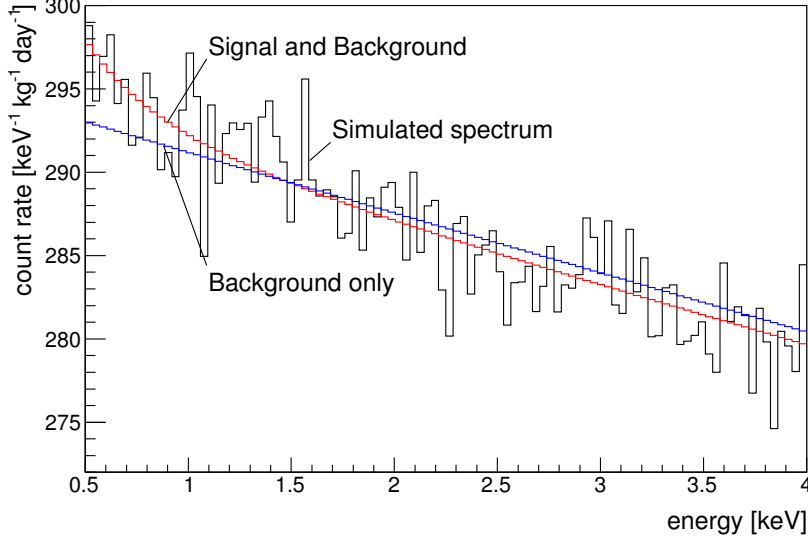


Figure 6.2: Fits of two different models to the simulated spectrum shown in figure 6.1. The estimated value for the background rate obtained by the fit of the background-only model to the spectrum is $R_B = 1003.38 \pm 0.83 \text{ kg}^{-1} \text{ day}^{-1}$. The fit of a model containing background and signal to the spectrum leads to a background rate of $R_B = 1000.48 \pm 1.01 \text{ kg}^{-1} \text{ day}^{-1}$ and a neutrino rate of $2.89 \pm 0.58 \text{ kg}^{-1} \text{ day}^{-1}$. The fit results are also showing that the simulated spectrum can not be described by the background-only model, since the fitted value for the background rate R_B in the background-only model is not in agreement with the expected value of $R_B = 1000 \text{ kg}^{-1} \text{ day}^{-1}$.

signal the fitted parameters are

$$R_B = \frac{B}{T_0} = 1000.48 \pm 1.01 \text{ kg}^{-1} \text{ day}^{-1} \quad (6.18)$$

$$R_S = \frac{S}{T_0} = 2.89 \pm 0.58 \text{ kg}^{-1} \text{ day}^{-1}. \quad (6.19)$$

The background rate of this model is in agreement with the expected rate of $R_B = 1000 \text{ kg}^{-1} \text{ day}^{-1}$. Also the signal rate is in reasonable agreement with the expected rate of $R_S = 3.3 \text{ kg}^{-1} \text{ day}^{-1}$. Thus, also the estimated parameters for the background rate R_B and neutrino rate R_S disfavor the background-only model.

The calculation of the conditional probability $p(\text{H}|\text{Spectrum})$ as well as the fit of both models to the simulated spectra were performed for each spectrum in the four ensembles to study the observation potential of a future experiment aiming at the observation of CNNS. Figure 6.3 exhibits the distributions of the conditional probabilities $p(\text{H}|\text{Spectrum})$ for all ensembles of

simulated spectra. For none of the 2000 simulated spectra containing only background events the probability $p(\text{H}|\text{Spectrum})$ is below the observation threshold of 10^{-4} . Thus, a false claim of the observation of CNNS is very unlikely. The observation potentials, i.e., the fraction of spectra with a probability $p(\text{H}|\text{Spectrum})$ below 10^{-4} (represented by the black vertical lines in figure 6.3), for the other three ensembles containing background and neutrino events are:

- 83.55 % for a mean background rate of $R_B = 1000 \text{ kg}^{-1} \text{ day}^{-1}$
- 51.95 % for a mean background rate of $R_B = 1500 \text{ kg}^{-1} \text{ day}^{-1}$
- 28.10 % for a mean background rate of $R_B = 2000 \text{ kg}^{-1} \text{ day}^{-1}$

The observation potential of an experiment aiming at the observation of CNNS is $\sim 50\%$ if the background rate is $\lesssim 1500 \text{ kg}^{-1} \text{ day}^{-1}$ and a neutrino rate of $\sim 3.3 \text{ kg}^{-1} \text{ day}^{-1}$. For this neutrino rate, a laboratory in $\sim 40 \text{ m}$ distance to a power reactor with a thermal power of $\sim 4 \text{ GW}$ and a dead time of $\sim 20\%$ due to background rejection was assumed. Since the recoil energies of reactor neutrinos are small ($\lesssim 4 \text{ keV}$), both the rate and the shape of the background spectrum can be monitored at energies above $\sim 4 \text{ keV}$.

For a laboratory closer to the reactor, background generated by the reactor could become more important. Especially neutrons generated by nuclear fission can lead to a dangerous background source, since their recoil-energy spectrum is similar to that of reactor neutrinos. Thus, a neutron detector is needed to monitor the neutron flux during the measurements.

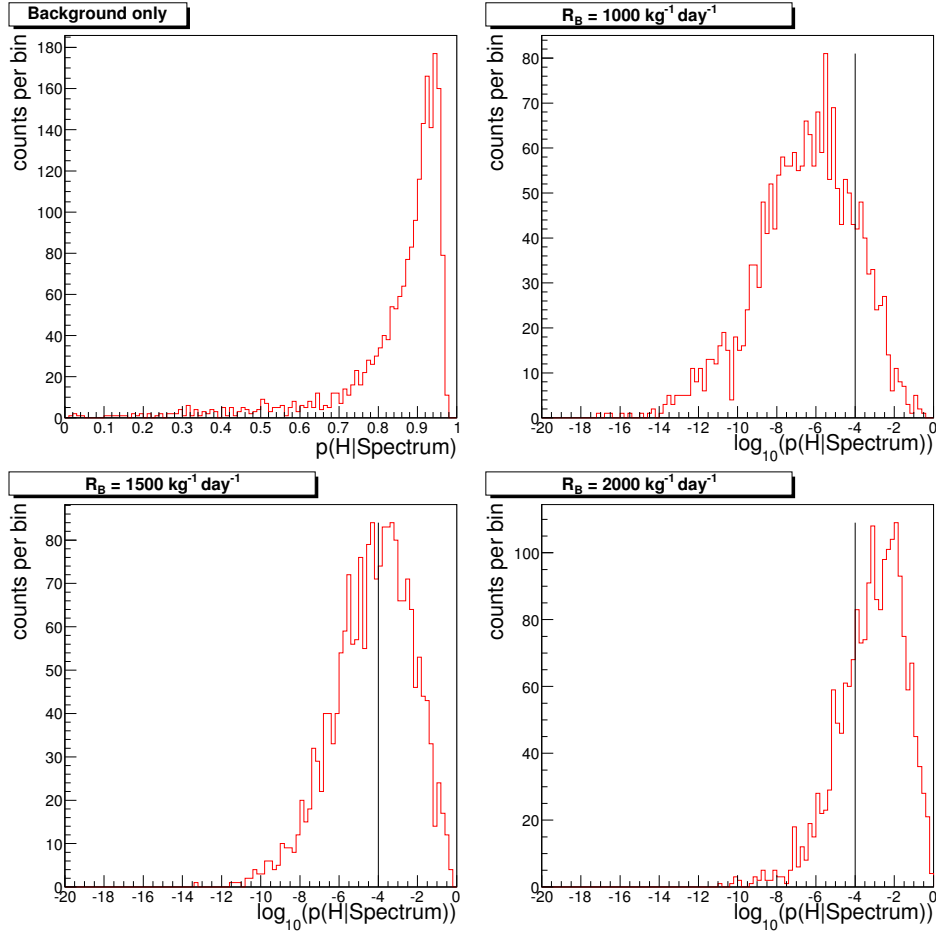


Figure 6.3: Conditional probabilities $p(H|\text{Spectrum})$ for the four ensembles used to study the observation potential of a future experiment for the observation of CNNS. For each ensemble 2000 spectra were simulated. For the spectra containing only background events no false claim of an observation of CNNS occurred. For $\sim 84\%$ of the simulated spectra with a mean background rate of $1000 \text{ kg}^{-1} \text{ day}^{-1}$ an observation could be claimed. For $\sim 52\%$ of the spectra with a mean background rate of $1500 \text{ kg}^{-1} \text{ day}^{-1}$ and for $\sim 28\%$ of the spectra with a mean background rate of $2000 \text{ kg}^{-1} \text{ day}^{-1}$ an observation could be claimed. The black vertical lines represent the limit of 10^{-4} for the probability $p(H|\text{Spectrum})$ to claim an observation of CNNS.

Chapter 7

Investigation of physics beyond the standard model

It has been pointed out in chapter 6 that an observation of CNNS is possible for an experiment located in ~ 40 m distance to a power reactor with a thermal power of ~ 4 GW. In this chapter the investigation of physics beyond the standard model will be discussed. Since processes beyond the standard model are leading to very small variations of the recoil spectra predicted by the standard model, the neutrino count rate has to be increased while the background rate has to be decreased to investigate physics beyond the standard model. Thus, the experiment should be located as close to the reactor core as possible. For the discussions in this chapter a distance of ~ 20 m to a reactor with a power of ~ 4 GW leading to ~ 17 neutrino events per kg-day is assumed. Furthermore, a background rate of ~ 500 events per kg-day is assumed corresponding to a rejection of $\sim 99.99\%$ of muon-induced background events.

7.1 Magnetic moment of the neutrino

The standard model predicts through radiation corrections a nonzero but small magnetic moment for Dirac-neutrinos[76, 77]:

$$\mu_\nu = 3.2 \cdot 10^{-19} \mu_B \left(\frac{m_\nu}{1 \text{ eV}} \right) \quad (7.1)$$

$$\mu_B = \frac{e\hbar}{2m_e} = 5.788 \text{ MeV T}^{-1}, \quad (7.2)$$

where μ_B is the Bohr magneton, m_e is the electron mass and m_ν is the neutrino mass. The current measured upper limit for the magnetic moment is $3.2 \cdot 10^{-11} \mu_B$ (90% confidence level)[78, 77].

The experiment for the observation of CNNS described in the present work (see section 2.5, section 5.2 and figure 5.8) could also be used to measure a magnetic moment. The cross sections of both CNNS and neutrino electron scattering are enhanced by a magnetic moment[76, 77]. However, for CNNS the enhancement of the cross section affects only very small recoil energies $\ll 0.5$ keV. Since the low-temperature detectors used to observe CNNS can not discriminate between nuclear and electron recoils, they can also detect neutrino electron scattering. Due to the small recoil energies generated by CNNS the neutrino signal is dominated by neutrino electron scattering for recoil energies above ~ 4 keV. The cross section $\sigma_{\nu-e}$ for neutrino electron scattering with a magnetic moment[76] is given by:

$$\begin{aligned} \frac{d\sigma_{\nu-e}}{dE_{rec}} &= \frac{G_F^2 m_e}{2\pi} \left[(g_V + g_A)^2 + (g_V - g_A)^2 \left(1 - \frac{E_{rec}}{E_\nu}\right)^2 \right. \\ &\quad \left. + (g_A^2 - g_V^2) \frac{m_e E_{rec}}{E_\nu^2} \right] \\ &\quad + \frac{\pi\alpha^2}{m_e} \left(\frac{\mu_\nu}{\mu_B}\right)^2 \left(\frac{1}{E_{rec}} - \frac{1}{E_\nu}\right), \end{aligned} \quad (7.3)$$

where G_F is the Fermi constant, m_e is the electron mass, E_{rec} is the recoil energy of the electron, E_ν is the neutrino energy, α is the fine structure constant, and

$$g_V = \begin{cases} 2 \sin^2 \theta_W + \frac{1}{2} & \text{for } \nu_e \\ 2 \sin^2 \theta_W - \frac{1}{2} & \text{for } \nu_\mu, \nu_\tau \end{cases} \quad (7.4)$$

$$g_A = \begin{cases} \frac{1}{2} & \text{for } \nu_e \\ -\frac{1}{2} & \text{for } \nu_\mu, \nu_\tau \end{cases}, \quad (7.5)$$

where θ_W is the Weinberg angle. For antineutrinos g_A has to be substituted by $g_A \rightarrow -g_A$. Due to the small distance between the reactor core and the experiment (~ 20 m) oscillations between flavor neutrinos can be neglected[79]. Thus, for the calculation of the neutrino spectra shown in figure 7.1 only $\bar{\nu}_e$ were taken into account. Figure 7.1 exhibits two neutrino spectra and a background spectrum for comparison. One neutrino spectrum was calculated without a magnetic moment ($\mu_\nu = 0$), for the other neutrino spectrum the current upper limit for the magnetic moment ($\mu_\nu = 3.2 \cdot 10^{-11} \mu_B$ [78, 77]) was used. For the background spectrum a rate of $R_B = 2500 \text{ kg}^{-1} \text{ day}^{-1}$ for the energy region between 0.5 and 20 keV was used. This rate corresponds to $500 \text{ kg}^{-1} \text{ day}^{-1}$ for the energy region between 0.5 and 4 keV used for the observation of CNNS (see chapter 6).

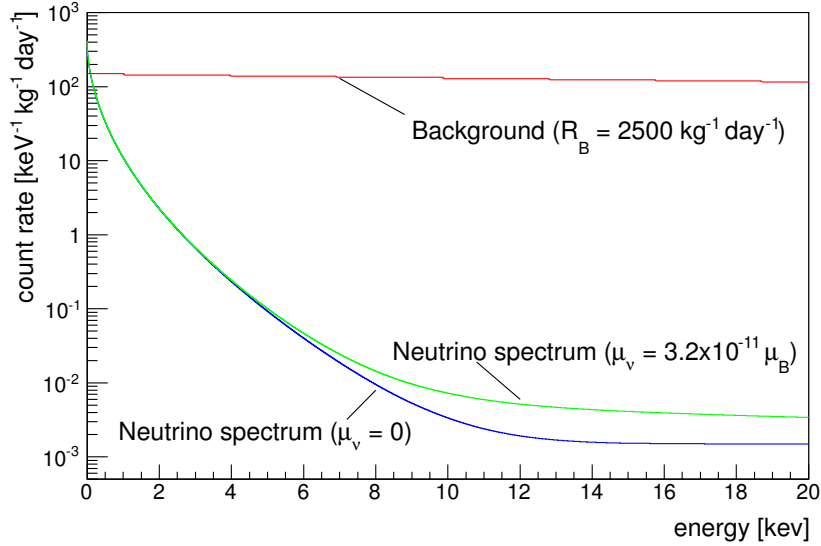


Figure 7.1: Neutrino spectra with and without a magnetic moment of the neutrino. The neutrino spectra are the sum of the recoil-energy spectra for CNNS and neutrino-electron scattering. For the magnetic moment the current upper limit of $3.2 \cdot 10^{-11} \mu_B$ (90% confidence level)[78, 77] was used. For comparison also the expected background spectrum is shown. The background rate $R_B = 2500 \text{ kg}^{-1} \text{ day}^{-1}$ in the energy region between 0.5 and 20 keV corresponds to a background rate of $500 \text{ kg}^{-1} \text{ day}^{-1}$ in the region between 0.5 and 4 keV used for the observation of CNNS (see chapter 6).

To study the sensitivity of a future CNNS experiment for a magnetic moment of the neutrino 4000 spectra were simulated similarly to the spectra used to estimate the observation potential of a CNNS experiment (see section 6.2). For the distribution of the background events an exponential (see section 6.2 and equation (6.11)) was used. The neutrino events are distributed following the neutrino spectrum without a magnetic moment (blue line in figure 7.1). For the neutrino rate R_S it was assumed that the experiment is located at a distance of 20 m from a reactor core with a thermal power of $\sim 4 \text{ GW}$. The resulting mean value for the neutrino rate is $R_S \approx 13.56 \text{ kg}^{-1} \text{ day}^{-1}$ (CNNS and neutrino-electron scattering) for the energy region between 0.5 and 20 keV. Furthermore an exposure of 20 kg-years corresponding to a measuring time of 5 years was assumed.

A model containing background, neutrino signal and a magnetic moment was fitted to all 4000 simulated spectra using the Bayesian analysis described in chapter 6. For the prior probability $p_0(R_B)$ of the background rate a normal distribution with a mean of $2500 \text{ kg}^{-1} \text{ day}^{-1}$ and a width of 1% was

used:

$$p_0(R_B) = \frac{1}{0.01R_B\sqrt{2\pi}} e^{-\frac{1}{2}\left(\frac{2500 \text{ kg}^{-1} \text{ day}^{-1} - R_B}{0.01R_B}\right)^2}. \quad (7.6)$$

For the prior probability $p_0(R_S)$ for the neutrino rate without magnetic moment a normal distribution with a mean of $13.56 \text{ kg}^{-1} \text{ day}^{-1}$ and a width of 10% was used:

$$p_0(R_S) = \frac{1}{0.1R_S\sqrt{2\pi}} e^{-\frac{1}{2}\left(\frac{13.56 \text{ kg}^{-1} \text{ day}^{-1} - R_S}{0.1R_S}\right)^2}. \quad (7.7)$$

The prior probability $p_0(R_{mag})$ for the rate R_{mag} caused by a magnetic moment was chosen to be constant:

$$p_0(R_{mag}) = \begin{cases} \frac{1}{R_{mag}^{max}} & \text{for } R_{mag} \leq R_{mag}^{max} \\ 0 & \text{for } R_{mag} > R_{mag}^{max} \end{cases}, \quad (7.8)$$

where R_{mag}^{max} is the maximal expected value for the rate R_{mag} . To save computation time the value of R_{mag}^{max} has to be as small as possible. However, it should be large enough so that the marginalized probability $p(R_{mag}|\text{Spectrum})$ vanishes for R_{mag}^{max} . Thus, R_{mag}^{max} was set to $\sim 5.6 \text{ kg}^{-1} \text{ day}^{-1}$ corresponding to a magnetic moment of $\sim 2 \cdot 10^{-10} \mu_B$ (see figure 7.2).

To obtain an upper limit for the magnetic moment from the fit of the model to a simulated spectrum the marginalized probability density function $p(R_{mag}|\text{Spectrum})$ has to be calculated:

$$p(R_{mag}|\text{Spectrum}) = \int_{R_B} dR_B \int_{R_S} dR_S p(R_B, R_S, R_{mag}|\text{Spectrum}), \quad (7.9)$$

where $p(R_B, R_S, R_{mag}|\text{Spectrum})$ is given by Bayes' theorem (see chapter 6).

The upper limit $R_{mag,90}$ for the count rate caused by a magnetic moment is calculated by integrating the probability density function $p(R_{mag}|\text{Spectrum})$:

$$\int_0^{R_{mag,90}} p(R_{mag}|\text{Spectrum}) dR_{mag} = 0.90. \quad (7.10)$$

Thus, the probability that the count rate R_{mag} is smaller than the upper limit $R_{mag,90}$ is 90%. The left panel of figure 7.2 depicts the marginalized probability density function $p(R_{mag}|\text{Spectrum})$ for one simulated spectrum. For this spectrum the upper limit $R_{mag,90} \approx 1.36 \text{ kg}^{-1} \text{ day}^{-1}$ (90% confidence level).

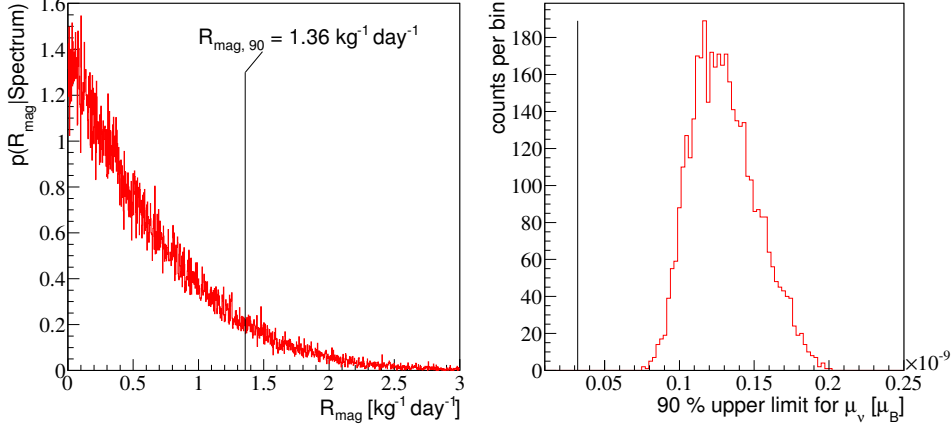


Figure 7.2: *Left panel:* Marginalized probability density function $p(R_{mag}|\text{Spectrum})$ for one simulated spectrum. The upper limit for the count rate caused by a magnetic moment is $R_{mag,90} \approx 1.36 \text{ kg}^{-1} \text{ day}^{-1}$ leading to an upper limit for the magnetic moment of $\mu_\nu < 1.1 \cdot 10^{-10} \mu_B$ (90 % confidence level). For comparison, the current best limit is $\mu_\nu < 3.2 \cdot 10^{-11} \mu_B$ [78, 77].

Right panel: Upper limits on the magnetic moment for the 4000 simulated spectra. For all simulated spectra the resulting upper limit is well above the current experimental limit [78, 77] represented by the vertical black line.

The upper limit for the magnetic moment μ_ν can be calculated using the upper limit $R_{mag,90} \approx 1.36 \text{ kg}^{-1} \text{ day}^{-1}$:

$$\mu_\nu < \sqrt{\frac{R_{mag,90}}{R_0}} \cdot 10^{-10} \mu_B \quad (7.11)$$

$$R_0 \propto \int_{0.5 \text{ keV}}^{\infty} dE_{rec} \int_{\sqrt{0.5 E_{rec} M}}^{\infty} dE_\nu \Phi(E_\nu) \frac{d\sigma_{mag}}{dE_{rec}} \quad (7.12)$$

$$\frac{d\sigma_{mag}}{dE_{rec}} = \frac{\pi\alpha^2}{m_e} \left(\frac{10^{-10} \mu_B}{\mu_B} \right)^2 \left(\frac{1}{E_{rec}} - \frac{1}{E_\nu} \right), \quad (7.13)$$

where $R_0 = 1.322 \text{ kg}^{-1} \text{ day}^{-1}$ is the additional count rate caused by a magnetic moment of $10^{-10} \mu_B$. The upper limit on the magnetic moment for $R_{mag,90} \approx 1.36 \text{ kg}^{-1} \text{ day}^{-1}$, shown in the left panel of figure 7.2, is:

$$\mu_\nu < 1.1 \cdot 10^{-10} \mu_B (90 \% \text{ confidence level}), \quad (7.14)$$

which is larger than the current upper limit of $3.2 \cdot 10^{-11}$ [78, 77] by a factor of ~ 3 .

The calculations of $R_{mag,90}$ and the upper limit on the magnetic moment were performed for all 4000 simulated spectra. The results of these calculations are shown in the right panel of figure 7.2. For all 4000 simulated spectra

the upper limits are well above the current experimental upper limit[78, 77] which is represented by the black line.

Thus, it is not possible to improve the limit on the magnetic moment of the neutrino with an exposure of ~ 20 kg-years. To increase the exposure at least target masses larger by a factor of ~ 10 are needed. However, the technical difficulties to reach such target masses are enormous (see section 2.5).

7.2 Search for sterile neutrinos

A recent recalculation of the reactor anti-neutrino spectra resulted in an increase of the mean neutrino flux by $\sim 3\%$ [80]. Thus, the neutrino flux measured by several previous short base-line experiments is too small by $\sim 3\%$ [80]. This so-called reactor anomaly could be explained by an oscillation of anti-electron neutrinos into sterile neutrinos¹.

Since CNNS is a neutral current process, it is independent of the neutrino flavor. Thus, an experiment aiming at the observation of CNNS could also measure the neutrino rate independently of the uncertainties of the oscillations between flavor neutrinos. For the observation of sterile neutrinos the neutrino rate has to be measured to a precision better than $\sim 1\%$. Since it is very difficult to measure the thermal power of a reactor with such a precision, the neutrino rate has to be determined by the comparison of two experiments located at different distances from the reactor. The oscillation length of flavor neutrinos into sterile neutrinos is assumed to be $\mathcal{O}(\text{m})$ [80]. Thus, to study the potential of a CNNS experiment for an observation of sterile neutrinos two ensembles with 200 spectra each were simulated. For one ensemble a distance of 20 m to a reactor core was assumed. For the other ensemble a distance of 22.5 m and a reduction of the neutrino flux by 2% due to an oscillation into sterile neutrinos in addition to the geometric effect (factor ~ 1.23) was assumed. For both ensembles a background rate of $500 \text{ kg}^{-1} \text{ day}^{-1}$ in the energy region between 0.5 and 4 keV and an exposure of 100 kg-days were used. With those mean values the spectra were simulated similarly to the simulations described in section 6.2.

Each simulated spectrum was fitted with a model containing background and CNNS signal. The neutrino rate R_S obtained by this fit can be used to search for an oscillation into sterile neutrinos. The difference in the neutrino rates at both locations is a measure for the amplitude of the oscillation. The

¹Sterile neutrinos can not participate in any interaction of the standard model (strong, electromagnetic, or weak interaction). Thus, they can only interact gravitationally due to their mass.

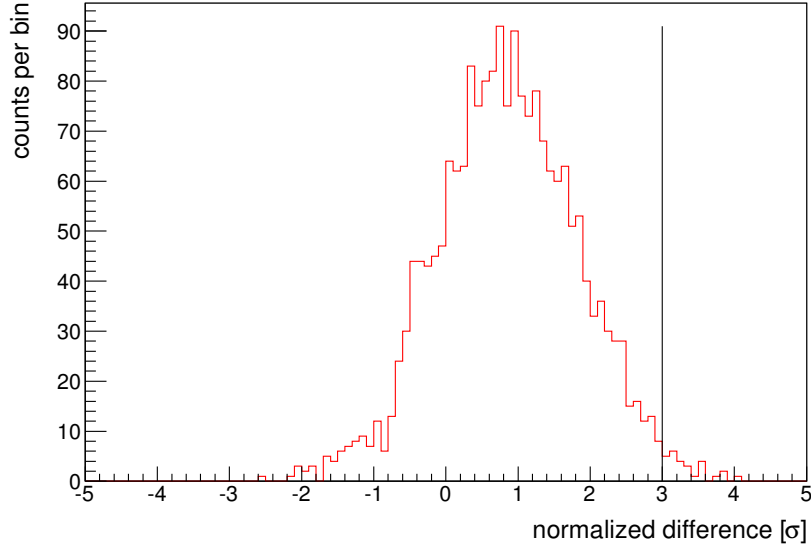


Figure 7.3: Normalized differences between the neutrino rates of the locations in 20 and 22.5 m distance. The differences were divided by their errors. For a few ($\sim 1\%$) spectra the difference is larger than a $3\text{-}\sigma$ effect. The vertical black line represents the $3\text{-}\sigma$ level.

neutrino flux at a location at a distance of 22.5 m is smaller by a factor of ~ 1.23 compared to a location at a distance of 20 m. The smaller neutrino flux has to be taken into account to calculate the difference in the neutrino rate at both locations. Figure 7.3 exhibits the differences of all simulated spectra divided by their errors (normalized differences). Only for a few ($\sim 1\%$) spectra this normalized difference is larger than the $3\text{-}\sigma$ level represented by the black line. The probability that the normalized difference is that large is $\lesssim 0.1\%$ without an oscillation into sterile neutrinos. However, the difference is still not large enough to claim an evidence of sterile neutrinos.

The investigation of new physics beyond the standard model using the experiment described in the present work is not promising. The potential limit for a magnetic moment of the neutrino is larger than the current limit by a factor of ~ 3 . With a probability of $\sim 1\%$ a hint for sterile neutrinos could be found to explain the reactor anomaly. To improve the sensitivity on new physics beyond the standard model the target mass has to be increased at least by a factor of ~ 10 . Such an increase of the target mass leads to immense technical difficulties (see section 2.5).

However, there are also other extensions of the standard model leading to enhancements of the cross sections for CNNS and neutrino-electron scattering

by a few orders of magnitude^[77]². It is promising to test such models by an experiment aiming at the observation of CNNS.

²In [77] new light gauge bosons are discussed. The so-called dark photon is a gauge boson which is coupled strongly to sterile neutrinos but very weakly to standard model particles. If such a particle exists, the cross sections for CNNS and neutrino-electron scattering could be enhanced by several orders of magnitudes for small recoil energies.

Chapter 8

Solar and atmospheric neutrinos as background for direct dark-matter searches

8.1 Direct dark-matter searches

The kinetics of galaxies and galaxy clusters can not be explained by baryonic matter alone[81, 82, 83] but by the existence of non-baryonic dark matter. The precision measurement of the temperature fluctuations of the cosmic microwave background revealed a dark matter content of $\sim 24\%$ of the total energy content of the universe[84, 85].

One candidate for dark matter is a Weakly Interacting Massive Particle (WIMP)[81, 82]. There are several candidates for WIMPs like the lightest supersymmetric particle[81, 82] or the lightest extra-dimensional Kaluza-Klein particle[81]. All these candidates are massive particles (mass $\gtrsim \mathcal{O}(10 \text{ GeV})$) and are expected to exhibit weak interaction with baryonic matter.

Direct dark-matter searches are based on the scattering of WIMPs off nuclei. The best choice of the target material depends on the WIMP mass and the nature of the interaction between WIMPs and nuclei. In the simplest model the interaction is spin-independent and elastic. The recoil energy spectrum of the target nuclei is, for this simple model, given by[4]:

$$\frac{dR(E_{rec})}{dE_{rec}} = \frac{c_1 N_A M_N \rho_D}{2\sqrt{\pi} \mu_1^2} \sigma_{WN} |F(q)|^2 v_0 \frac{A^2}{E_0} e^{-\frac{c_2 E_{rec}}{E_0 r}} [\text{kg}^{-1} \text{s}^{-1} \text{keV}^{-1}] \quad (8.1)$$

$$\mu_1 = \frac{M_W M_N}{M_W + M_N} \quad (8.2)$$

$$r = 4 \frac{M_W M_T}{(M_W + M_T)^2}, \quad (8.3)$$

where $c_1 = 0.751$ and $c_2 = 0.561$ [4] are dimensionless constants describing the annular modulation of the WIMP flux, $N_A = 6.022 \cdot 10^{26} \text{ kg}^{-1}$ [6] is Avogadro's number, $M_N = 931.5 \text{ MeV}$ [6] is the average mass of one nucleon, $\rho_D = 0.3 \frac{\text{GeV}}{\text{cm}^3}$ [86] is the local dark-matter density, μ_1 is the reduced mass for $A = 1$, σ_{WN} is the WIMP-nucleon cross section, $|F(q)|$ is the Helm form factor (see equation (1.4)[5]), $v_0 \approx 230 \frac{\text{km}}{\text{s}}$ [4] is the velocity of the earth relative to the WIMPs, A is the mass number of the target nucleus, $E_0 = \frac{1}{2}M_W(\frac{v_0}{c})^2$ is the kinetic energy of the WIMPs, r is a dimensionless kinematic factor, M_W is the WIMP mass, $M_T = AM_N$ is the mass of the target nucleus.

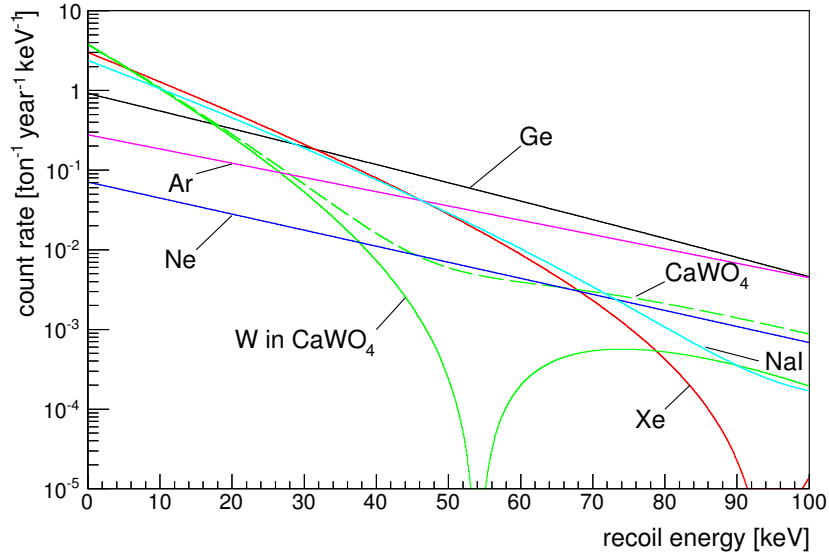


Figure 8.1: Recoil-energy spectra of $M_W = 60 \text{ GeV}$ WIMPs for different materials. For the calculation of these spectra a WIMP-nucleon cross section σ_{WN} of $1.0 \cdot 10^{-46} \text{ cm}^2$ was used.

Figure 8.1 depicts the recoil-energy spectra for different target materials used for direct dark-matter searches. For the calculations of these spectra a WIMP mass $M_W = 60 \text{ GeV}$ and a WIMP-nucleon cross section $\sigma_{WN} = 1.0 \cdot 10^{-46} \text{ cm}^2$ was used.

For calcium tungstate (CaWO_4) used in the CRESST experiment[34, 38] two different spectra are shown in figure 8.1. The solid line represents only the tungsten recoils and the dashed line represents the sum of all nuclei.

8.2 Neutrinos as background source

The main part of background events is due to cosmic muons and natural radioactivity. Both interact mainly with the electrons of the target mater-

ial. However, the WIMPs are mainly interacting with the nuclei. As most experiments for direct dark-matter searches are able to discriminate between electron-recoil and nuclear-recoil events they can reject most of the background events. The remaining background is due to neutrons caused by cosmic muons. These neutrons can be shielded, if they are produced in the surrounding rock. However, if they are produced inside the shielding, they can only be rejected by an active muon veto or via multiple scattering events in several detectors.

Up to now, most direct dark-matter searches recorded only few background events, e.g., 2 events were observed in 194.1 kg-days[29] with the CDMS experiment. However, since CNNS is producing the same signature as WIMP-scatterings also neutrinos could be a background source[2, 87, 12, 13, 14, 15, 16] for the ton-scale target masses of the next-generation direct dark-matter searches.

8.2.1 Solar neutrinos

The strongest natural neutrino source is the sun. Thus, solar neutrinos (see section 1.2.1) are the first candidate for a background source for direct dark-matter searches.

The recoil-energy spectra for different target materials used for direct dark-matter searches shown in figure 8.2 are calculated according to equation (1.10). The kinks in the recoil-energy spectra of calcium tungstate (CaWO_4) and sodium iodide (NaI) originate from the masses of the different nuclei. The maximum recoil energy for a neutrino source depends on the mass of the target nucleus. A larger mass leads to a smaller recoil energy. Thus, above the maximum recoil energy for a heavy nucleus like tungsten or iodine, only the lighter nuclei can contribute to the combined spectrum.

In figure 8.3 the count rates above an energy threshold E_{th} are shown for materials used in direct dark-matter searches. For small energy thresholds the count rates for solar neutrinos are relatively high ($\sim 10^3$ events for an energy threshold of ~ 0.1 keV). However, the energy thresholds of direct dark-matter searches are ~ 10 keV leading to a very small count rate for solar neutrinos.

The best sensitivity for direct dark-matter searches is achieved, if no background events are observed in the recoil-energy region where potential WIMP events are expected. In table 8.1 the “optimal” recoil-energy regions for direct dark-matter searches are listed: For an exposure of one ton-year ~ 0.1 solar neutrino events are expected in these regions. An expected count

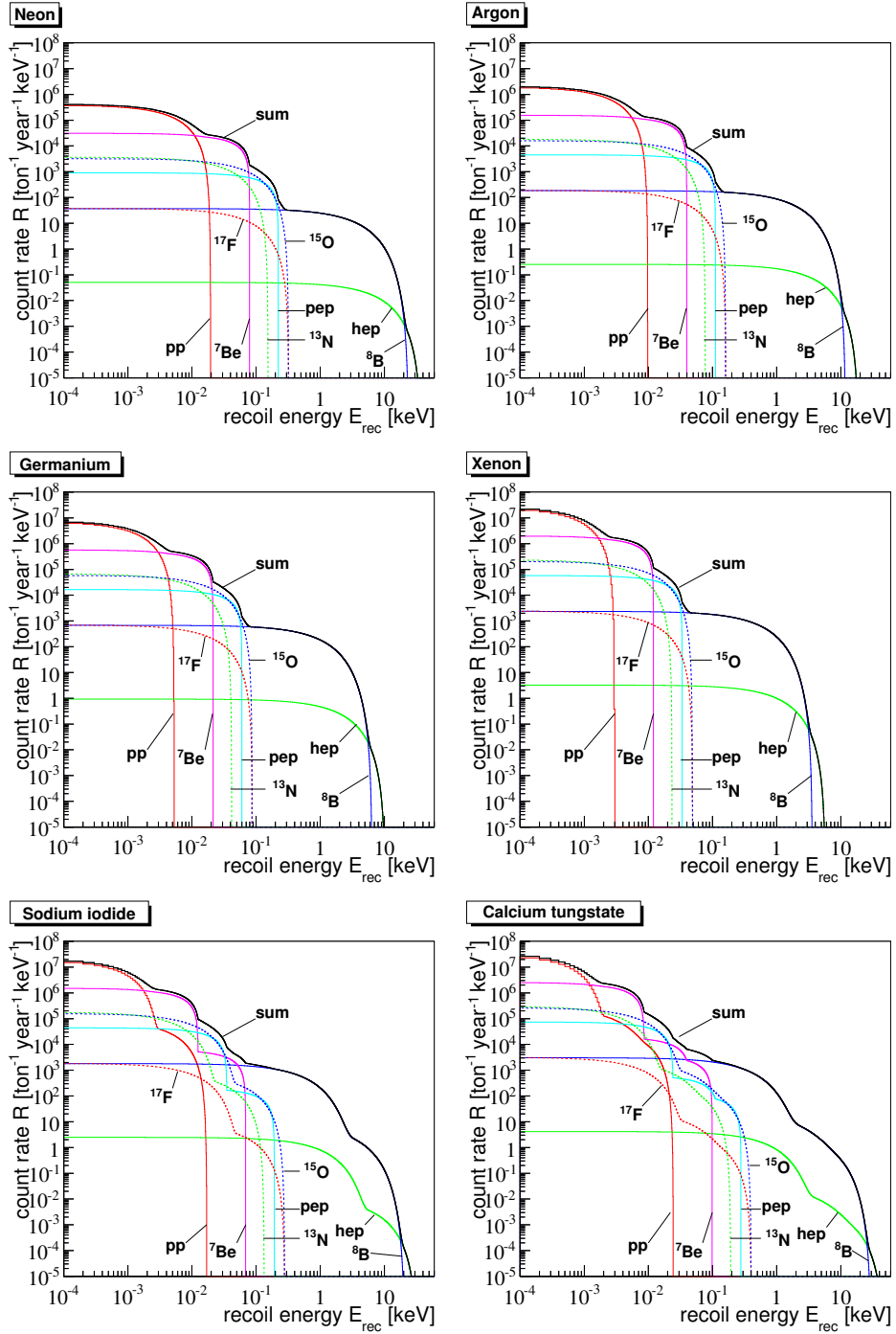


Figure 8.2: Recoil spectra of solar neutrinos for different target materials used in direct dark-matter searches.

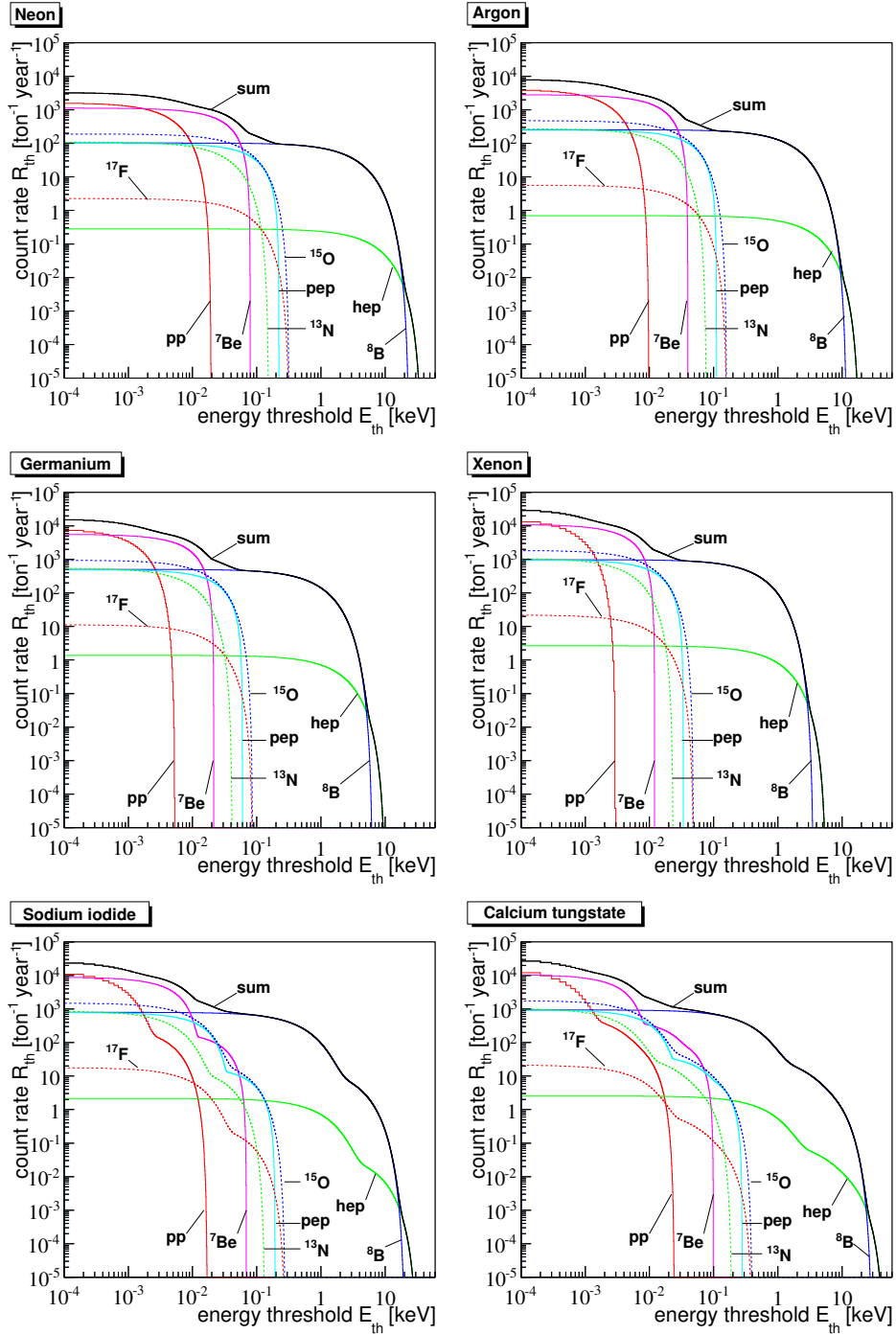


Figure 8.3: Count rates above threshold of solar neutrinos for different target materials. These count rates are the integrals of the recoil-energy spectra shown in figure 8.2 (see also section 1.2).

Material	optimal region	current region
Neon (Ne)	15.93 - 100 keV	-
Argon (Ar)	8.62 - 100 keV	30 - 100 keV
Germanium (Ge)	4.91 - 100 keV	10 - 100 keV
Xenon (Xe)	2.89 - 100 keV	8.4 - 100 keV
Sodium iodide (NaI)	11.48 - 100 keV	2 - 6 keV
Calcium tungstate (CaWO ₄)	16.31 - 100 keV	12 - 40 keV
W in CaWO ₄	2.05 - 100 keV	12 - 40 keV

Table 8.1: Optimal and current recoil-energy regions for direct dark-matter searches. The lower threshold of the optimal search regions given in the second column is chosen such that 0.1 solar neutrino events are expected in that region for an exposure of one ton-year. The upper threshold is not critical since the recoil-spectra are very steep (see figures 8.2 and 8.3). In the third column the current recoil-energy regions are listed for ArDM[41] (Ar), CDMS[29] (Ge), XENON100[36] (Xe), DAMA/ LIBRA[88] (NaI), and CRESST[38] (CaWO₄).

rate of 0.1 events per ton-year corresponds to a probability¹ for no neutrino events of $\sim 90\%$. Due to the steep recoil spectra and the low count rates for larger recoil energies (see figures 8.2 and 8.3) the expected count rate depends mainly on the lower threshold of the recoil-energy regions.

For comparison also the current recoil-energy regions of several direct dark-matter searches are listed in table 8.1. The different target materials and the corresponding experiments will be discussed in more detail in the following.

Neon (Ne)

Due to its small mass neon is a good target material for light WIMP masses ($M_W \lesssim 10$ GeV). Furthermore, there are no long-lived radioactive isotopes of Ne and also radioactive isotopes of other rare gases can efficiently be removed[42, 89]. Since there is currently no experiment using Ne as target material the optimal recoil-energy threshold of 15.93 keV (see table 8.1) can not be compared with the energy threshold of an existing experiment. However, there are plans to use Ne in the future[42, 90].

¹Poisson distribution: $p_{\lambda=0.1}(k=0) = \frac{\lambda^k}{k!} e^{-\lambda} \approx 0.9$, where λ is the mean number and k is the observed number of events.

Argon (Ar)

Although argon has the long-lived radioactive isotope ^{39}Ar the handling of argon has less technical difficulties than for Ne. Thus, argon is used as a target material, e.g., for the Argon Dark Matter experiment (ArDM)[41]. The recoil-energy threshold of ArDM ($\sim 30\text{ keV}$) is well above the optimal threshold of 8.62 keV and, thus, solar neutrinos are no background source for the ArDM experiment.

Germanium (Ge)

Due to the high radiopurity and the well known properties germanium is used in several direct dark-matter searches with different read out techniques[29, 39, 43]. The optimal recoil-energy threshold of 4.91 keV is also well below the lowest threshold achieved in direct dark-matter searches, i.e., 10 keV in the Super Cryogenic Dark-Matter search (SuperCDMS)[35, 91, 29]. Thus, for current thresholds solar neutrinos are no background source, even for ton-scale experiments.

Xenon (Xe)

The experiment with the presently best sensitivity for a WIMP mass of $\sim 60\text{ GeV}$ is XENON100[36] using liquid xenon as target material. The recoil-energy threshold of 8.4 keV [36] is also well above the optimal threshold of 2.89 keV . Thus, solar neutrinos are no serious background source for xenon as target material.

Sodium iodide (NaI)

Sodium iodide is used by the DAMA/ LIBRA[88] experiment. However, this experiment is following a different approach for direct dark-matter search. Due to the rotation of the earth around the sun the WIMP flux is modulated on a yearly basis[88, 92]. The advantage of this model-independent approach is that practically all background sources either show no modulation or a modulation with a different phase or frequency[88]. Thus, also solar neutrino events are no problem due to the different phase of the yearly modulation of the solar neutrino flux, although the currently used energy region in DAMA/ LIBRA is well below the optimal threshold[88]. However, the observation of the modulation of a WIMP signal requires large exposures.

The CoGeNT[43] experiment is using a similar approach with germanium as target material.

Calcium tungstate (CaWO_4)

Calcium tungstate is used as target material for the experiment Cryogenic Rare Event Search with Superconducting Thermometers (CRESST)[34, 38]. CaWO_4 is a scintillating insulator and has the potential to reject neutron background due to the different mass numbers of the three nuclei forming CaWO_4 . While heavy WIMPs (mass $M_W \gtrsim 20 \text{ GeV}$) interact mainly with tungsten due to the A^2 dependence of the WIMP-nucleon cross section σ_{WN} (see equation (8.1)), neutrons are preferably scattering off oxygen[93]. Furthermore for tungsten recoils (i.e. the incident particle scatters off tungsten) less scintillation light is produced than for calcium and oxygen recoils[93]. Thus, measuring the amount of scintillation light produced by the energy deposition it is possible to discriminate tungsten recoils against calcium and oxygen recoils.

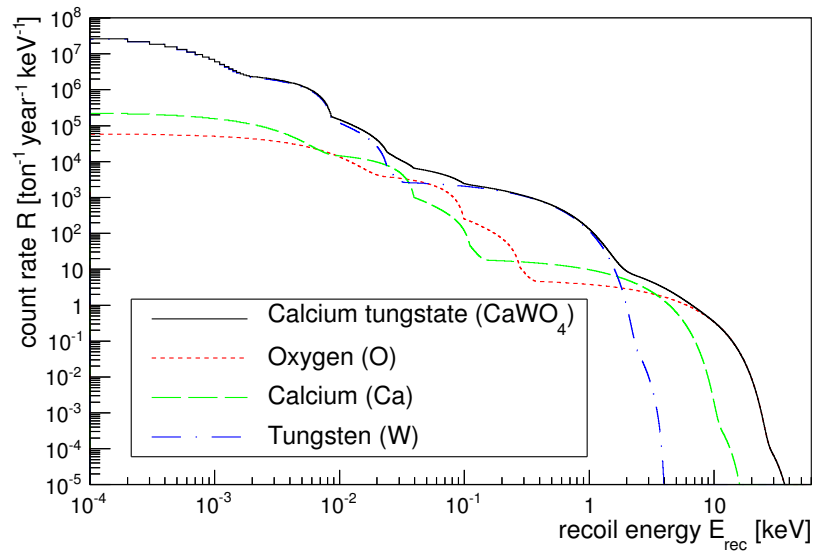


Figure 8.4: Recoil spectra of solar neutrinos for the different constituents of CaWO_4 . If the discrimination between tungsten recoils and calcium and oxygen recoils is possible, solar neutrinos are no serious background above an energy threshold of $\sim 2 \text{ keV}$.

The recoil spectra of solar neutrinos for tungsten, calcium, and oxygen are shown in figure 8.4. Above a recoil energy of $\sim 2 \text{ keV}$ solar neutrinos are scattering mainly off calcium and oxygen. With a working discrimination between tungsten recoils and calcium and oxygen recoils the optimal energy threshold is 2.05 keV , which is also well below the current energy threshold of 12 keV for CRESST[38].

However, if the discrimination between tungsten and the two other constituents is not possible in the region between 12 and 40 keV, solar neutrinos will be a serious background source ($\sim 1 \text{ ton}^{-1} \text{ year}^{-1}$) for a ton-scale experiment using CaWO_4 .

8.2.2 Atmospheric neutrinos

Due to the small recoil energies solar neutrinos are no background source for the most direct dark-matter searches. Although atmospheric neutrinos have a smaller flux than solar neutrinos their energies can be much higher[94].

The recoil-energy spectra of atmospheric neutrinos shown in figure 8.5 are flat up to recoil energies of $\sim 10 \text{ keV}$. Thus, atmospheric neutrinos can not be rejected by a proper choice of the recoil-energy threshold. These recoil spectra were calculated using equation (1.10). Since the form factor becomes very small for high neutrino energies only atmospheric neutrinos with energies $\lesssim 100 \text{ MeV}$ were taken into account for the calculation of the recoil spectra shown in figure 8.5. The flux of atmospheric neutrinos with energies below 100 MeV was taken from [94]. The uncertainty of this flux is $\sim 20\%$. Since CNNS is a neutral-current interaction the fluxes for all neutrino flavors given in [94] were summed and then fitted by

$$\Phi(E_\nu) = e^{a_0 + a_1 \ln(E_\nu) + a_2 \ln(E_\nu)^2 + a_3 \ln(E_\nu)^3 + a_4 \ln(E_\nu)^4}, \quad (8.4)$$

where the values of the parameters a_i are listed in table 8.2.

a_0	$-5.34234 \cdot 10^2$
a_1	$1.71949 \cdot 10^2$
a_2	$-2.10980 \cdot 10^1$
a_3	1.15426
a_4	$-2.39567 \cdot 10^{-2}$

Table 8.2: Fit parameters a_i used in equation (8.4).

In figure 8.6 the count rates above a recoil-energy threshold E_{th} are shown for different target materials. For the present thresholds as well as for the thresholds of the optimal search regions listed in table 8.1 atmospheric neutrinos are leading to $\sim 10^{-2}$ events per ton-year. Thus, atmospheric neutrinos are only a serious background source for larger exposures of about 5 to 10 ton-years.

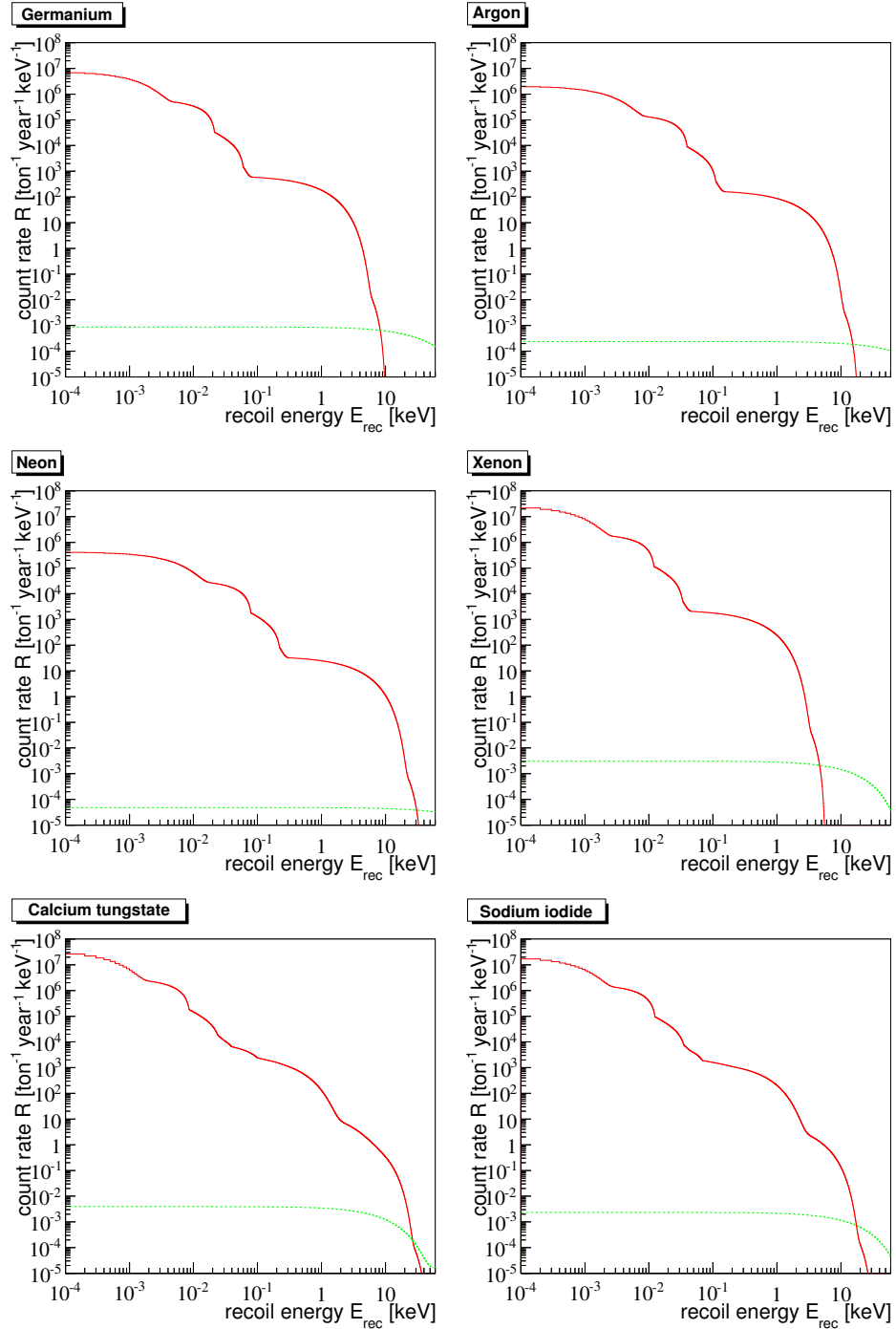


Figure 8.5: Recoil-energy spectra of atmospheric (green dotted lines) and solar neutrinos (red solid lines) for different target materials used for direct dark-matter searches.

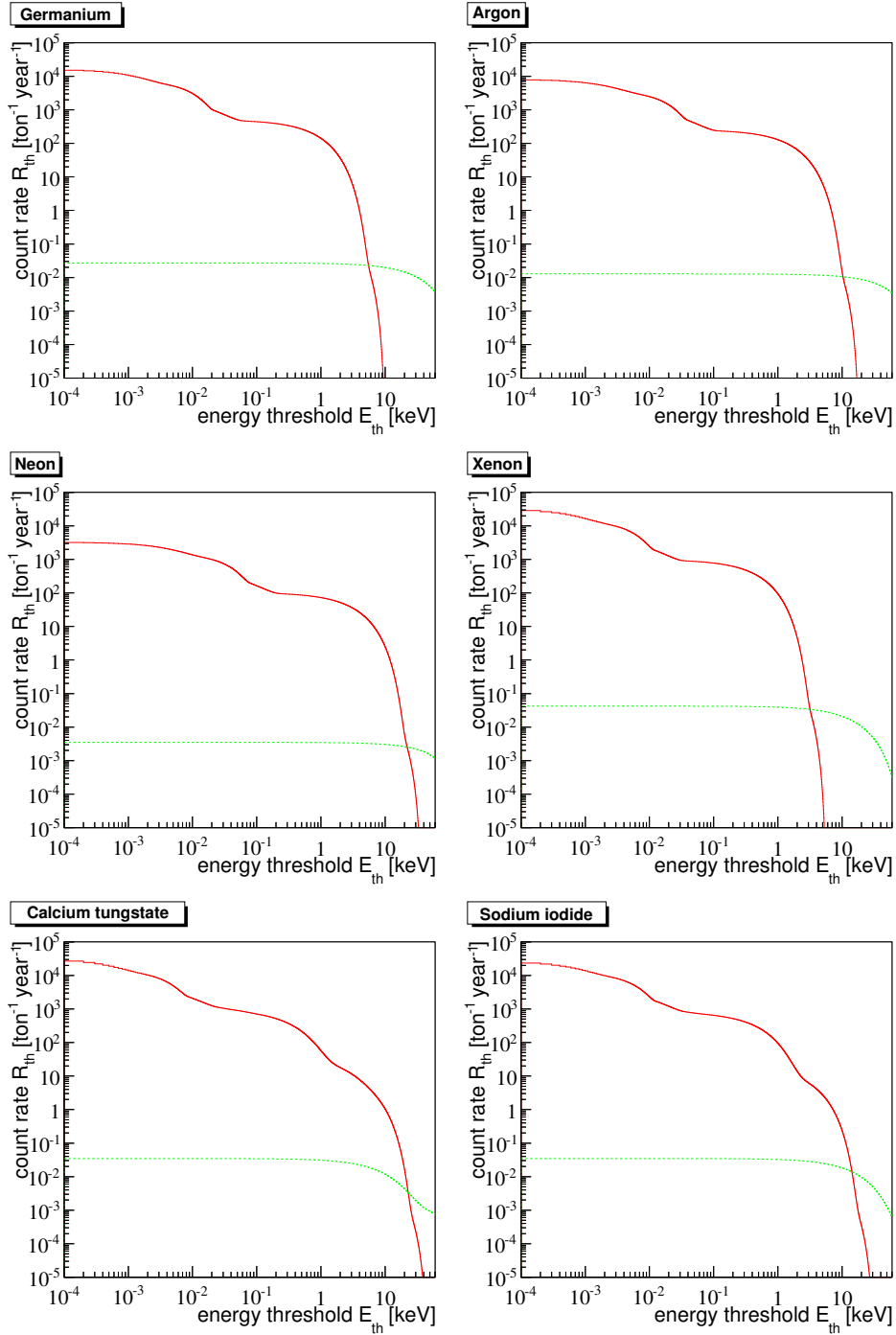


Figure 8.6: Count rates above a recoil-energy threshold E_{th} for different target materials used in direct dark-matter searches. These count rates are the integrals of the recoil-energy spectra shown in figure 8.5 (see also section 1.2).

8.3 Limitations for future experiments

Solar neutrinos are no serious background source for direct dark-matter searches if the energy threshold is chosen properly, see table 8.1. The probability to observe one or more background events in these optimal regions is $\sim 10\%$. Due to smaller count rates atmospheric neutrinos are becoming important for larger exposures of about 5 to 10 ton-years.

If an experiment observes no events inside the region for direct dark-matter search, it can exclude part of the parameter space, i.e., part of the plane spanned by WIMP mass M_W and cross section σ_{WN} for WIMP-nucleon scattering. The number of events inside an energy region is Poisson distributed:

$$p_\lambda(k) = \frac{\lambda^k}{k!} e^{-\lambda}, \quad (8.5)$$

where λ is the mean number and k is the observed number of events. If no events are observed, all values of $\lambda > \lambda_{CL}$ can be excluded at a confidence level CL . The limit λ_{CL} is given by the requirement that the probability to observe no events is $(1 - CL)$:

$$p_{\lambda_{CL}}(k=0) = e^{-\lambda_{CL}} = 1 - CL \quad (8.6)$$

$$\Rightarrow \lambda_{CL} = -\ln(1 - CL) \stackrel{CL=0.9}{\approx} 2.3. \quad (8.7)$$

All parameter sets (M_W, σ_{WN}) leading to an expected number of WIMP events higher than λ_{CL} can be excluded on a confidence level CL . The expected number λ of WIMP events for an exposure T_0 is given by the integral over the recoil spectrum (equation (8.1)):

$$\lambda = \int_0^\infty dE_{rec} \frac{dR(E_{rec})}{dE_{rec}} \quad (8.8)$$

$$= T_0 \int_0^\infty dE_{rec} \frac{c_1 N_A M_N \rho_D}{2\sqrt{\pi} \mu_1^2} \sigma_{WN} |F(q)|^2 v_0 \frac{A^2}{E_0} e^{-\frac{c_2 E_{rec}}{E_0 r}}. \quad (8.9)$$

The WIMP-nucleon cross section σ_{WN} is independent of the recoil energy. Thus, the expected number λ of WIMP events can be written as:

$$\lambda = \sigma_{WN} I(M_W) T_0 \quad (8.10)$$

$$\text{where } I(M_W) = \int_0^\infty dE_{rec} \frac{c_1 N_A M_N \rho_D}{2\sqrt{\pi} \mu_1^2} |F(q)|^2 v_0 \frac{A^2}{E_0} e^{-\frac{c_2 E_{rec}}{E_0 r}}. \quad (8.11)$$

The exclusion limit can now be written as:

$$\sigma_{WN}(M_W) = \frac{\lambda_{CL}}{I(M_W) T_0} = \frac{-\ln(1 - CL)}{I(M_W) T_0}. \quad (8.12)$$

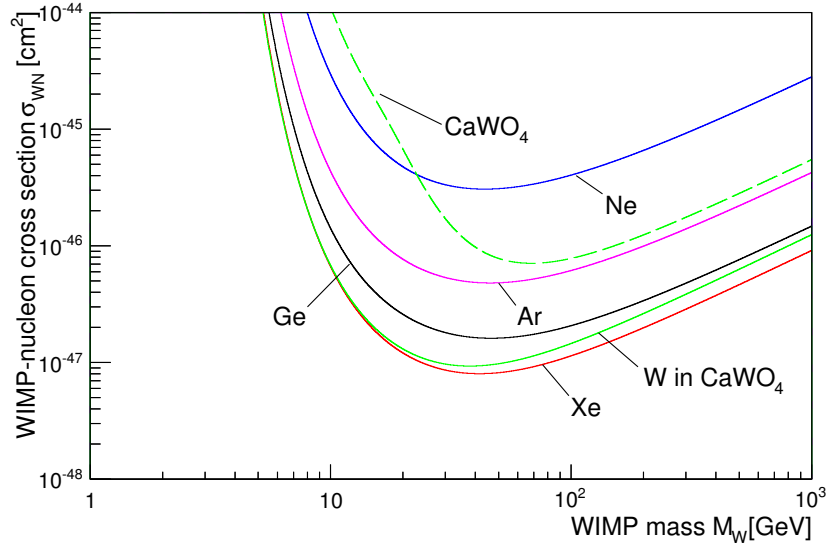


Figure 8.7: Exclusion plots (90 % exclusion limit) for different target materials used for direct dark-matter searches. For these plots an exposure of one ton-year was assumed and the optimal search regions listed in table 8.1 were used. The green dashed line shows the exclusion limit for CaWO_4 if the discrimination (see section 8.2) between the constituents (O, Ca and W) is not possible. If this discrimination is possible, tungsten can be used independently of calcium and oxygen leading to the green solid line.

Figure 8.7 shows the 90 % exclusion limits for different target materials using the optimal search regions and assuming an exposure T_0 of one ton-year. If the discrimination between tungsten and calcium and oxygen recoils (see section 8.2) is not possible, the energy threshold has to be 16.31 keV to avoid background events due to solar neutrinos. Since the WIMP-recoil spectra shown in figure 8.1 are exponential, a higher energy threshold leads to worse sensitivity. The exclusion limit for CaWO_4 without discrimination is represented by the dashed (green) line in figure 8.7.

If, however, the discrimination between the constituents of CaWO_4 is possible, tungsten alone could be used for direct dark-matter search. In that case the energy threshold would be 2.05 keV leading to a much better sensitivity. The exclusion limit for CaWO_4 with a discrimination between the constituents is represented by the solid green line in figure 8.7.

In addition, such a measurement would make it possible to compare the numbers of WIMP scattering events on O, Ca, and W (multi-target experiment) and, thus, directly confirm the WIMP hypothesis used.

Since the energy thresholds of most direct dark-matter searches are well

above the thresholds of the optimal regions given in table 8.1, it is more appropriate to calculate the exclusion limits for the current search regions. In table 8.3 the expected numbers of atmospheric and solar neutrino events

Material	E_{th} [keV]	Solar	Atmosph.	Max. exposure
Ar	30	$2.91 \cdot 10^{-8}$	$7.15 \cdot 10^{-3}$	14.0 ton-years
Ge	10	$2.51 \cdot 10^{-8}$	$1.98 \cdot 10^{-2}$	5.1 ton-years
Xe	8.4	$1.56 \cdot 10^{-10}$	$2.34 \cdot 10^{-2}$	4.3 ton-years
CaWO ₄	12	$5.35 \cdot 10^{-1}$	$8.45 \cdot 10^{-3}$	0.18 ton-years
CaWO ₄ (98 %)	12	$1.07 \cdot 10^{-2}$	$3.98 \cdot 10^{-4}$	9.0 ton-years
W in CaWO ₄	12	$3.76 \cdot 10^{-11}$	$8.06 \cdot 10^{-3}$	12.4 ton-years

Table 8.3: Number of events per ton-year for atmospheric and solar neutrinos for different target materials. The energy thresholds used for the calculation of the count rates are given in column two. In the last column the maximal exposures are listed, i.e., the exposure leading to ~ 0.1 neutrino events. For calcium tungstate (CaWO₄) three scenarios are listed: the first shows the values if no discrimination between the constituents of CaWO₄ is possible. For the second scenario an exclusion of 98% of all oxygen events was applied using the present status of the discrimination mechanism. For the last scenario only tungsten events were taken into account assuming a complete separation of the three constituents of CaWO₄.

for an exposure of one ton-year are listed for the current energy thresholds listed in the second column and also in table 8.1. The maximal exposures listed in the last column of table 8.3 are leading to an expected number of atmospheric and solar neutrino events of ~ 0.1 in the current regions for direct dark-matter searches.

For calcium tungstate there are three different scenarios listed. For the first scenario it was assumed that no discrimination between the three constituents of CaWO₄ is possible. The maximal exposure for this case is very small (~ 0.18 ton-years) due to the large number of solar neutrino events for oxygen.

For the third scenario only tungsten events were taken into account assuming a complete separation of the constituents of CaWO₄ above a recoil energy of 12 keV. Due to the large mass of tungsten only atmospheric neutrinos are contributing to the neutrino background making a large maximal exposure of 12.4 ton-years possible.

For the second scenario a partial separation of the constituents was assumed. The separation of the constituents is based on the different amount of produced scintillation light for the same recoil energy[93]. For a gamma or beta event about 1 to 2%[95] of the energy E_{rec} deposited in the CaWO₄ crystal is measured as scintillation light by a separate light detector[34, 96].

The scintillation light which is produced by nuclear recoils is smaller by the quenching factor Q_i which depends on the constituent. The quenching

Nucleus	Quenching factor [%]
O	$Q_O = 10.4 \pm 0.5$
Ca	$Q_{Ca} = 6.38^{+0.62}_{-0.65}$
W	$Q_W = 3.91^{+0.48}_{-0.43}$

Table 8.4: Quenching factors Q_i for the constituents of calcium tungstate (CaWO_4)[38].

factors Q_i of the different constituents of CaWO_4 are listed in table 8.4[38]. The energy E_{ph} deposited in the light detector is given by

$$\langle E_{ph} \rangle = L_0 Q_i E_{rec}, \quad (8.13)$$

where L_0 is the absolute detected light yield of typically 1% - 2%. For a recoil energy of ~ 10 keV and $L_0 = 2\%$ only ~ 3 photons are absorbed in the light detector for a tungsten recoil.

The absolute light yield L_0 differs between the CaWO_4 crystals used in CRESST[38, 95, 96]. To compare the results of different crystals a normalized light yield $L(E_{rec})$ is introduced:

$$L(E_{rec}) = \frac{1}{L_0} \frac{E_{ph}}{E_{rec}} \quad (8.14)$$

$$\langle L(E_{rec}) \rangle = \frac{1}{L_0} \frac{\langle E_{ph} \rangle}{E_{rec}} = Q_i. \quad (8.15)$$

$L(E_{rec})$ is normalized to 1 for gamma events with an energy of ~ 122 keV[38, 96]. The mean value of L is given by the quenching factors Q_i . For large recoil energies and for electron recoils the number of photons absorbed by the light detector is high enough so that the distribution of the photon number can be approximated by a normal distribution. For nuclear recoils, especially for tungsten recoils, the number of absorbed photons is too small for this approximation. However, due to the small energy deposition in the light detector the distribution of E_{ph} is dominated by the electronic noise of the light detector which is also normal distributed. The width σ_i of the light yield of a nucleus i is given by:

$$\sigma_i = \frac{1}{L_0} \frac{1}{E_{rec}} \sqrt{\sigma_{BL}^2 + E_0 E_{ph}} = \frac{1}{L_0} \frac{1}{E_{rec}} \sqrt{\sigma_{BL}^2 + E_0 L_0 Q_i E_{rec}}, \quad (8.16)$$

where σ_{BL} is the width of the electronic noise (i.e., the width of the base line) and $E_0 = 2.88$ eV is the energy of one photon ($\lambda_{\text{CaWO}_4} = 430$ nm) emitted

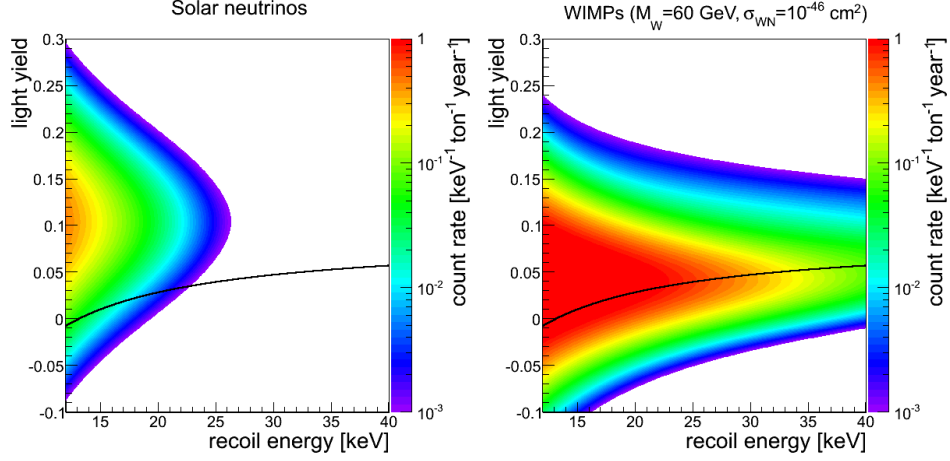


Figure 8.8: Light-yield plots for solar neutrinos and for WIMPs ($M_W = 60 \text{ GeV}$, $\sigma_{WN} = 1.0 \cdot 10^{-46} \text{ cm}^2$). The colors represent the count rates for different recoil energies E_{rec} and different light yields L . For the shown energy region (12 - 40 keV) solar neutrinos are mainly scattering off oxygen while WIMPs are mainly producing tungsten recoils. The black line shows the 98% exclusion limit for oxygen recoils, i.e., 98% of all oxygen recoil events are above this line. This line can be used to reject the majority of the solar neutrino background events.

by a calcium tungstate crystal. The equations (8.14) and (8.16) were used to produce the light-yield plots depicted in figure 8.8. The colors represent the count rates for the different recoil energies E_{rec} and the light yields L . The projections of those distributions on the recoil energy axis are the recoil energy spectra shown in figures 8.2, 8.4, and 8.1.

Since solar neutrino events are mainly oxygen recoils and WIMP events mainly tungsten recoils it is possible to reject the majority of solar neutrino events and to keep a large part of WIMP events. The light yield of oxygen recoils is normal distributed with the quenching factor Q_O as mean and the width σ_O given by equation (8.16). This normal distribution is given by

$$f(L) = \frac{1}{\sqrt{2\pi}\sigma_O} e^{-\frac{(L-Q_O)^2}{2\sigma_O^2}} = \frac{1}{\sigma_O} \phi\left(\frac{L-Q_O}{\sigma_O}\right), \quad (8.17)$$

where ϕ is a normal distribution with mean 0 and width 1. The cumulative distribution of the light-yield is given by

$$F(L) = \frac{1}{\sqrt{2\pi}\sigma_O} \int_{-\infty}^L e^{-\frac{(t-Q_O)^2}{2\sigma_O^2}} dt = \Phi\left(\frac{L-Q_O}{\sigma_O}\right), \quad (8.18)$$

where Φ is the cumulative distribution of ϕ . A fraction p of all events is

above the limit L_{max} , if L_{max} fulfills the equation:

$$\frac{1}{\sqrt{2\pi}\sigma_O} \int_{L_{max}}^{\infty} e^{-\frac{(t-Q_O)^2}{2\sigma_O^2}} dt = 1 - F(L_{max}) = 1 - \Phi\left(\frac{L_{max} - Q_O}{\sigma_O}\right) = p. \quad (8.19)$$

The limit L_{max} can now be calculated:

$$L_{max} = Q_O + \sigma_O \Phi^{-1}(1 - p) \quad (8.20)$$

$$= Q_O + \frac{\Phi^{-1}(1 - p)}{L_0 E_{rec}} \sqrt{\sigma_{BL}^2 + E_0 L_0 Q_O E_{rec}}, \quad (8.21)$$

where Φ^{-1} is the inverse of Φ . The black line in figure 8.8 represents the limit L_{max} for $p = 98\%$, i.e., 98% of all oxygen recoils are above this line. For the calculation of this black line an absolute light yield $L_0 = 2\%$ [95] and an electronic noise $\sigma_{BL} = 10 \text{ eV}$ [96] were assumed.

Apart from the area determined by equation (8.21) it is possible to define a lot of other areas also containing the same fraction p of all solar neutrino events. However, with the upper limit L_{max} given by equation (8.21) the fraction p of all oxygen-recoil events is rejected. Thus, independent of the recoil-energy distribution, the fraction p of all background sources generating oxygen-recoil events is rejected, e.g., also the majority of neutron background events can be rejected.

The limit L_{max} was used to calculate the number of atmospheric and solar neutrinos as well as the maximum exposure for the direct dark-matter search listed in table 8.3. Figure 8.9 shows the 90% exclusion limits of different target materials using the energy thresholds and maximal exposures listed in table 8.3. For the dashed green line all events of all constituents were taken into account representing a scenario without separation of the constituents. Due to the large number of solar-neutrino induced oxygen recoils the sensitivity of this scenario is worse by a factor of ~ 50 compared to germanium or xenon.

The dotted green line represents a scenario where 98% of the oxygen recoils are rejected (black line in figure 8.8). For this scenario the sensitivity is much better than for the scenario without separation. However, the sensitivity is still worse by a factor of ~ 5 than the sensitivity of germanium and xenon.

For the solid green line only tungsten recoils were taken into account leading to a sensitivity comparable to the sensitivity of xenon for WIMP masses $M_W \gtrsim 50 \text{ GeV}$. This scenario represents a complete separation of the contributions of the constituents of CaWO_4 . Therefore, the separation thresholds of CRESST detectors have to be decreased by a factor of ~ 10 ,

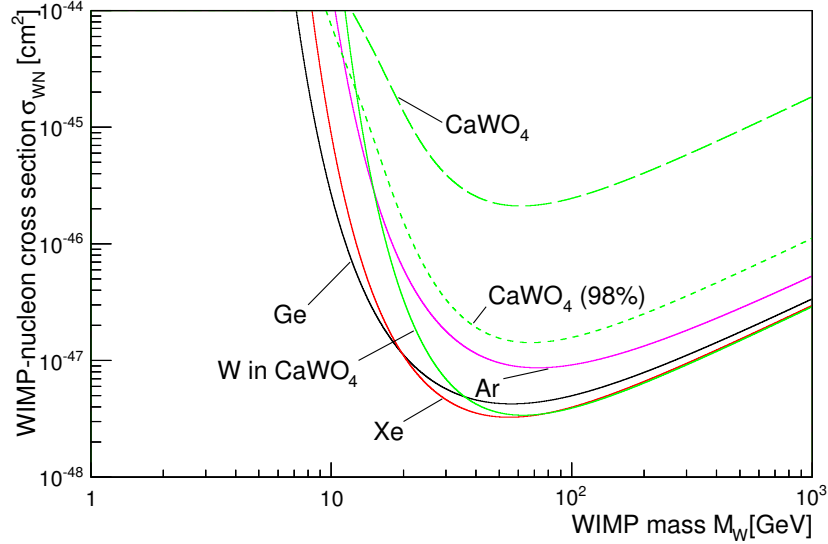


Figure 8.9: Exclusion plots (90 % exclusion limits) for the current search regions and maximal exposures listed in table 8.3. The dashed green line represents the scenario where the events of all constituents of CaWO_4 were taken into account without separation of O, Ca and W events. The dotted line represents a scenario where 98 % of all oxygen recoil events are rejected. For the solid green line only tungsten recoils were taken into account representing a scenario with a complete separation of the events of the constituents. For this scenario the separation thresholds of CRESST detectors have to be improved by a factor of ~ 10 .

which is only possible, if both the electronic noise σ_{BL} and the absolute light yield L_0 are improved.

If atmospheric and solar neutrinos were the only background sources for direct dark-matter searches, germanium and xenon presently would be the best target materials. However, the current dark-matter searches observed 2 - 3 background events for exposures of $\mathcal{O}(100)$ kg-days [29, 36, 97]. So it is likely that for exposures of $\mathcal{O}(1)$ ton-years other background sources like fast neutrons are even more important than atmospheric and solar neutrinos. Since neutrons are interacting mainly with oxygen, the black line in figure 8.8 would also reject a large part of the possible neutron background in a CaWO_4 target. Such a background suppression is not possible for germanium or xenon. Thus, all different background sources have to be taken into account to choose the best target material for direct dark-matter searches.

Chapter 9

Conclusions and outlook

Coherent Neutrino Nucleus Scattering (CNNS) is a neutral current process and hence independent of the neutrino flavor. A neutrino scatters off a target nucleus via the exchange of a virtual Z^0 boson. For low transferred momenta the wavelength of the Z^0 is comparable to the diameter of the target nucleus. Thus, the neutrino scatters coherently off all nucleons leading to an enhanced ($\propto N^2$) cross section. However, up to now CNNS has not been observed experimentally due to the small recoil energies of the target nuclei ($\mathcal{O}(\text{keV})$).

For the first observation of CNNS a strong neutrino source is needed. Thus, the expected count rates for several neutrino sources have been calculated and discussed. The strongest natural neutrino sources are the sun and core-collapse supernovae in our galaxy. However, due to the low energies of the majority of solar neutrinos detectors with an energy threshold $\lesssim 0.1$ keV are needed to observe ~ 0.5 neutrino events per ton-day. Because of the small count rates a ton-scale experiment is needed to observe CNNS. Therefore, the observation of CNNS with solar neutrinos bears a lot of technical difficulties due to the required large target mass and the low energy threshold of the detection system. Supernova neutrinos, on the other hand, have larger energies than solar neutrinos leading to larger recoil energies. Thus, also detectors with large energy thresholds can be used to detect supernova neutrinos. For ton-scale direct dark-matter searches a supernova at a distance of ~ 10 kpc leads to ~ 2 neutrino events in the energy region used for dark matter search. Due to the good background suppression of direct dark-matter searches a few supernova-neutrino events in ~ 10 s could not be explained by background. Thus, the next generation of direct dark-matter searches with ton-scale target masses and energy thresholds of $\lesssim 10$ keV will be able to observe CNNS with the neutrinos generated by a core-collapse supernova at a distance of ~ 10 kpc.

Since ton-scale target masses are needed for an observation of CNNS using

natural neutrino sources, also artificial neutrino sources have been studied. If a beam of protons with energies of 650 to 1500 MeV is guided to a beam dump, amongst others π^+ particles are generated, which are stopped before their decay. During the decay of these π^+ typically three neutrinos with energies of up to ~ 50 MeV are produced. Due to the large neutrino energies such a stopped pion source could be used to observe CNNS, if it is possible to build a proton accelerator with a power of ~ 1 MW in an underground facility. Also power reactors as neutrino sources have been studied. Due to the high neutrino fluxes generated by reactors with thermal powers of 2 to 4 GW an experiment with a target mass of $\mathcal{O}(1 \text{ kg})$ located at a distance of 20 to 40 m (neutrino flux of 10^{12} to $10^{13} \text{ cm}^{-2} \text{ s}^{-1}$) from the reactor core could observe CNNS with expected count rates of $\mathcal{O}(10 \text{ kg}^{-1} \text{ day}^{-1})$. Since a lot of reactors with such powers are already available, reactor neutrinos are at present the most promising source for an observation of CNNS.

For reactor neutrinos and an assumed energy threshold of 0.5 keV, sapphire as target material would generate the largest count rate. Indeed, low-temperature detectors can reach an energy threshold of 0.5 keV with sapphire as target material. Thus, a low-temperature detector based on a 32 g sapphire crystal ($40 \times 20 \times 10 \text{ mm}^3$) was designed and studied in the present thesis. A Transition Edge Sensor (TES) based on an Ir-Au bilayer was directly evaporated onto the sapphire crystal. Both a calibration and a background measurement were performed with this low-temperature detector. The energy threshold for this detector is ~ 1 keV which, however, is too large for an observation of CNNS. This rather high energy threshold can be explained by poor properties of the TES. Since the critical temperature ($T_c \lesssim 7 \text{ mK}$) of the superconducting Ir-Au bilayer is below the base temperature ($T_{base} \approx 10 \text{ mK}$) of the dilution refrigerator used for the measurements, only the flat part of the transition curve between the superconducting and the normal conducting phase could be used for the operation of the detector. Thus, to improve the energy threshold of the detector a TES with a critical temperature of $\sim 20 \text{ mK}$ and a steeper phase transition is needed.

Although the energy threshold of the low-temperature detector used for the present work is too large for an observation of CNNS, the detector could still be applied to measure the background spectrum for energies below $\sim 10 \text{ keV}$. In the energy region up to $\sim 200 \text{ keV}$ the measured background spectrum is featureless and follows an exponential decay. For low energies ($\lesssim 10 \text{ keV}$) the spectrum is almost flat. To study the background composition several simulations using different background sources were performed. The resulting spectra are compared to the measured background spectrum to identify the main contribution to the background. The simulation of ambient neutrons produced by cosmic muons in the walls surrounding the detector

results in a spectrum which is much steeper than the measured one. Thus, ambient neutrons are only a small contribution to the measured spectrum. External gamma rays are identified to be also a minor contribution to the background spectrum, since a large fraction of the gamma rays are absorbed in the walls of the refrigerator, and the resulting spectra should have features like Compton edges or photo-peaks. Also a simulation with cosmic muons was performed. For this simulation the energy and angular distribution of cosmic muons at sea level were used. The resulting spectrum is in good agreement with the measured background spectrum for energies below ~ 10 keV. Also for energies above ~ 10 keV the simulated and the measured spectra are in reasonable agreement. Thus, cosmic muons are the main contribution to the measured background spectrum.

For a future experiment aiming at the observation of CNNS the use of 125 low-temperature detectors based on 32 g sapphire crystals ($20 \times 20 \times 20$ mm³) is assumed. The detectors are arranged in an array of $5 \times 5 \times 5$ detectors. This array is surrounded by a passive shielding of 20 cm of polyethylene, 10 cm of copper and 10 cm of lead. In addition, the complete shielding is surrounded by a muon veto system. Since the probability that a neutrino scatters off in more than one detector is vanishingly small, coincident events in more than one detector can be used to reject background events. Again several simulations using the setup of the detector array and different background sources were performed to estimate the efficiency of this background rejection technique. The simulation of ambient neutrons shows that $\sim 98\%$ of the neutrons are absorbed in the shielding and the efficiency of the background rejection due to coincident events is $\sim 30\%$ for the energy region below ~ 4 keV used for the observation of CNNS. For larger energies the efficiency for the background rejection increases up to $\sim 60\%$. Using the results of the simulation of gamma rays generated by intrinsic radioactivity, upper limits for the allowed radioactivity of the sapphire crystals and the copper holder of the detector array can be obtained. For the sapphire crystals ~ 100 mBq kg⁻¹ and for the copper holder ~ 10 mBq kg⁻¹ are allowed which can easily be achieved. The simulation of cosmic muons shows that the efficiency for the muon background rejection due to coincident events is very small ($\lesssim 1\%$) for energies below ~ 10 keV. For higher energies the efficiency increases to $\sim 20\%$. Thus, a good muon veto system is crucial for the rejection of muon-induced background events. For an efficient background rejection ($\gtrsim 99.9\%$) a good time resolution of the detector is needed to avoid large dead times. For a dead time of $\sim 10\%$ a time resolution of ~ 10 μ s is required. Such a good time resolution sets strong constraints on the properties of a low-temperature detector. To achieve such a good time resolution the effective area of the TES has to be increased, e.g., by the use of superconducting

structures attached to the TES, so-called phonon collectors.

To study the observation potential of the experiment discussed in the present work four ensembles of spectra containing background and signal events were simulated. For one ensemble the spectra were simulated taking only background events but no neutrino events into account. For the other three ensembles different background rates (1000, 1500, and 2000 $\text{kg}^{-1} \text{day}^{-1}$) in the energy region below 4 keV were used. For these three ensembles a neutrino rate of 3.3 $\text{kg}^{-1} \text{day}^{-1}$ corresponding to a distance of ~ 40 m from a reactor with a thermal power of ~ 4 GW (neutrino flux of $3.6 \cdot 10^{12} \text{ cm}^{-2} \text{ s}^{-1}$) was assumed. Furthermore, it was assumed that ~ 20 % of all neutrino events are rejected due to coincidences with the muon veto or other detectors. Each simulated spectrum was fitted by a background-only model and a model containing signal and background using a Bayesian approach. If the probability that the background-only model describes the spectrum is not sufficient an observation of CNNS can be claimed. For the 2000 spectra containing only background events no false claim of an observation occurred. For ~ 84 % of the spectra with a mean background rate of 1000 $\text{kg}^{-1} \text{day}^{-1}$, for ~ 52 % of the spectra with a background rate of 1500 $\text{kg}^{-1} \text{day}^{-1}$, and for ~ 28 % of the spectra with a background rate of 2000 $\text{kg}^{-1} \text{day}^{-1}$ an observation of CNNS could be claimed at a confidence level of 99.99 % for an exposure of 4 kg-years.

For locations closer to the reactor the investigation of new physics beyond the standard model appears to be possible. Thus, two further ensembles were simulated to study the influence of a hypothetical magnetic moment of the neutrino and oscillations of flavor neutrinos into sterile neutrinos. For both ensembles a distance of ~ 20 m from the reactor core leading to a neutrino rate of $\sim 13 \text{ kg}^{-1} \text{day}^{-1}$ and a background rate of 500 $\text{kg}^{-1} \text{day}^{-1}$ was assumed. To estimate the sensitivity to a magnetic moment a model containing background, neutrino signal and a magnetic moment was fitted to the simulated spectra containing no magnetic moment. The resulting upper limits for the magnetic moment of the neutrino are larger by a factor of ~ 3 than the current best limit of $3.2 \cdot 10^{-11} \mu_B$. To study the potential for the observation of sterile neutrinos an oscillation with an amplitude of 2 % between flavor ($\nu_e, \nu_\mu, \nu_\tau, \bar{\nu}_e, \bar{\nu}_\mu, \text{ and } \bar{\nu}_\tau$) and sterile neutrinos was assumed. As a result of the estimation of the neutrino rate, for ~ 1 % of the spectra sterile neutrinos are leading to a 3- σ effect compared to the no-oscillation hypothesis. Thus, the investigation of new physics beyond the standard model is challenging for the setup described in the present thesis.

Atmospheric and solar neutrinos constitute an ultimate background for direct dark-matter searches, since CNNS can generate the same signature as WIMP scatterings. For most target materials the events caused by solar

neutrinos are well below the energy threshold used for direct dark-matter search. The atmospheric neutrino background limits the achievable sensitivity for the WIMP-nucleon cross section to a value between 3 and $9 \cdot 10^{-48} \text{cm}^2$. However, for calcium tungstate also solar neutrinos have to be taken into account, since the recoil energies generated by solar neutrinos scattering off oxygen are above the energy threshold. Solar neutrinos limit the achievable sensitivity for the WIMP-nucleon cross section to $2 \cdot 10^{-46} \text{cm}^2$ if a discrimination between the constituents of calcium tungstate is not possible. However, with a rejection of $\sim 98\%$ of all oxygen recoils, the sensitivity for the WIMP-nucleon cross section can be improved by a factor of ~ 10 . Furthermore, such an improvement is also possible if the sensitivity is limited by neutron background. The current best limit for the WIMP-nucleon cross section is $\sim 2 \cdot 10^{-45} \text{cm}^2$ achieved with xenon as target material. Thus, atmospheric and solar neutrinos have to be taken into account for the next-generation experiments with ton-scale target masses.

References

- [1] A. K. Drukier, et al., *Principles and applications of a neutral-current detector for neutrino physics and astronomy*, Phys. Rev. D **30**, 2295 (1984)
- [2] A. Gütlein, et al., *Solar and Atmospheric Neutrinos: Background Sources for the Direct Dark Matter Searches*, Astropart. Phys. **34**, 90 (2010), [arXiv:1003.5530v3](https://arxiv.org/abs/1003.5530v3)
- [3] B. Povh, et al., *Teilchen und Kerne*, Springer-Verlag, Berlin Heidelberg New York, 5th edition (2001)
- [4] J. D. Lewin, et al., *Review of mathematics, numerical factors, and corrections for dark matter experiments based on elastic nuclear recoil*, Astropart. Phys. **6**, 87 (1996)
- [5] R. H. Helm, *Inelastic and Elastic Scattering of 187-MeV Electrons from Selected Even-Even Nuclei*, Phys. Rev. **104**, 1466 (1956)
- [6] J. Beringer, et al., Particle Data Group, *Review of Particle Physics*, Phys. Rev. D **86**, 010001 (2012)
- [7] W. H. Press, et al., *Numerical Recipes: The Art of Scientific Computing*, Cambridge University Press, 3rd edition (2007)
- [8] J. N. Bahcall, et al., *New Solar Opacities, Abundances, Helioseismology, and Neutrino Fluxes*, ApJ **621**, L85 (2005)
- [9] J. N. Bahcall, <http://www.sns.ias.edu/~jnb/>
- [10] G. Bellini, et al., Borexino collaboration, *First Evidence of pep Solar Neutrinos by Direct Detection in Borexino*, Phys. Rev. Lett. **108**, 051302 (2012)
- [11] A. M. Serenelli, et al., *Solar Models with Accretion. I. Application to the Solar Abundance Problem*, ApJ **743**, 24 (2011)

-
- [12] B. Cabrera, et al., *Bolometric detection of neutrinos*, Phys. Rev. Lett. **55**, 25 (1985)
- [13] A. K. Drukier, et al., *Detecting cold dark-matter candidates*, Phys. Rev. D **33**, 3495 (1986)
- [14] J. Monroe, et al., *Neutrino backgrounds to dark matter searches*, Phys. Rev. D **76**, 033007 (2007)
- [15] L. E. Strigari, *Neutrino coherent scattering rates at direct dark matter detectors*, New J. of Phys. **11**, 105011 (2009)
- [16] J. Vergados, et al., *Can solar neutrinos be a serious background in direct dark matter searches?*, Nucl. Phys. B **804**, 144 (2008)
- [17] V. Kopeikin, et al., *Reactor as a Source of Antineutrinos: Thermal Fission Energy*, arXiv:hep-ph/0410100v1 (2004)
- [18] O. Tengblad, et al., *Integral $\bar{\nu}$ -spectra derived from experimental β -spectra of individual fission products*, Nucl. Phys. A **503**, 136 (1989)
- [19] P. Colling, et al., *Low-energy X-ray detection in cryogenic detectors with tungsten thermometers*, Nucl. Instr. Meth. A **354**, 408 (1995)
- [20] M. Sistia, et al., *Massive cryogenic particle detectors with low energy threshold*, Nucl. Instr. Meth. A **466**, 499 (2001)
- [21] J. Mandula, *Nuclear Power Reactors in the World 2012 Edition, Reference Data Series 2*, International Atomic Energy Agency, Vienna (2012)
- [22] J. Wuttke, et al., *SPHERES, Jülich's high-flux neutron backscattering spectrometer at FRM II*, Rev. Sci. Instrum. **83**, 075109 (2012), arXiv:1204.3415v5
- [23] J. Alonso, et al., *Expression of Interest for a Novel Search for CP Violation in the Neutrino Sector: DAEdALUS*, arXiv:1006.0260v1 (2010)
- [24] K. Scholberg, *Prospects for measuring coherent neutrino-nucleus elastic scattering at a stopped-pion neutrino source*, Phys. Rev. D **73**, 033005 (2006)
- [25] W. Fetscher, *Muon decay: Measurement of the energy spectrum of the ν_e as a novel precision test for the standard model*, Phys. Rev. Lett. **69**, 2758 (1992)

-
- [26] H. Burkard, et al., *Muon decay: Measurement of the transverse positron polarization and general analysis*, Phys. Lett. B **160**, 343 (1985)
- [27] M. Bardon, et al., *Measurement of the Momentum Spectrum of Positrons from Muon Decay*, Phys. Rev. Lett. **14**, 449 (1965)
- [28] L. Michel, *Interaction between Four Half-Spin Particles and the Decay of the μ -Meson*, Proc. Phys. Soc. (London) A **63**, 514 (1950)
- [29] Z. Ahmed, et al., CDMS II collaboration, *Dark Matter Search Results from the CDMS II Experiment*, Science **327**, 1619 (2009), [arXiv:0912.3592v1](#)
- [30] H.-T. Janka, *Explosion Mechanisms of Core-Collapse Supernovae*, [arXiv:1206.2503v1](#) (2012)
- [31] M. Biassoni, et al., *Study of supernova ν -nucleus coherent scattering interactions*, Astropart. Phys. **36**, 151 (2012)
- [32] M. Costantini, et al., *The interest in neutrinos from core collapse supernovae*, Nucl. Phys. B (Proc. Suppl.) **139**, 27 (2005)
- [33] K. Scholberg, *Supernova Neutrino Detection*, Nucl. Phys. B (Proc. Suppl.) **91**, 331 (2001)
- [34] G. Angloher, et al., CRESST collaboration, *Commissioning run of the CRESST-II dark matter search*, Astropart. Phys. **31**, 270 (2009), [arXiv:0809.1829v1](#)
- [35] D. Akerib, et al., SuperCDMS collaboration, *Present Status of the SuperCDMS*, J. Low Temp. Phys. **151**, 818 (2008)
- [36] E. Aprile, et al., XENON100 Collaboration, *Dark Matter Results from 100 Live Days of XENON100 Data*, Phys. Rev. Lett. **107**, 131302 (2011)
- [37] H. Kraus, et al., EURECA collaboration, *EURECA the European future of cryogenic dark matter searches*, J. Phys. Conf. Ser. **39** (2006)
- [38] G. Angloher, et al., CRESST collaboration, *Results from 730 kg days of the CRESST-II Dark Matter Search*, Eur. Phys. J. C **72**, 1 (2012), [arXiv:1109.0702v1](#)
- [39] E. Armengaud, et al., EDELWEISS collaboration, *Final results of the EDELWEISS-II WIMP search using a 4-kg array of cryogenic germanium detectors with interleaved electrodes*, Phys. Lett. B **702**, 329 (2011), [arXiv:1103.4070](#)

-
- [40] E. Aprile, et al., XENON1T collaboration, *The XENON1T Dark Matter Search Experiment*, arXiv:1206.6288v1 (2012)
- [41] C. Regenfus, ArDM collaboration, *The Argon Dark Matter Experiment (ArDM)*, J. Phys. Conf. Ser. **203**, 012024 (2010), arXiv:0912.2962v1
- [42] W. H. Lippincott, et al., *Scintillation yield and time dependence from electronic and nuclear recoils in liquid neon*, arXiv:1111.3260v1 (2011)
- [43] C. E. Aalseth, et al., CoGeNT Collaboration, *Search for an Annual Modulation in a p-Type Point Contact Germanium Dark Matter Detector*, Phys. Rev. Lett. **107**, 141301 (2011)
- [44] M. Agostini, et al., GERDA collaboration, *Characterization of a broad energy germanium detector and application to neutrinoless double beta decay search in ^{76}Ge* , J. Instr. **6**, P04005 (2011)
- [45] F. Pröbst, et al., *Model for cryogenic particle detectors with superconducting phase transition thermometers*, J. Low Temp. Phys. **100**, 69 (1995)
- [46] C. Cozzini, *CRESST Dark Matter Search with Cryogenic Calorimeters*, Ph.D. thesis, Ludwig-Maximilians-Universität München, URL <http://edoc.ub.uni-muenchen.de/1299/> (2003)
- [47] M. Sisti, *CRESST - a Cryogenic Experiment for Direct Dark Matter Search*, Ph.D. thesis, Ludwig-Maximilians-Universität München (1999)
- [48] K. Irwin, *An application of electrothermal feedback for high resolution cryogenic particle detection*, Appl. Phys. Lett. **66**, 1998 (1995)
- [49] H. Kraus, et al., *Quasiparticle trapping in a superconductive detector system exhibiting high energy and position resolution*, Phys. Lett. B **231**, 195 (1989)
- [50] F. Pobell, *Matter and Methods at Low Temperatures*, Springer-Verlag, Berlin, 3rd edition (2007)
- [51] S. Roth, *Sputtered Tungsten Thin Films and Composite Detectors for the Application in the Dark Matter Experiments CRESST and EURECA*, Diploma thesis, Technische Universität München (2007)
- [52] U. Nagel, et al., *Proximity effect in iridium-gold bilayers*, J. Appl. Phys. **76**, 4262 (1994)


- [53] J. Höhne, et al., *Progress on fabrication of iridium-gold proximity-effect thermometers*, Nucl. Inst. Meth. A **370**, 160 (1996)
- [54] J. Clark, et al. (editors), *The SQUID Handbook: Fundamentals and Technology of SQUIDs and SQUID Systems*, Wiley-VCH, 1st edition (2004)
- [55] B. Josephson, *Possible new effects in superconductive tunnelling*, Phys. Lett. **1**, 251 (1962)
- [56] B. D. Josephson, *The discovery of tunnelling supercurrents*, Rev. Mod. Phys. **46**, 251 (1974)
- [57] W. Demtröder, *Experimentalphysik 2, Elektrizität und Optik*, Springer-Verlag, Berlin Heidelberg (2009)
- [58] R. B. Firestone, et al. (editors), *Table of isotopes*, John Wiley & sons, Inc., New York, 8th edition (1996)
- [59] A. Zöller, *Optimierung einer Röntgenfluoreszenzquelle und Untergrunduntersuchungen für ein zukünftiges Experiment zur kohärenten Neutrino-Kern-Streuung*, Diploma thesis, Technische Universität München (2010)
- [60] C. Isaila, et al., *Low-temperature light detectors: Neganov-Luke amplification and calibration*, Phys. Lett. B **716**, 160 (2012)
- [61] A. Langenkämper, *Untersuchung der Realisierbarkeit eines LED Kalibrierungsverfahrens für auf Saphir basierende Tieftemperaturdetektoren*, Bachelor's thesis, Technische Universität München (2012)
- [62] E. Pantić, *Performance of Cryogenic Light Detectors in the CRESST-II Dark Matter Search*, Ph.D. thesis, Technische Universität München, URL <http://mediatum.ub.tum.de/node?id=668368> (2008)
- [63] M. Dobbs, et al., *Frequency multiplexed superconducting quantum interference device readout of large bolometer arrays for cosmic microwave background measurements*, arXiv:1112.4215v2 (2012)
- [64] P. H. Barrett, et al., *Interpretation of Cosmic-Ray Measurements Far Underground*, Rev. Mod. Phys. **24**, 133 (1952)
- [65] M. Ambrosio, et al., *Seasonal variations in the underground muon intensity as seen by MACRO*, Astropart. Phys. **7**, 109 (1997)

-
- [66] C. Isaila, *Development of Cryogenic Light Detectors with Neganov-Luke Amplification for the Dark Matter Experiments CRESST and EURECA*, Ph.D. thesis, Technische Universität München, URL <http://mediatum.ub.tum.de/node?id=980371> (2010)
- [67] R. Lang, *Search for Dark Matter with the CRESST Experiment*, Ph.D. thesis, Technische Universität München, URL <http://mediatum.ub.tum.de/node?id=677820> (2008)
- [68] S. Agostinelli, et al., *Geant4a simulation toolkit*, Nucl. Inst. Meth. A **506**, 250 (2003)
- [69] Y.-F. Wang, et al., *Predicting neutron production from cosmic-ray muons*, Phys. Rev. D **64**, 013012 (2001)
- [70] C. Ciemniak, *Setup of a Neutron Scattering Facility for the Measurement of Scintillation Light Quenching Factors of Low-Temperature Detectors Used in the Direct Dark Matter Search Experiments CRESST and EURECA*, Ph.D. thesis, Technische Universität München, URL <http://mediatum.ub.tum.de/node?id=1078311> (2011)
- [71] D. Abrams, et al., CDMS Collaboration, *Exclusion limits on the WIMP-nucleon cross section from the Cryogenic Dark Matter Search*, Phys. Rev. D **66**, 122003 (2002)
- [72] M. Hofmann, *Liquid Scintillators and Liquefied Rare Gases for Particle Detectors*, Ph.D. thesis, Technische Universität München, URL <http://mediatum.ub.tum.de/node?id=1115726> (2012)
- [73] A. Caldwell, et al., *Signal discovery in sparse spectra: A Bayesian analysis*, Phys. Rev. D **74**, 092003 (2006)
- [74] A. Caldwell, et al., *BAT The Bayesian analysis toolkit*, Comp. Phys. Comm. **180**, 2197 (2009), [arXiv:0808.2552](https://arxiv.org/abs/0808.2552)
- [75] N. Metropolis, et al., *Equation of State Calculations by Fast Computing Machines*, J. Chem. Phys. **21**, 1087 (1953)
- [76] P. Vogel, et al., *Neutrino electromagnetic form factors*, Phys. Rev. D **39**, 3378 (1989)
- [77] R. Harnik, et al., *Exploring signals in dark matter detectors*, JCAP **07**, 026 (2012)

-
- [78] A. Beda, et al., *Gemma experiment: Three years of the search for the neutrino magnetic moment*, Phys. Part. Nucl. Lett. **7**, 406 (2010)
- [79] Y. Abe, et al., Double Chooz Collaboration, *Indication of Reactor $\bar{\nu}_e$ Disappearance in the Double Chooz Experiment*, Phys. Rev. Lett. **108**, 131801 (2012)
- [80] G. Mention, et al., *Reactor antineutrino anomaly*, Phys. Rev. D **83**, 073006 (2011)
- [81] G. Bertone, et al., *Particle dark matter: evidence, candidates and constraints*, Phys. Rept. **405**, 279 (2005)
- [82] G. Jungman, et al., *Supersymmetric dark matter*, Phys. Rept. **267**, 195 (1996)
- [83] D. Clowe, et al., *A Direct Empirical Proof of the Existence of Dark Matter*, Astroph. J. Lett. **648**, L109 (2006)
- [84] G. Hinshaw, et al., *Nine-Year Wilkinson Microwave Anisotropy Probe (WMAP) Observations: Cosmological Parameter Results*, arXiv:1212.5226v1(2012)
- [85] D. N. Spergel, et al., *Three-Year Wilkinson Microwave Anisotropy Probe (WMAP) Observations: Implications for Cosmology*, Astroph. J. Suppl. S. **170**, 377 (2007)
- [86] J. Bovy, et al., *On the local dark matter density*, arXiv:1205.4033v1 (2012)
- [87] A. Gütlein, et al., *Solar and Atmospheric Neutrinos: Limitations for Direct Dark Matter Searches*, Nucl. Phys. B, Proc. Suppl. **229–232**, 536 (2012), arXiv:1009.3815v2
- [88] R. Bernabei, et al., DAMA/LIBRA collaboration, *New results from DAMA/LIBRA*, arXiv:1002.1028v1 (2010)
- [89] M. Harrison, et al., *Use of activated charcoal for the purification of neon in the CLEAN experiment*, Nucl. Instr. Meth. A **570**, 556 (2007)
- [90] D. N. McKinsey, MiniCLEAN collaboration, *The Mini-CLEAN experiment*, Nucl. Phys. B, Proc. Suppl. **173**, 152 (2007)

-
- [91] Z. Ahmed, et al., CDMS collaboration, *Search for Weakly Interacting Massive Particles with the First Five-Tower Data from the Cryogenic Dark Matter Search at the Soudan Underground Laboratory*, Phys. Rev. Lett **102**, 011301 (2009)
- [92] K. Freese, et al., *Signal modulation in cold-dark-matter detection*, Phys. Rev. D **37**, 3388 (1988)
- [93] J.-C. Lanfranchi, et al., CRESST collaboration, *Neutron scattering facility for characterization of CRESST and EURECA detectors at mK temperatures*, Opt. Mat. **31**, 1405 (2009), [arXiv:0810.0132v1](https://arxiv.org/abs/0810.0132v1)
- [94] G. Battistoni, et al., *The atmospheric neutrino flux below 100 MeV: The FLUKA results*, Astropart. Phys. **23**, 526 (2005)
- [95] M. Kiefer, *Improving the Light Channel of the CRESST-II-Dark Matter Detectors*, Ph.D. thesis, Technische Universität München, Max-Planck-Institut für Physik, URL <http://mediatum.ub.tum.de/node?id=1097360> (2012)
- [96] J. Schmalzer, *The CRESST Dark Matter Search - New Analysis Methods and Recent Results*, Ph.D. thesis, Technische Universität München, Max-Planck-Institut für Physik (2012)
- [97] E. Aprile, et al., XENON100 Collaboration, *Dark Matter Results from 225 Live Days of XENON100 Data*, [arXiv:1207.5988v1](https://arxiv.org/abs/1207.5988v1) (2012)

Danksagung

 m folgendem Abschnitt möchte ich mich bei all denjenigen bedanken, die mich bei der Fertigstellung dieser Doktorarbeit unterstützt haben. Als erstes möchte ich mich bei Prof. Franz von Feilitzsch und seinem Nachfolger Prof. Stefan Schönert für die nette und freundliche Aufnahme am Lehrstuhl E15 und die interessanten Diskussionen bedanken.

Bei meinem Doktorvater Prof. Lothar Oberauer möchte ich mich für die interessante Themenstellung und die vielen hilfreichen Diskussionen und Anregungen bedanken.

Auch beim Leiter der Kryogruppe Dr. Jean-Côme Lanfranchi möchte ich mich für die interessanten Diskussionen und den vielen hilfreichen Tips für den Umgang mit Kryostaten, Aufdampfanlagen und Tieftemperaturdetektoren bedanken.

Bei Dr. Walter Potzel, Dr. Jean-Côme Lanfranchi und Dr. Martin Hofmann möchte ich mich fürs Korrekturlesen bedanken. Durch ihre kritischen Fragen und Kommentare war es möglich viele Unklarheiten in der Arbeit zu entdecken und zu beseitigen.

Ich möchte mich auch bei Sabine Roth bedanken für die großartige Unterstützung beim Herstellen und Betreiben von Tieftemperaturdetektoren, insbesondere für die Hilfe beim Bonden. Auch für die zahlreichen wichtigen Diskussionen möchte ich mich bei ihr bedanken. Auch bei den anderen aktuellen und ehemaligen Mitgliedern der Kryogruppe (Dr. Chritian Ciemiak, Dr. Christian Isaila, Andrea Münster, Dr. Sebastian Pfister, Moritz von Sivers, Raimund Strauß, Stephan Wawoczny, Wolfgang Westphal, Michael Willers und Mark Wüstrich) möchte ich mich für ihre größeren und kleineren Beiträge zur Entstehung dieser Arbeit bedanken.

Bei Dominikus Hellgartner, Quirin Meindl, Randolph Möllenberg und Andreas Zöller möchte ich mich für die vielen zielführenden Diskussionen über Statistik, Datenanalyse und Probleme beim Programmieren bedanken.

Bei Hermann Hagn möchte ich mich ganz besonders bedanken für die großartige Unterstützung bei der elektrischen Entstörung des Kryostaten und

der Messelektronik. Ohne sein Wissen und seine Anregungen wären die Messungen, die in dieser Arbeit präsentiert werden, in dieser Form nicht möglich gewesen.

Bedanken möchte ich mich auch bei Norbert Gärtner für die Unterstützung und die Hilfe bei den Reperaturen an diversen Vakuumpumpen, Aufdampfanlagen und dem Kryostaten. Ebenfalls möchte ich mich bei der Werkstatt (Harald Hess, Erich Seitz und Thomas Richter) für die zahlreichen Tipps und das Herstellen von Detektorhaltern und Teilen für den Kryostaten bedanken. Ohne ihr Wissen und ihren Einsatz wären die Messungen für diese Arbeit nicht möglich gewesen.

Ein ganz besonderes Lob geht auch an meine Mitspieler in der E15 Fußballmannschaft “Die WIMPs” (Nils Haag, Dominikus Hellgartner, Martin Hofmann, Jörn Lepelmeier, Randolph Möllenberg, Uli Thalhammer, Jürgen Winter und Vincenz Zimmer) die mit großem Einsatz und unter Einsatz ihrer Gesundheit mitgeholfen haben beim Fußballturnier des Physik-Departments 2011 einen 1:0 Sieg zu erringen.

Bei Maria Bremberger möchte ich mich für die tolle Unterstützung und Hilfe bei organisatorischen und bürokratischen Problemen bedanken. Außerdem möchte ich ihr auch für die vielen netten Gespräche danken.

Bei allen Mitgliedern des Lehrstuhls E15, auch bei denen die bisher noch nicht genannt wurden (Matteo Agostini, Tobias Bode, Dr. Dusan Budjas, Michael Franke, Dr. Marianne Göger-Neff, Dr. Jozsef Janicsko, Dr. Gunther Korschinek, Andrea Lazzaro, Timo Lewke, Thurid Mannel, Alexander Neumeier, Dr. Patrick Pfahler, Ludwig Prade, Marc Tippmann, Dr. Honghanh Trinhthi), möchte ich mich für die großartige Arbeitsatmosphäre bedanken. Die vielen lustigen und interessanten Gespräche beim Mittagessen und den Kaffeepausen haben zu einem sehr gutem Arbeitsklima beigetragen.

Zuletzt danke ich auch noch meinen Freunden und meiner Familie für ihre Geduld und ihrer aufbauenden Worte beim Schreiben dieser Arbeit.